



Virginia Commonwealth University  
VCU Scholars Compass

---

Theses and Dissertations

Graduate School


---

2018

## Metal-Organic Frameworks and Graphene-Based Support Materials for Heterogeneous Catalysis

Andrew Lin  
*Virginia Commonwealth University*

Follow this and additional works at: <https://scholarscompass.vcu.edu/etd>

 Part of the [Materials Chemistry Commons](#), and the [Physical Chemistry Commons](#)

© The Author

---

Downloaded from

<https://scholarscompass.vcu.edu/etd/5574>

This Dissertation is brought to you for free and open access by the Graduate School at VCU Scholars Compass. It has been accepted for inclusion in Theses and Dissertations by an authorized administrator of VCU Scholars Compass. For more information, please contact [libcompass@vcu.edu](mailto:libcompass@vcu.edu).

METAL-ORGANIC FRAMEWORKS AND GRAPHENE-BASED SUPPORT MATERIALS  
FOR HETEROGENEOUS CATALYSIS

A Dissertation submitted in partial fulfillment of the requirements for the degree of  
Doctor of Philosophy at Virginia Commonwealth University

By

ANDREW LIN  
B.Sc., Virginia Commonwealth University, Virginia, 2013

Director: M. SAMY EL-SHALL  
PROFESSOR, CHAIRMAN DEPARTMENT OF CHEMISTRY

Virginia Commonwealth University  
Richmond, VA  
July 26th, 2018

## Acknowledgments

There are many people that I would like to thank for supporting me during the fulfillment of this arduous task. This dissertation is dedicated in parts to my caring parents Lian Chi Lin and Ya Min Hsu, who encouraged me from a young age to pursue my interests, as well as my legal guardians Xiaochang Yu and Shui Lingmin, whose kindness and hospitality has molded me into the person I am. The warm care and financial support of my family has allowed me to work wholeheartedly on the pursuit of higher education.

This dissertation would not have been possible without the assistance of my research supervisor, Dr. El-Shall, who provided the opportunity to work on the frontiers of exciting scientific discovery in the field of catalysis through access to instrumentation and equipment. His ideas, encouragement, and sense of humor has been much appreciated.

In addition, I would like to thank my postdoc and fellow graduate coworkers, with whom I learned together and stuck with over the course of five years, and whom I would treat as family. I have learned much and have been inspired by the many outstanding lab mates who have preceded and will succeed me; without such positive support, the works presented in this dissertation would have been more lackluster.

I would like to thank the VCU department of chemistry, as well as Dr. Michael Hunnicutt and Dr. Joseph Turner, for the opportunity to teach, mentor, and learn from the many undergraduate students who have enrolled in CHEZ 409. Four years as a teaching assistant in Instrumental Analysis Lab have sharpened my understanding of analytical chemistry and attention to detail.

## Table of Contents

|   | Page      |
|---|-----------|
| Acknowledgments .....   | ii        |
| List of Figures.....  | vi        |
| List of Tables .....  | ix        |
| Abstract.....   | 10        |
| <b>Chapter 1: Introduction .....</b>  | <b>1</b>  |
| <b>1.1 Catalysis .....</b>  | <b>1</b>  |
| <b>1.2 Nanoparticles.....</b>   | <b>2</b>  |
| <b>1.3 Supports.....</b>  | <b>2</b>  |
| <b>1.4 Objectives and Overview.....</b>   | <b>4</b>  |
| <b>Chapter 2: Experimental Methods.....</b>   | <b>7</b>  |
| <b>2.1 Synthesis of MOF and GO Supports.....</b>  | <b>7</b>  |
| 2.1.1 GO Oxide Synthesis .....  | 7         |
| 2.1.2 Pd/Ce-MOF Synthesis.....  | 7         |
| 2.1.3 Pd/Ce-MOF-rGO Synthesis .....   | 8         |
| 2.1.4 Pd/HPW/UiO-66-NH <sub>2</sub> Synthesis .....   | 9         |
| 2.1.5 Pd/GO-PPD/BZD Synthesis .....   | 10        |
| <b>2.2 Catalytic Reactions .....</b>  | <b>10</b> |
| 2.2.1 CO Oxidation .....  | 10        |
| 2.2.2 Vanillin Hydrogenation .....  | 11        |
| 2.2.3 Suzuki Cross Coupling .....   | 11        |
| <b>2.3 Instrumentation.....</b>   | <b>11</b> |
| <b>2.4 Techniques.....</b>  | <b>12</b> |
| 2.4.1 n-Butylamine Titration.....   | 12        |
| 2.4.2 Pyridine Adsorption.....  | 13        |
| <b>Chapter 3: Palladium Nanoparticles Supported on Ce-Metal–Organic Framework for Efficient CO Oxidation and Low-Temperature CO<sub>2</sub> Capture .....</b> | <b>16</b> |
| <b>3.1 Introduction.....</b>  | <b>16</b> |
| <b>3.2 Characterization .....</b>   | <b>19</b> |
| <b>3.3 Effect of Pd wt% on Catalytic CO Oxidation .....</b>   | <b>24</b> |
| <b>3.4 Synergistic Effect between Unsaturated Cerium Nodes and Palladium.....</b>   | <b>27</b> |

|  |     |
|--|-----|
| <b>Chapter 4: Palladium Nanoparticles Supported on a Metal-Organic Framework-Partially Reduced Graphene Oxide Hybrid for the Catalytic Hydrodeoxygenation of Vanillin as a Model for Biofuel Upgrade Reactions</b> ..... | 47  |
| <b>4.1 Introduction</b> .....  | 47  |
| <b>4.2 Characterization</b> .....  | 52  |
| <b>4.3 Acidity Measurement and Active Site Determination</b> .....   | 58  |
| <b>4.4 Effect of Ce-MOF-PRGO Hybridization on Vanillin Hydrogenation Selectivity</b> .....   | 60  |
| <b>4.5 Effect of RGO% in Ce-MOF-PRGO Supports for Vanillin Hydrogenation</b> .....   | 63  |
| <b>4.6 Effect of Palladium Content, Temperature, and Pressure on the Conversion and Selectivity of Ce-MOF-PRGO Supports</b> .....  | 63  |
| <b>4.7 Recyclability of 5% Pd/Ce-MOF Catalysts</b> .....   | 64  |
| <b>4.8 Proposed Mechanism and Literature Comparison</b> .....  | 65  |
| <b>Chapter 5: Acid Site Correlation to Selectivity of 2-Methoxy-4-Methylphenol in Hydrogenation of Vanillin</b> .....  | 92  |
| <b>5.1 Introduction</b> .....  | 92  |
| <b>5.2 Characterization</b> .....  | 94  |
| <b>5.3 Acidity Measurement by Pyridine Adsorption and n-Butylamine Titration</b> .....   | 95  |
| <b>5.4 Pore Volume and Kinetic Diameter for Uptake of HPW into UiO-66-NH<sub>2</sub> and Mass Transfer Limitations of Vanillin into the Pores of UiO-66-NH<sub>2</sub></b> .....   | 97  |
| <b>5.5 Effect of 0-20 wt% HPW/UiO-66-NH<sub>2</sub> for Hydrogenation of Vanillin</b> .....  | 99  |
| <b>5.6 Altered Vanillin Hydrogenation Mechanism in the Presence of a Strongly Acidic Catalyst and the Effect of HPW on Selectivity</b> .....   | 101 |
| <b>5.7 Recycling of 5% HPW/UiO-66-NH<sub>2</sub> and ICP Analysis for Leaching</b> .....   | 105 |
| <b>Chapter 6: Partial Functionalization of Graphene Oxide with p-Phenylenediamine and Benzidine as Novel Supports for Palladium Nanoparticle Catalysts for Room Temperature Suzuki Cross Coupling Reactions</b> .....    | 128 |
| <b>6.1 Introduction</b> .....  | 128 |
| <b>6.2 Strong Electrostatic Adsorption (SEA)</b> .....   | 130 |
| <b>6.3 Characterization</b> .....  | 130 |
| <b>6.4 Effect of PPD/BZD Concentration of GO Interlayer Distance</b> .....   | 134 |
| <b>6.5 Effect of PPD/BZD Concentration on Palladium Uptake and Nanoparticle Size</b> .....   | 136 |
| <b>6.6 Effect of PPD/BZD Functionalization of Suzuki Cross Coupling Activity</b> .....   | 137 |
| <b>6.7 Effect of PPD/BZD Concentration on Suzuki Cross Coupling Activity</b> .....   | 138 |
| <b>6.8 Recycling of 3% Pd/GO-BZD ( 0.1 ) and ICP Analysis for Leaching</b> .....   | 140 |
| <b>Chapter 7: Results and Conclusions</b> .....  | 156 |

**Appendix A** ..... 159  
**List of References** ..... 163

## List of Figures

|   | Page |
|---|------|
| <b>Figure 1.</b> CO oxidation reactor configuration. ....   | 14   |
| <b>Figure 2.</b> Vanillin hydrogenation reactor. ....   | 15   |
| <b>Figure 3.</b> CO oxidation of CO into CO <sub>2</sub> mechanism and illustration of oxygen vacancy in CeO <sub>2</sub> . ....  | 29   |
| <b>Figure 4.</b> Structure and secondary building unit (SBU) of {[Ce(BTC)(H <sub>2</sub> O)]DMF} <sub>n</sub> . ....  | 30   |
| <b>Figure 5.</b> XRD diffractogram for Ce-MOF and 5% Pd/Ce-MOF. ....  | 31   |
| <b>Figure 6.</b> FTIR spectra of Ce-MOF. ....   | 32   |
| <b>Figure 7.</b> Raman spectrum of Ce-MOF. ....   | 33   |
| <b>Figure 8.</b> TEM images of Ce-MOF (a,b) and the 5% Pd/Ce-MOF catalyst (c,d). ....   | 34   |
| <b>Figure 9.</b> Palladium size distribution of palladium nanoparticles supported on Ce-MOF. ....   | 35   |
| <b>Figure 10.</b> XPS C 1s spectra of Ce-MOF (A) and 5% Pd/Ce-MOF (B). ....   | 36   |
| <b>Figure 11.</b> XPS Ce 3d spectra of Ce-MOF (a) and 5% Pd/Ce-MOF (b). ....  | 37   |
| <b>Figure 12.</b> XPS Pd 3d spectra of 5% Pd/Ce-MOF. ....   | 38   |
| <b>Figure 13.</b> TGA plots of Ce-MOF and 5% Pd/Ce-MOF. ....  | 39   |
| <b>Figure 14.</b> N <sub>2</sub> gas adsorption and desorption isotherms of Ce-MOF and 5% Pd/Ce-MOF. ....   | 40   |
| <b>Figure 15.</b> CO <sub>2</sub> uptake of Ce-MOF and 5% Pd/Ce-MOF at 273K. ....   | 41   |
| <b>Figure 16.</b> CO Oxidation activity of 3-7 wt% Pd/Ce-MOF as a function of temperature ramping for a gas mixture of 4% CO and 20% O <sub>2</sub> in helium balance (25 mg catalyst, flow rate of 100cc/min). ....              | 42   |
| <b>Figure 17.</b> CO conversion for 5% Pd/Ce-MOF maintained at 90 °C as a function of time. ....  | 43   |
| <b>Figure 18.</b> CO Oxidation activity of 5 wt% Pd, Pt, and Au on Ce-MOF as a function of temperature ramping for a gas mixture of 4% CO and 20% O <sub>2</sub> in helium balance (25 mg catalyst, flow rate of 100cc/min). .... | 44   |
| <b>Figure 19.</b> Design strategy of a Ce-MOF-PRGO hybrid. ....   | 67   |
| <b>Figure 20.</b> XRD Diffraction patterns of Ce-MOF, Ce-MOF-RGO, and 5% Pd/Ce-MOF-RGO. ....  | 68   |
| <b>Figure 21.</b> FTIR spectra of GO, Ce-MOF-PRGO, and Ce-MOF. ....   | 69   |
| <b>Figure 22.</b> Raman spectra of GO (A), RGO (B), Ce-MOF-PRGO (C), and Ce-MOF (D). ....   | 70   |
| <b>Figure 23.</b> N <sub>2</sub> gas adsorption and desorption isotherms of 5% Pd/Ce-MOF and 5% Pd/Ce-MOF-PRGO. ....  | 71   |
| <b>Figure 24.</b> XPS C 1s spectra of Ce-MOF (A) and 5% Pd/Ce-MOF (B), and 5% Pd/Ce-MOF-PRGO (C). ....  | 72   |
| <b>Figure 25.</b> XPS Ce 3d spectra of Ce-MOF (A) and 5% Pd/Ce-MOF (B), and 5% Pd/Ce-MOF-PRGO (C). ....   | 73   |
| <b>Figure 26.</b> XPS Pd 3d spectra of 5% Pd/Ce-MOF (A), and 5% Pd/Ce-MOF-PRGO (B). ....  | 74   |
| <b>Figure 27.</b> TEM of Ce-MOF (A), 5% Pd/Ce-MOF (B), and Ce-MOF-PRGO (C, D). ....   | 75   |
| <b>Figure 28.</b> TEM of 5% Pd/PRGO (A), and 5% Pd/Ce-MOF-PRGO (B-F). ....  | 76   |
| <b>Figure 29.</b> SEM of 5% Pd/Ce-MOF (A,B) and 5% Pd/Ce-MOF-PRGO. ....   | 77   |
| <b>Figure 30.</b> Palladium nanoparticle size distribution of 5% Pd supported on Ce-MOF (A), Ce-MOF-PRGO (B), and RGO (C). ....   | 78   |
| <b>Figure 31.</b> Potentiometric titration curves of 5% Pd supported on Ce-MOF, Ce-MOF-PRGO, and RGO. ....  | 79   |

|  |     |
|--|-----|
| <b>Figure 32.</b> FTIR spectra of GO + pyridine (A), GO (B), Ce-MOF-PRGO + pyridine (C), Ce-MOF-PRGO (D), Ce-MOF + pyridine (E), and Ce-MOF (F). Peaks for Lewis or Brønsted acid sites are labelled as L and B, respectively. ....  | 80  |
| <b>Figure 33.</b> Hydrogenation of vanillin to 2-methoxy-4-methylphenol.....   | 81  |
| <b>Figure 34.</b> Mol% composition of vanillin, vanillyl alcohol, and 2-methoxy-4-methylphenol as a function of time for 5% Pd on Ce-MOF (A), RGO (B), a physical mixture of Ce-MOF and RGO (C), and Ce-MOF-PRGO hybrid. Reaction conditions: 0.3g vanillin, 40 mL water, 50 mg catalyst, T = 373K, H <sub>2</sub> Pressure = 1 MPA, and stir speed = 900 rpm..... | 82  |
| <b>Figure 35.</b> Mol% of vanillin, vanillyl alcohol, and 2-methoxy-4-methylphenol as a function of PRGO wt% in the Ce-MOF-PRGO support with 5 wt% Pd. Reaction conditions: 0.3g vanillin, 40 mL water, 50 mg catalyst, T = 373K, H <sub>2</sub> Pressure = 1 MPA, and stir speed = 900 rpm, t = 120 min. ....   | 83  |
| <b>Figure 36.</b> Mol% of vanillin, vanillyl alcohol, and 2-methoxy-4-methylphenol as a function of 1-10 wt% Pd in the Ce-MOF-PRGO support for the hydrogenation of vanillin. Reaction conditions: 0.3g vanillin, 40 mL water, 50 mg catalyst, T = 373K, H <sub>2</sub> Pressure = 1 mPA, and stir speed = 900 rpm, t = 120 min. ..                                | 84  |
| <b>Figure 37.</b> Mol% of vanillin, vanillyl alcohol, and 2-methoxy-4-methylphenol as a function of temperature for the 5% Pd/Ce-MOF-PRGO catalyst for the hydrogenation of vanillin. Reaction conditions: 0.3g vanillin, 40 mL water, 50 mg catalyst, H <sub>2</sub> Pressure = 1 mPA, and stir speed = 900 rpm, t = 120 min. ....                                | 85  |
| <b>Figure 38.</b> Mol% of vanillin, vanillyl alcohol, and 2-methoxy-4-methylphenol as a function of pressure for the 5% Pd/Ce-MOF-PRGO catalyst for the hydrogenation of vanillin. Reaction conditions: 0.3g vanillin, 40 mL water, 50 mg catalyst, Temperature = 373K, and stir speed = 900 rpm, t = 120 min. ....  | 86  |
| <b>Figure 39.</b> Reusability of 5% Pd/Ce-MOF-PRGO catalyst for the conversion and selectivity of vanillin into products. Reaction conditions: 0.3g vanillin, 40 mL water, 50 mg catalyst, T = 373K, H <sub>2</sub> Pressure = 1 mPA, and stir speed = 900 rpm, t = 120 min. ....  | 87  |
| <b>Figure 40.</b> XRD of 5% Pd/Ce-MOF-PRGO before and after the vanillin hydrogenation reactions after recycling.....  | 88  |
| <b>Figure 41.</b> Crystal structure of UiO-66 (zirconium oxide secondary building units, or nodes, with 8-coordinated zirconium and 1.15 nm pore size). ....   | 107 |
| <b>Figure 42.</b> Pd nanoparticles on HPW/UiO-66-NH <sub>2</sub> design strategy. ....   | 108 |
| <b>Figure 43.</b> XRD diffractogram of UiO-66-NH <sub>2</sub> as a function of HPW content. All samples contain palladium nanoparticles. ....  | 109 |
| <b>Figure 44.</b> FTIR spectra of 0-20 wt% HPW/UiO-66-NH <sub>2</sub> 0.4% Pd.....   | 110 |
| <b>Figure 45.</b> SEM (A) and TEM (B) of 5% HPW/UiO-66-NH <sub>2</sub> 0.4% Pd. Palladium nanoparticles are circled in red. ....   | 111 |
| <b>Figure 46.</b> TEM of UiO-66-NH <sub>2</sub> (A) and 5% HPW UiO-66-NH <sub>2</sub> . ....   | 112 |
| <b>Figure 47.</b> Pd 3d XPS spectra for palladium nanoparticles supported on UiO-66-NH <sub>2</sub> and 5% HPW UiO-66-NH <sub>2</sub> . ....   | 113 |
| <b>Figure 48.</b> BET adsorption and desorption profiles of the 0-20 wt% HPW/UiO-66-NH <sub>2</sub> supports without palladium nanoparticles. ....   | 114 |
| <b>Figure 49.</b> FT-IR spectra of pyridine adsorption into UiO-66-NH <sub>2</sub> with and without HPW loading. ....  | 115 |
| <b>Figure 50.</b> Potentiometric n-butylamine titration of 0-20 wt% HPW/UiO-66-NH <sub>2</sub> supports.....   | 116 |
| <b>Figure 51.</b> Pore size distribution of UiO-66-NH <sub>2</sub> . ....  | 117 |
| <b>Figure 52.</b> Two-step hydrogenation of vanillin into 2-methoxy-4-methylphenol. Reaction conditions: 300 mg vanillin (2 mmol) in 20 mL of DI water with 50 mg of catalyst (1:200 palladium catalyst:substrate ratio). 1 mPa H <sub>2</sub> gas, 100 °C, 960 rpm.....   | 118 |



|  |     |
|--|-----|
| <b>Figure 53.</b> Vanillin hydrogenation activity as a function of time for palladium catalyst supported on UiO-66-NH <sub>2</sub> (A), 1% HPW/UiO-66-NH <sub>2</sub> (B), 3% HPW/UiO-66-NH <sub>2</sub> (C), 5% HPW/UiO-66-NH <sub>2</sub> (D), 20% HPW/UiO-66-NH <sub>2</sub> (E), and 2-methoxy-4-methylphenol mol% as a function of 0-20 wt% HPW by 60 min. .... | 119 |
| <b>Figure 54.</b> Mol% of 2-Methoxy-4-methylphenol as a function of time with 0-20% HPW loading (A) and 2-Methoxy-4-Methylphenol selectivity as a function of acidity (B) at the 60 minute interval for UiO-66-NH <sub>2</sub> 0.4% Pd with 0-20% HPW loading. ....  | 120 |
| <b>Figure 55.</b> Proposed dehydration-hydrogenation mechanism of vanillyl alcohol into 2-methoxy-4-methylphenol.....  | 121 |
| <b>Figure 56.</b> 5% HPW/UiO-66-NH <sub>2</sub> 0.4% Pd selectivity over 4 repeated runs (A) and XRD diffractogram of HPW/UiO-66-NH <sub>2</sub> 0.4% Pd catalysts before and after recycling. ....  | 122 |
| <b>Figure 57.</b> Structure of PPD (A) and BZD (B). ....   | 142 |
| <b>Figure 58.</b> XRD of GO functionalized with PPD (A) and BZD (B) as an effect of concentration. ....  | 143 |
| <b>Figure 59.</b> FTIR spectra for GO, GO-BZD, and GO-PPD.....   | 144 |
| <b>Figure 60.</b> FTIR spectra as a function of PPD concentration (A), and as a function of BZD concentration (B). ....  | 145 |
| <b>Figure 61.</b> XPS Survey (A), and XPS spectra of C 1s (B), and XPS spectra of Pd 3d (C) for GO, GO-PPD ( 0.1 ), and GO-BZD ( 0.1 ). ....   | 146 |
| <b>Figure 62.</b> Pd 3d XPS for 3% Pd on GO-BZD before and after recycling .....   | 147 |
| <b>Figure 63.</b> TEM images of palladium nanoparticles supported on GO, GO-PPD, and GO-BZD with varying amounts of linkers.....   | 148 |
| <b>Figure 64.</b> Illustration of GO (A) reduced/functionalized with a high concentration of PPD (B) and low concentration of PPD (C). ....  | 149 |
| <b>Figure 65.</b> Suzuki cross coupling conversion% of 3%Pd on GO, GO-PPD ( 0.1 ), and GO-BZD ( 0.1 ). Conditions: 0.3 mol% Pd, 0.32 mmol bromobenzene, 0.38 mmol phenylboronic acid, 1 mmol K <sub>2</sub> CO <sub>3</sub> , and stir speed 450 rpm at r.t.....   | 150 |
| <b>Figure 66.</b> Conversion of reactants into biphenyl product for GO-BZD as a function of BZD concentration (A) and GO-PPD as a function of PPD concentration (B). ....  | 151 |
| <b>Figure 67.</b> Conversion of reactants into biphenyl as a function of the effect of Pd% on GO-BZD ( 0.1 ) samples.....  | 152 |

## List of Tables

|   | Page |
|---|------|
| <b>Table 1.</b> BET surface area measured at 77K and CO <sub>2</sub> uptake at 273K. ....   | 45   |
| <b>Table 2.</b> Comparison of CO oxidation of supported nanoparticles on a series of MOFs. T <sub>50%</sub> and T <sub>100%</sub> are the temperatures for 50% and 100% conversion of CO gas into CO <sub>2</sub> gas. ....               | 46   |
| <b>Table 3.</b> Acidity values of 5 wt% Pd on Ce-MOF, Ce-MOF-PRGO, and RGO. TOF values calculated from number of active sites for mol% composition of 2-methoxy-4-methylphenol at 30 min. ....  | 89   |
| <b>Table 4.</b> Pd dispersion, average particle size, number of active sites, metallic surface area, and TOF for 5% Pd supported on Ce-MOF, Ce-MOF-PRGO, and RGO. H <sub>2</sub> pulse chemisorption performed at 40 °C. ....             | 90   |
| <b>Table 5.</b> Hydrogenation of vanillin over a series of different catalysts. ....  | 91   |
| <b>Table 6.</b> Palladium oxidation state calculated from Pd 3d XPS analysis of supports with and without HPW loading. ....   | 123  |
| <b>Table 7.</b> BET surface area measurements of 0-20 wt% HPW UiO-66-NH <sub>2</sub> supports without palladium nanoparticles. ....   | 124  |
| <b>Table 8.</b> Acid strength and acidity of 0-20 wt% HPW/UiO-66-NH <sub>2</sub> . ....   | 125  |
| <b>Table 9.</b> Conversion of vanillin and vanillyl alcohol into products with a series of UiO-66-NH <sub>2</sub> supports with and without HPW and palladium nanoparticles. ....   | 126  |
| <b>Table 10.</b> Comparison of TOF based of off palladium content in comparison to recent works. ....   | 127  |
| <b>Table 11.</b> Summary of d-spacing, Pd wt% loading, size, and TOF for GO, GO-PPD, and GO-BZD samples. ....   | 153  |
| <b>Table 12.</b> Comparison of catalytic activity against other carbon-based supports by mol%, conversion%, and turnover frequency (TOF). ....  | 154  |
| <b>Table 13.</b> Recycling and ICP analysis of 3% Pd/GO-BZD ( 0.1 ). Conditions: 0.3 mol% Pd, 0.32 mmol bromobenzene, 0.38 mmol phenylboronic acid, 1 mmol K <sub>2</sub> CO <sub>3</sub> . Microwave Irradiation: 80 °C, 5 m, 3.5W. .... | 155  |

## **Abstract**

### **METAL-ORGANIC FRAMEWORKS AND GRAPHENE-BASED SUPPORT MATERIALS FOR HETEROGENEOUS CATALYSIS**

By: Andrew Lin

A Dissertation submitted in partial fulfillment of the requirements for the degree of Doctor of Philosophy at Virginia Commonwealth University

Virginia Commonwealth University, 2018

Director: Dr. M. Samy El-Shall, Chairman of Department of Chemistry

Nanoparticles are involved in a broad range of applications, including heterogeneous catalysis. Nanoparticles tend to quickly lose their well-defined shapes and facets due to aggregation under duress such as heat.

A series of highly studied materials are explored as support materials for nanoparticle supports. These supports include metal-organic frameworks (MOF), graphene oxide (GO), and a MOF-PRGO (partially reduced graphene oxide) hybrid. The inclusion of a support with the palladium increased lifespan of the catalyst by separation of nanoparticles. The choice of support material not only allowed for supporting of palladium nanoparticles, but allowed for rational catalyst synthesis in order to design catalysts with improved catalytic activity.

CO oxidation, vanillin hydrogenation, and Suzuki cross coupling were studied. For the CO oxidation reaction, a cerium-based MOF, Ce-MOF, is shown to increase activity of palladium nanoparticles by capturing reactant gases and acting as an oxygen reservoir that cycles between (III) and (IV) states while transferring oxygen to palladium nanoparticles at the Pd/Ce-MOF interface. A hybrid Ce-MOF-PRGO was synthesized to increase the surface area and acidity of Ce-MOF materials and was shown to be active for vanillin hydrogenation. Smaller rod-like Ce-MOF crystals were observed, indicating intercalation of crystals on GO. Zirconium-based MOF UiO-66-NH<sub>2</sub> was acidified via incorporation of tungstophosphoric acid (HPW), which increased the selectivity of products by adjusting the mechanistic pathway. GO was partially functionalized with aromatic amines to improve the coupling of bromobenzene and phenylboronic acid. Small amounts of aromatic amines increased the Pd(0) content and decreased nanoparticle size.

## Chapter 1: Introduction

### 1.1 Catalysis

During the transition from alchemy into modern practice of chemistry, the transmutation of commonly available commodities such as copper into gold, was highly coveted.[1] While this was never successful, the mindset for the conversion of abundant resources or compounds into more desirable or value-added products was retained and became a foundation of the field of chemistry.

In modern times, many chemical processes proceed through the usage of a catalyst. A catalyst a substance that lowers the activation energy barrier of a reaction, and hence the free energy requirements of a reaction, to allow for the conversion of starting materials or compounds into chemical products. Catalysts are crucial for the world's economy, and 90% of chemical manufacturing involve catalysts.[2] Pharmaceutical and industrial applications involving catalysts include the conversion of natural gas or biomass into fuel,[3-5] production of plastics,[6] or synthesis of specialty chemicals.[7-8] Two main types of catalysis exist: homogeneous and heterogeneous. Homogeneous catalysis involve reactants and catalysts of the same phase, typically liquid-liquid.

While high heat transfer, fast diffusivity, and defined active sites are properties attributed to homogeneous catalysts,[9] separation of liquid catalysts from liquid products is a costly endeavor. It is difficult to remove a catalyst like  $\text{H}_2\text{SO}_4$  from a reaction, and such a hazardous substance poses an environmental concern. The advantage of heterogeneous catalysts is that the catalyst has a different phase from the reactants. Heterogeneous catalysis is less studied because changes to the catalyst structure is not discrete, which is the case for homogeneous catalysis whereby a structural change can directly be attributed to a change in activity. Heterogeneous

catalysts have much more potential sites, such as edges and planes, where catalysis can occur. Each such site can have different activity and may affect the product formation. Despite being costlier and less well-understood, heterogeneous catalysis is of interest to industries. Heterogeneous catalysts are more readily recovered, such as by centrifugation or with a magnet, and are more easily recycled than homogeneous catalysts.[10]

## **1.2 Nanoparticles**

Nanoparticles have been studied for usage as heterogeneous catalysts.[11] Surface-bound atoms are more reactive than atoms in the center, so the high surface-to-volume ratio property of nanoparticles is highly coveted.[2] The major drawback of metallic nanoparticles as catalysts is directly related to their nature as metals. Nanoparticles lose their well-defined shapes and sizes when exposed to heat or harsh reaction conditions. The aggregation of nanoparticles quickly ends their usefulness as a reusable catalyst.[12-13] This is particularly problematic for nanoparticles whose metal identity is of an expensive nature, such as palladium, gold, or platinum.

## **1.3 Supports**

One method of preventing the aggregation of metal nanoparticles is through the usage of a support. There are a number of supports such as metal-organic frameworks (MOFs) and graphene oxide (GO) that have been well studied for catalyst supports. The benefits of supports such as MOFs is the spatial confinement or physical separation of nanoparticles to prevent aggregation. GO also allows for the dispersion of nanoparticles via nucleation of nanoparticles at defect sites.

MOFs are a relatively new robust class of coordination polymers that are highly crystalline in nature with well-defined cavities or channels. MOF-centric research has become prominent in the past decade.[14-18] These crystals consist of unsaturated metal oxide nodes connected to the hydroxyl bonds of organic linkers, creating 2D or 3D crystallographic structures. High surface

area have been measured for such materials due to the presence of micropores and mesopores. The high surface areas associated with MOFs have applications for gas capture and sequestration,[14, 19] sensing,[20] and catalysis.[21] MOFs are also highly tunable, allowing for pre-synthetic and post-synthetic modification of either the metal clusters, or more commonly, the organic linkers.[22-23] This tunable functionality, such as the functionalization of a MOF by amine groups, is easily exploitable for catalytic purposes because the electronic properties and moieties of the MOF is altered.[24] One of the more important properties of a material involved in an industrial catalytic process are the thermal stability and recyclability of the material. Some MOFs, specifically the MIL and UiO series, are stable until 350 °C and do not degrade in solvent nor the solvent removal process.[25] The catalytic application of utilizing MOFs as a support material for the spatial restriction of nanoparticles within confined cages has been studied. It has been observed that metallic nanoparticle supported within MOFs often have a small size and do not aggregate as quickly under heat. Nanoparticles in this manner have been shown to be recyclable.

Graphene (G) is a conductive honeycomb single layer  $sp^2$  hybridized allotrope of carbon that is not easily dispersible in solution.[26] Graphene oxide (GO) is a relatively high surface area material ( $\sim 600 \text{ m}^2/\text{g}$ )[27] that is similar to graphene, but is less conducting and more easily dispersed in solution due to the presence of oxygen-bearing groups such as alcohols, epoxies, and carboxylic acids. Because of its unique 2D hexagonal linkage of carbon atoms, these carbon-based materials have applications as sensors,[28] electrochemical applications,[29-31] and catalysis.[32] While GO has inferior electrocatalytic properties to graphene due to a due to a high C/O ratio, GO is simpler to make than graphene and is easily reducible into reduced graphene oxide (rGO) by numerous chemical and thermal techniques.[33] The presence of metal nanoparticle precursor salts during reduction of GO allows for co-reduction of salts into nanoparticles and GO into rGO.

During the co-reduction process, the nanoparticles settle on defect sites generated on the surface of GO as the oxygen groups vacate. This allows for the formation of small nanoparticle seeds, which result in high dispersion.[34]

It is possible to combine both the MOFs and GO supports to create a composite material. The graphitic re-stacking of GO is a disadvantage. The low atomic density and low dispersive forces associated with MOFs are also drawbacks.[35] Hybridization of MOFs and GO result in a MOF-PRGO (partially reduced graphene oxide), which has been shown to nullify these drawbacks. The interlayer distance between graphene oxide layers are spaced by the intercalative growth of Ce-MOF crystals. The Ce-MOF gains greater catalyst-support interaction due to interaction with GO sheets. The synergistic effect of the support on nanoparticles is enhanced, resulting in increased dispersion.

#### **1.4 Objectives and Overview**

The overall goal of this work is to synthesize a series of materials to act as supports of palladium nanoparticles. It will be demonstrated that MOFs, GO, and MOF-PRGO composites are useful materials for dispersing palladium nanoparticles in a manner that would extend their lifetime as catalysts for a wide range of applications. Three main objectives are achieved: 1) the loading of palladium nanoparticles on MOFs, GO, and composites, 2) rational catalyst synthesis to optimize catalyst-support interaction, and 3) characterization of materials.

Chapter 3 begins with the synthesis of a cerium trimesate MOF, Ce-MOF. This material is loaded with palladium using simple microwave irradiation and the 5% Pd/Ce-MOF is used in the catalytic conversion of CO into CO<sub>2</sub> gas. It is demonstrated that this material has higher activity than ceria. This work exploits the unsaturated nature of MOF metal nodes: the cycling of Ce (III) and Ce (IV) metal centers allows for the material to act as a “reservoir” for oxygen, and



has higher activity than traditional nonporous ceria supports, which are reliant on oxygen vacancies.

Chapter 4 expands on Ce-MOF, with hybridization with GO, to create a material with higher surface area. A synergistic effect is observed between Ce-MOF and GO, whereby mesopores are generated at the Ce-MOF-PRGO interface. This synergistic effect leads to the generation of more sites for nanoparticle dispersion. Two regimes of palladium nanoparticle size distribution occurred, with larger particles settling GO and the smaller particle trapped within the confines of the Ce-MOF crystals. The hydrogenation of vanillin into 2-methoxy-4-methylphenol with a series of constituent support components showed that the hybrid was more selective due to the enhanced dispersion and the higher accessible active site.

It was calculated that the hybrid MOF-PRGO support was more acidic than the MOF or the PRGO by nonaqueous n-butylamine titration. It was hypothesized that the acidity of a support plays a role in the vanillin hydrogenation reaction. Chapter 5 describes in detail the acidification of a well-studied zirconium-based UiO-66-NH<sub>2</sub> MOF with tungstophosphoric acid (HPW), which is proposed to alter the pathway of the vanillin hydrogenation reaction. It was noted that high selectivity towards 2-methoxy-4-methylphenol was observed after replacement of palladium nanoparticles with substitute HPW. A significantly cheaper catalyst was developed for vanillin hydrogenation.

Chapter 6 focuses on GO as a support for palladium nanoparticles in the Nobel Prize-winning Suzuki cross coupling reaction of bromobenzene and phenylboronic acid into biphenyl. Benzidine (BZD) and p-phenylenediamine (PPD) have been previously used in the reduction of GO for electrochemical applications. In this work, GO is only partially functionalized to alter the accessibility of palladium nanoparticles to defect sites and to tune nanoparticle size. It was found

that low loadings of PPD and BZD allows for the palladium particles to assume a smaller size, completing the reaction at a faster rate than previously reported.

## Chapter 2: Experimental Methods

This chapter describes the experimental techniques regarding synthesis, reactor setup, and characterization.

### 2.1 Synthesis of MOF and GO Supports

#### 2.1.1 GO Oxide Synthesis

GO was synthesized using a modified Hummers' method.[36] 115 mL  $\text{H}_2\text{SO}_4$  was cooled to 0 °C in an ice bath under stirring. 2.5g  $\text{NaNO}_3$  was crushed into a fine powder and slowly added into the cold  $\text{H}_2\text{SO}_4$  solution. After 20 min, 5g graphite was added, followed by slow addition of 15g  $\text{KMnO}_4$ . After 20 min, the ice bath was removed, and the mixture proceeded at 32-38 °C for 3 hours with vigorous stirring. Afterwards, 230 mL of hot DI water was added to the viscous slurry, and the exothermically achieved 80 °C was maintained for 30 min as the solution turned brown. After 20 min, 8 mL of 30%  $\text{H}_2\text{O}_2$  was slowly added to stop the reaction. The solution achieve a light gold color.

The synthesized GO was washed with 5L of hot DI water and dried over three days at 60 °C.

#### 2.1.2 Pd/Ce-MOF Synthesis

4.04g  $\text{Ce}(\text{NO}_3)_3 \cdot 6\text{H}_2\text{O}$  (10.0 mmol) and 1.40 g trimesic acid (6.67 mmol) were added to a 60 mL solution of DMF and sonicated until dispersion.[37] The mixture was transferred to a 100 mL teflon autoclave sealed chamber and heated at 100 °C for 24 h. The white powder product was centrifuged with DMF to remove unreacted molecules and washed twice with ethanol to ensure removal of guest DMF molecules. The crystalline white powder was recovered and dried overnight at 80 °C.

100 mg of the Ce-MOF powder was dispersed in 40 mL of DI water via sonication for 30 minutes. Palladium nitrate was added to the solution and stirred for 4 h. The palladium ions were reduced by 80uL hydrazine hydrate (HH) under microwave irradiation conditions for 90s (10s intervals). A 1000W microwave oven was used. The 5%Pd/Ce-MOF catalyst was washed twice with ethanol and dried in an oven at 100 °C for 24 h.

### **2.1.3 Pd/Ce-MOF-rGO Synthesis**

1.0 g  $\text{Ce}(\text{NO}_3)_3 \cdot 6\text{H}_2\text{O}$  (2.5 mmol) and 1.40 g trimesic acid (4.8 mmol) were added to a 20 mL solution of DMF and sonicated for 15 min until dispersion. The mixture was transferred to a 50 mL roundbottom flask and heated under reflux at 120 °C for 24 h. Afterwards, the powder was washed repeatedly with DMF to remove unreacted ligands and then washed with ethanol several times to evacuate guest molecules. The recovered crystalline powder was dried at 100 °C for 12 h prior to usage.

The one-pot synthesis of Ce-MOF-rGO follows a similar procedure: 1.5-50 wt% GO is added to the reaction mixture of  $\text{Ce}(\text{NO}_3)_3 \cdot 6\text{H}_2\text{O}$  and trimesic acid and sonicated to ensure full dispersion prior to reflux.

A physical mixture of the Ce-MOF + rGO was made by mixing formed white Ce-MOF crystals and dark brown GO sheets (12.5 wt%). The mixed powder was physically ground with a mortar and pestle until a uniform grey powder was obtained. The obtained physical mixture was used as-prepared.

200 mg of the respective samples was dispersed in 40 mL of DI water via sonication for 30 minutes. Palladium nitrate was added to the solution and stirred for 4 h. The palladium ions were reduced by 50uL hydrazine hydrate (HH) under microwave irradiation conditions for 120s

(30s intervals) with a 1000W microwave oven. The catalyst was washed twice with ethanol and dried in an oven at 100 °C for 24 h.

#### **2.1.4 Pd/HPW/UiO-66-NH<sub>2</sub> Synthesis**

UiO-66-NH<sub>2</sub> was prepared as reported by Katz.[38] 1.25g zirconium (IV) chloride (5.4mmol) and 1.34g 2-amino-terephthalic acid (7.4mmol) was dispersed in 150 mL DMF under heavy sonication in a 250 mL Erlenmeyer flask. 5 mL undiluted HCl was added to the Erlenmeyer flask and capped. The flask was put in an oven and heated at 120 °C for 17h. After cooling, the slurry was washed with 50 mL DMF three times to remove all unreacted ligands. The filtrate was washed and collected in methanol and dried at 100 °C for 24 h to remove all solvent molecules and to activate the material.

Tungstophosphoric acid (HPW) was loaded into each support via impregnation method.[39] 300 mg of the as-synthesized support was dispersed in a 5 mL 1:1 ratio of water and methanol solution under sonication. A range of 5-50% HPW (1-20% by ICP analysis) by nominal weight was added to solution and sonicated for 10 min. The solution was stirred for a total of 8 hours, followed by a quick centrifugation of 1:1 water and methanol at 8000 rpm for 30 seconds to separate the solution into two phases. The aqueous solution was decanted and the filtrate was dried under vacuum overnight at 100 °C. Samples are denoted as x% HPW/UiO-66-NH<sub>2</sub>.

200 mg of the as-synthesized HPW/UiO-66-NH<sub>2</sub> was dispersed into 12 mL ultrapure pure water. Then 0.126 mL of (30 mM) PdCl<sub>2</sub> was added dropwise to the solution under vigorous stirring. This solution was allowed to stir for 20 hours, followed by two rapid washes of water. The water was decanted and the filtrate was dried under vacuum overnight. The yellow powder was heated at 200 °C in 10% hydrogen flow at 20 ml/min for 2 hours to reduce the supported palladium into a Pd(0).

HPW and palladium content were measured by ICP analysis. Samples are denoted as x% HPW UiO-66-NH<sub>2</sub> 0.4% Pd.

### **2.1.5 Pd/GO-PPD/BZD Synthesis**

100 mg GO was dispersed in 60 mL DI water with either 0.025 mmol-6.0 (3-600 mg) of p-phenylenediamine (GO-PPD) or 0.025-0.5 mmol (4-85 mg) of benzidine (GO-BZD). The mixture was sealed in a 100 mL capacity autoclave reactor and heated at 95 °C over the course of 24 hours. The recovered support was carefully washed with DI water and dried overnight at 80 °C. The samples are denoted as GO, GO-PPD (0.025-6.0), and GO-BZD (0.025-0.5) and collectively GO(-PPD/BZD).

20 mg of GO(-PPD/BZD) was dispersed in 15 mL of DI H<sub>2</sub>O and sonicated to ensure dispersion. After measurement of the initial pH of the solution, 0.5 mM NH<sub>4</sub>OH was titrated to increase the pH of each GO(-PPD/BZD) solution to pH 10. [Pd(NH<sub>3</sub>)<sub>4</sub>]<sup>2+</sup> added to each sample to achieve a target of 3 wt palladium, followed by microwave irradiation (MWI) of every support in the presence of 33uL of hydrazine hydrate. The samples were centrifuged twice with water and twice with ethanol at 10,000 rpm followed by overnight drying at 80 °C.

## **2.2 Catalytic Reactions**

### **2.2.1 CO Oxidation**

25 mg of a catalyst is packed into a quartz column with glass wool (Figure 1).[40] The quartz column is filled with glass beads. The tube is inserted into a tube furnace with controlled temperature ramping. The flow of 4% CO / 20% O<sub>2</sub> / 80% He gas is inserted in one end, and a thermocouple detector is placed near the catalyst to determine sample temperature. The other end of the quartz tube is connected to an IR detector (ACS, Automated Chemical Systems Inc.) that

measures the change in flow composition from CO into CO<sub>2</sub> that interfaces with a computer for recording. LabVIEW is used to record conversion of CO as a function of temperature.

In a typical reaction, the gas mixture is flowed over the supported catalyst as the temperature of the reaction is ramped. The gas mixture is set to flow at 100cc/min, which is controlled by MKS digital flow meters. All catalytic activities were measured after an initial heat treatment of the catalyst at 110 °C to ensure activation of materials.

### **2.2.2 Vanillin Hydrogenation**

300 mg vanillin (2 mmol) is added to 20 mL of DI water and stirred for 10 min. Afterwards, 50 mg of catalyst (1:200 palladium catalyst:substrate ratio) is added and sonicated until full dispersion. The solution is transferred to an autoclave reactor chamber, which is sealed, pressurized with 1 MPa H<sub>2</sub> gas, and heated at 100 °C for 2 h with 960 rpm stirring (Figure 2). A collection valve is used to collect samples for GC-FID analysis at pre-determined intervals.

### **2.2.3 Suzuki Cross Coupling**

0.3 mol% supported palladium was dispersed in 4mL of 50% ethanol. 0.32 mmol bromobenzene (34uL) and 0.38 mmol phenylboronic acid (47 mg) were added to the solution and briefly sonicated to ensure good dispersion of reactants. 133 mg of K<sub>2</sub>CO<sub>3</sub> was then dissolved and the solution was stirred at room temperature at 500 rpm. At predetermined intervals, a small aliquot of the solution was drawn and analyzed by GC-FID to determine the conversion percentage of reactants into biphenyl.

## **2.3 Instrumentation**

X-ray diffraction (XRD) patterns were collected from a PANalytical MPD X'Pert Pro equipped with a copper filter (Cu  $k\alpha$ ,  $\lambda = 1.54 \text{ \AA}$ ) at 45kV and 40 mA with a scan speed of 2.5°

20/min. FTIR spectra were collected with a Thermo Scientific Nicolet iS50 FT-IR. Diamond attenuated total reflectance (DATR) was used for MOF samples. GO samples were crushed and mixed with KBr to collect transmissions scans. X-ray photoelectron spectroscopy (XPS) spectra were obtained using the ThermoFisher Scientific ESCALAB 250 with a microfocused monochromated AlK $\alpha$  X-ray source (15 kV) and a double-focusing full 180° spherical sector electron analyzer. TEM images were obtained using the Jeol JEM-1230 Transmission Electron Microscope with the Gatan Orius SC1000 side mount CCD camera at 120 kV. ICP confirmation of palladium content was performed on an Agilent Technologies 5110 ICP-OES equipped with SPS4 Autosampler accessory. Axial and radial detection were utilized. A 6890N GC equipped with a HP-5 mS column and FID was used to separate and quantitate conversion of reactants into products. A Micromeritics AutoChem 2920 II was used for reduction of palladium. BET analysis was performed on a Micromeritics 3Flex system. Samples were degassed under vacuum for 12 h at 190 °C prior to N<sub>2</sub> adsorption isotherms, which were measured at -196 °C.

## **2.4 Techniques**

### **2.4.1 n-Butylamine Titration**

30 mg of catalyst without palladium is soaked in 15 mL acetonitrile for 3 hours. Afterwards, an electrode was immersed and stabilized in solution for 20 minutes followed by a titration at a rate of 50 $\mu$ L/min with a 0.05 M n-butylamine titrant in acetonitrile. An electrode was used to measure mV readings; all readings were taken after ten minutes of stabilization. Acid strength, E<sub>i</sub> (mV), and acidity (mmol/g) were determined by initial mV reading and titration until saturation. The acid strength of acid sites were indicated from the initial electrode potential. The endpoint of titration indicated the total number of acid sites.[41]



### **2.4.2 Pyridine Adsorption**

30 mg of each sample was degassed under high vacuum at 120 °C for 12 h. The samples were then soaked in 0.1 mL dry pyridine in a sealed system for 12 h. Afterwards, the samples were heated at 70 °C under vacuum to evaporate physically adsorbed pyridine from the surface of the MOF. The samples were analyzed by FT-IR to determine the Brønsted/Lewis acid sites ratio.[42]

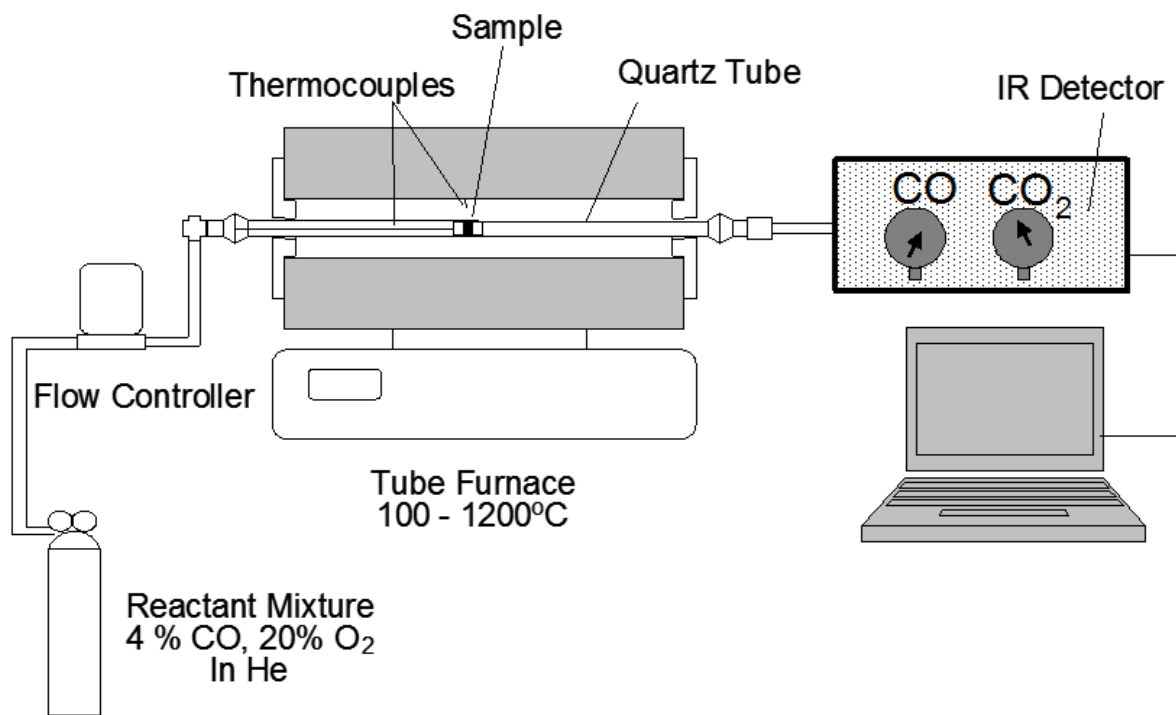


**Figure 1.** CO oxidation reactor configuration.

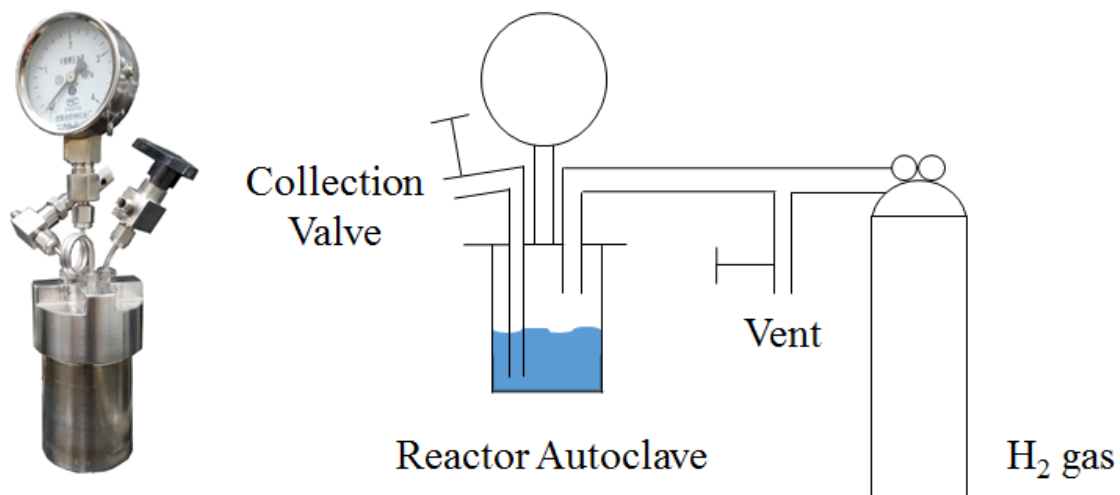


**Figure 2.** Vanillin hydrogenation reactor.

## **Chapter 3: Palladium Nanoparticles Supported on Ce-Metal–Organic Framework for Efficient CO Oxidation and Low-Temperature CO<sub>2</sub> Capture**

This chapter is based on the publication “Palladium Nanoparticles Supported on Ce-Metal–Organic Framework for Efficient CO Oxidation and Low-Temperature CO<sub>2</sub> Capture” by Andrew Lin, Amr A. Ibrahim, Pezhman Arab, Hani M. El-Kaderi, and M. Samy El-Shall, which was published on May 2017 in ACS Applied Materials & Interfaces.[43] This chapter has been re-written to departmental dissertation guidelines.

### **3.1 Introduction**

MOF-based supports for palladium nanoparticle catalysts have been demonstrably effective for a wide variety of liquid phase reactions such as hydrogenation, oxidation, and polymerization reactions.[42, 44-48] Such catalysts have also been effectively utilized and optimized for selectivity, in terms of both chemoselectivity and regioselectivity, such as in the selective hydrogenation of cinnamaldehyde, a compound with both an alkene and a carbonyl group, into hydrocinnamaldehyde and cinnamyl alcohol, respectively.[49] MOFs have also been shown to be useful for critical reactions such as oxygen reduction reaction and generation of hydrogen by photocatalysis.[50-52] The key denominator of these reactions is that they are liquid-phase reactions. Relatively fewer gas-solid phase reactions have been investigated using such MOF catalysts.[42, 53-57] There are comparatively few gas-solid phase reactions when compared to well-studied liquid-solid phase reactions because such reactions require higher temperatures.

There are few studies of the catalytic oxidation of CO gas into CO<sub>2</sub> gas using MOF-based supports for palladium nanoparticles.[55] CO is a toxic gas with serious industrial, environmental, and health concerns. This toxic gas needs to be purified from H<sub>2</sub> streams used in fuel cell applications because of its poisoning effects on the performance of fuel cells and also needs to be

purged from enclosed indoor spaces due to its crippling impact on living organisms. Many reports have provided wonderful catalysts for the conversion of CO gas into CO<sub>2</sub> gas,[58] but the generation of CO<sub>2</sub> is not environmentally friendly either. Catalytic oxidation of CO is an excellent method for elimination of this toxic gas, but the generated product is not typically addressed. Generated CO<sub>2</sub> is a greenhouse gas that must be mitigated for climate change concerns, and MOFs were chosen for this study particularly for this reason. MOFs are porous materials that have been well-studied for sequestration or capture of such gases. The development of a MOF that can induce low temperature CO oxidation that is simultaneously capable of CO<sub>2</sub> gas sequestration makes a highly versatile MOF in the face of modern global challenges. Such a MOF capable of this dual application is of immense interest to a wide variety of fields, such as the conversion and removal of toxic gases generated and release into the atmosphere by combustion, fuel cell performance longevity, or to treat air pollutants.[59-60]

Ceria, CeO<sub>2</sub>, is a well-studied support for palladium nanoparticles for the catalytic oxidation of CO. CeO<sub>2</sub> can act as both a support or it can serve as the actual catalyst.[61-62]

This is not because CeO<sub>2</sub> is a high surface area material but rather because of the presence of oxygen vacancies that are present in the lattice in tunable quantities. Figure 3 demonstrates the mechanism of CO oxidation: an oxygen molecule is adsorbed onto the surface of a catalyst, typically palladium, and a CO molecule is adsorbed as well. The adsorbed oxygen is transferred from the catalyst to the CO molecule, and a radical oxygen is left on the surface of the catalyst, which quickly binds to a second CO molecule.[61] Figure 3 shows the mechanism on the surface of CeO<sub>2</sub> with oxygen vacancies present. The same reaction principle applies; given the lack of palladium, oxygen vacancies attract molecular oxygen, which allow for the formation of radical oxygen that drive the oxidation of CO into CO<sub>2</sub>. The oxygen storage capacity (OSC) of CeO<sub>2</sub>

allows for this material to act as a catalyst for this reaction, and the main reason ceria is a well-studied support for palladium nanoparticles for CO oxidation is due to the synergistic effect between the catalyst and the support.[63] This synergistic effect promotes the reactivity of the catalyst.

Rather than exploit the OSC of ceria supports to enhance the activity of palladium nanoparticle catalysts, a porous cerium-based MOF support was synthesized. The design strategy of this catalyst was based on the hypothesis that a cerium-based MOF could act similarly to ceria. However, higher surface area and gas storage capabilities are the primary benefits of a MOF over a metal oxide, so this MOF was designed with such intentions. A cerium-based MOF would have high affinity for oxygen due to the presence of cerium f-orbitals and could enhance the CO oxidation activity of supported palladium nanoparticles. Of all lanthanide metals, only cerium is easily able to achieve a stable 4+ state. Most lanthanide elements have only 3 valence electrons, but cerium is able to achieve a stable 4+ state because of the stability of the empty f-orbital shell.[64] Cerium is expected to store oxygen because MOFs are, by definition, organic linkers coordinated to unsaturated metal centers. Lanthanide MOFs are less studied than MOFs with a metal identity of more common transition metal elements, such as titanium, zirconium, and copper. One other imperative advantage of a cerium-based MOF over CeO<sub>2</sub> is the ability to adsorb and sequester generated CO<sub>2</sub>.

The cerium-based MOF selected for this application, {[Ce(BTC)(H<sub>2</sub>O)]DMF}<sub>n</sub>, has a polymeric assembly of cerium metal clusters coordinated to trimesic acid (benzene-1,3,5-tricarboxylic acid) organic linkers.[37] The structure of this MOF, referred to as Ce-MOF, is illustrated in Figure 4. The structure has a highly dense homogenous distribution of cerium sites. The affinity of unsaturated cerium nodes provide an excellent opportunity to deposit palladium

nanoparticles. The CO molecules are expected to efficiently adsorb onto the palladium and the cerium interface is expected to capture oxygen and to act as an oxygen reserve.

The Pd/Ce-MOF material is synthesized by using hydrazine hydrate (HH) to simultaneously activate the pores of Ce-MOF and reduce Pd(NO<sub>3</sub>)<sub>2</sub> by rapid chemical reduction with microwave irradiation (MWI). MWI assists the chemical reduction of palladium salt into palladium nanoparticles when HH is used as a reducing agent. This is due to achievement of supersaturation under rapid heating which results in rapid nucleation of nanoparticles. This method of reduction results in uniform and rapid heating of the reaction mixture, which results in palladium quickly reducing.[65-66] The fast generation of a supersaturated solution of palladium atoms result in rapid nucleation of palladium seeds within the pores and on the surface of the Ce-MOF.[42, 59-60] Additionally, this method of reduction of palladium has a side effect on the Ce-MOF crystals, whereby MWI heating removes coordinated DMF molecules around the cerium metal centers.[66] This results in higher surface area and institutes higher accessibility of pores for catalytic applications.

### **3.2 Characterization**

It is important to distinguish the difference between CeO<sub>2</sub> and Ce-MOF through a series of characterization. The XRD diffraction patterns shown in Figure 5 show the characteristics peaks for Ce-MOF. Peaks appear at 8.4, 10.6, and 18.1° 2θ, which are indicative of an excellent degree of crystallinity; furthermore, these peaks are in good agreement with literature results for Ce-MOF.[67] The lack of a strong peak at 27° indicates that there was no formation of CeO<sub>2</sub> and that the material is a MOF. Figure A1 shows that expected XRD diffraction patterns for CeO<sub>2</sub> are completely different. Low angle peaks (2-10°) are for the organic component of MOFs, indicating successful coordination of trimesic acid with cerium nodes. It can also be seen that the loading of

5% palladium into Ce-MOF did not distort the crystal lattice: the retained crystallinity also implies that the material is not damaged nor destroyed in the presence of a strongly reducing HH.[67]

The FTIR spectrum of the Ce-MOF support is shown in Figure 6, which shows the interaction between the organic linkers to the metal nodes. The spectrum shows that the dominant characteristics peaks for the  $\text{COO}^-$  (asymmetric vibrations at  $1612\text{ cm}^{-1}$  and symmetric vibrations at  $1435\text{ cm}^{-1}$  and  $1373\text{ cm}^{-1}$ ) groups of trimesic acid. Low intensity bands for Ce-O stretch vibrations are observed between the ranges of  $500\text{-}700\text{ cm}^{-1}$ . The presence of DMF in the Ce-MOF crystals is evidenced by the C=O vibration at  $1666\text{ cm}^{-1}$ . This indicates that the polymeric network is stabilized by the presence of adsorbed solvent molecules, as does the strong peak at  $3450\text{ cm}^{-1}$ , which is attributed to superficial physically adsorbed water molecules. MWI treatment results in the loss of stabilizing DMF molecules (Figure A2).

The Raman spectrum of Ce-MOF is shown in Figure 7. The spectrum shows five distinct peaks for this material at  $800$ ,  $1000$ ,  $1385$ ,  $1470$ , and  $1600\text{ cm}^{-1}$ . These peaks have been previously reported in literature for Ce-MOF.[68] The peak at  $1470\text{ cm}^{-1}$  is for a C-O symmetric Raman shift.

The needle-like Ce-MOF crystals are shown in Figure 8. The synthesized MOF crystals are vastly different from  $\text{CeO}_2$  particles, which are generally spherical in nature. Figure 8a and Figure 8b shows the as-prepared Ce-MOF crystals with a length of  $2\text{-}6\mu\text{m}$ . Figure 8c and Figure 8d show the Ce-MOF crystals after introduction of palladium nanoparticles after MWI in the presence of HH. The needle shape is retained with no damage to crystal, as expected from XRD pattern analysis (Figure 5). It is clear from the micrographs that this method of chemical reduction results in homogeneous distribution of palladium nanoparticles across the Ce-MOF crystals. The average size of palladium nanoparticles deposited on the Ce-MOF was determined to be approximately  $8 \pm 2\text{ nm}$ . The full palladium nanoparticle size distribution is shown in Figure 9.



XPS measurements were performed to determine the chemical composition of the Ce-MOF materials before and after loading of palladium. Such measurements are critical to the nature of the work, not only to determine the Pd(0) percentage composition but to confirm the cerium is unsaturated and capable of capturing oxygen. The C 1s spectra of the Ce-MOF material and 5% Pd/Ce-MOF material are shown in Figure 10. The expected  $sp^2$ -bound carbon peak is present at 284.5 eV. The C 1s spectra indicate both samples show peaks correlated to oxygen at 286.3 eV. Peaks for C-OH, C-O, C=O, and HO-C=O are found at 285.6, 286.7, 287.7, and 289.0 eV, respectively.[66] All carbon peaks are retained in similar intensity before and after loading of palladium (Figure 10A and Figure 10B).

Three doublets are observed for cerium in Figure 11 for  $3d_{5/2}$  at 882 (v), 885 (v'), and 888 eV (v'') and for  $3d_{3/2}$ , at 900 (u), 904 (u'), and 906 (u''). The u/v'' and u'/v'' spinning-orbit pairs are characteristic of  $Ce^{4+}$  3d states.[69] The appearance of a shoulder in the XPS spectra for the cerium-based MOF at 885 eV (u') and its respective spinning pair at 904 eV (v') are assigned to the  $Ce^{3+}$  3d states, confirming the presence of unsaturated cerium metal within the MOF.[70] This suggests the successful synthesis of an orderly MOF. The confirmation of  $Ce^{3+}$  is also important to prove the capture and transfer of oxygen, which would result in a cycling between Ce(III)/Ce(IV) oxidation numbers during the catalytic reaction on the unsaturated metal centers.

Figure 12 shows the XPS spectrum for 3d Pd in the 5% Pd/Ce-MOF sample. The binding energy of Pd(0) is at 335.8 eV and 340.1 eV, and the atomic ratio of Pd(0) to Pd(II) is 1.37.[66] Pd(II) is present in the samples in the form of PdO, which is surface oxidized palladium nanoparticles. The serendipitous formation of a layer of PdO is expected to act as a reservoir for oxygen that can be released during the catalytic oxidation of CO gas.

Figure 13 shows the thermal stability of the Ce-MOF and 5% Pd/Ce-MOF samples by thermogravimetric analysis, where the mass of the sample is measured as a function of temperature, to show decomposition. The thermogravimetric curve for Ce-MOF exhibits several decomposition steps as the temperature is ramped from 50 to 340 °C: at 140 °C, where a small weight loss occurs (~5%), at 240 °C, where 10% weight loss occurs, and at 400 °C, where the sample loses 58% of its weight with respect to the initial weight. The first weight loss at 140 °C is attributed to the loss of water molecules. The second weight loss at 240 °C is due to the partial loss of adsorbed DMF. At 400 °C, all of the DMF molecules are removed, and the sharp decrease in the weight of the sample is due to the thermal decomposition of the MOF where the ligand is decomposed.[37] This results in the total collapse of the network. The collapse of the framework follows the release of DMF, indicating that the adsorbed DMF molecules stabilizes the Ce-MOF crystal structure.

N<sub>2</sub> adsorption-desorption isotherms were collected at 77K and shown in Figure 14. The Ce-MOF is revealed to have a low BET surface area of 62 m<sup>2</sup>/g, which is consistent with previous measurements: this MOF has lower porosity than more well-studied MOFs such as the UiO or the MIL series.[37, 67] Interestingly, isorecticular MOFs with lanthanide metal has a much higher surface area than Ce-MOF despite similar preparations,[67] leading to the conclusion that either cerium is a bulkier molecule or its presence helps the MOF retain DMF by adsorption. The surface area is increased to 89 m<sup>2</sup>/g for the 5% Pd/Ce-MOF catalyst. This indicates that the microwave treatment during MWI for reduction of palladium assisted in the activation of Ce-MOF by removal of impurities from the pores of the MOF material.

In addition to using Ce-MOF as a support material due to its ability to sequester gases, this material is impregnated with palladium nanoparticles and its impact on CO<sub>2</sub> uptake is observed. CO<sub>2</sub> gases must be removed from the atmosphere due to climate change concerns, and removed

CO<sub>2</sub> can potentially be used as a chemical reactant in fuel applications such as CO<sub>2</sub> hydrogenation into methane.[71] Previous reports of doping of porous materials with metallic nanoparticles such as palladium has shown adverse effects on the uptake of gases.[72] Studies have shown that the doping of palladium nanoparticles into redox-active MOFs increases hydrogen storage at the expense of CO<sub>2</sub> uptake.[73] The inhibition of CO<sub>2</sub> uptake in such a material is detrimental to the sequestration capabilities of a porous MOF in this particular application. While palladium nanoparticles is expected to provide additional sites for interaction with hydrogen, counter ions and other species inside the pores of MOFs have been shown to inhibit the uptake of CO<sub>2</sub>. [74]

In this case, the inclusion of palladium nanoparticles within Ce-MOF increases the CO<sub>2</sub> uptake at 273K. This is shown in Figure 15 for Ce-MOF and 5% Pd/Ce-MOF samples. While as-prepared Ce-MOF shows an uptake of 1.7 mmol/g uptake at 1.0bar, the uptake is improved after palladium loading. 5% Pd/Ce-MOF shows an increase in CO<sub>2</sub> uptake to 3.5 mmol/g under the same conditions. This is considered significant; pristine UiO-66 has a maximum of 2.2 mmol/g with a surface area of between 800-1000 m<sup>2</sup>/g, as measured by N<sub>2</sub> adsorption-desorption BET surface area analysis.[75] Figure 15 also shows that the CO<sub>2</sub> isotherm for Ce-MOF, while fully reversible, has a pronounced hysteresis. This is due to the ultra-narrow pores of Ce-MOF restricting the surface area and thus limiting the active sites of the material and also due to the strong affinity for CO<sub>2</sub> molecules by the MOF. The addition of palladium and simultaneous activation of the material by MWI adds additional adsorption sites for CO<sub>2</sub>, as evidenced by the surface area increase of 62 m<sup>2</sup>/g to 89 m<sup>2</sup>/g, as well as the diminution of the size of the hysteresis. The BET measurements and CO<sub>2</sub> uptake are summarized in Table 1. BET surface area was also measured with CO<sub>2</sub> uptake.

Despite the low uptake of N<sub>2</sub> at 77K, the Ce-MOF support exhibit high CO<sub>2</sub> uptake values at 273K, which support the argument that the material is microporous.[76] Poor N<sub>2</sub> adsorption can be attributed to the Ce-MOF's low diffusivity and the adsorption kinetics of N<sub>2</sub> at 77K.[76-77] This is, again, attributed to the ultra-narrow pores indicated by the CO<sub>2</sub> uptake hysteresis of the Ce-MOF prior to activation by MWI. Because of the higher affinity of the material for CO<sub>2</sub> as a probe molecule rather than N<sub>2</sub>,[76] CO<sub>2</sub> adsorption-desorption was also measured. The surface area of the Ce-MOFs by CO<sub>2</sub> isotherms were collected at 273K and are shown in Table 1. The surface area measurements when CO<sub>2</sub> was used as a probe molecule resulted in an increase in the surface area: Ce-MOF was determined to have a surface area of 636 m<sup>2</sup>/g and 5% Pd/Ce-MOF was determined to have a surface area of 620 m<sup>2</sup>/g. These may be the true surface area of the material, but the usage of CO<sub>2</sub> as a probe molecule often results in overestimation of surface areas for materials with particularly high binding affinities towards CO<sub>2</sub>. [78] It is believed that the latter is the case due to the ability of the Ce-MOF to capture and to release adsorbed CO<sub>2</sub> molecules during the catalytic process.

### **3.3 Effect of Pd wt% on Catalytic CO Oxidation**

A range of 3-7 wt% palladium was doped into Ce-MOF. Conversion for the catalytic transformation of CO into CO<sub>2</sub> gas was measured as a function of increasing temperature. Figure 16 shows a profile for the conversion of CO into CO<sub>2</sub> gas as a function of ramped temperature for a range of Pd wt% samples. The 3% Pd/Ce-MOF sample achieved 50% (T<sub>50%</sub>) and 100% (T<sub>100%</sub>) conversion of CO into CO<sub>2</sub> gas at 180 °C and 190 °C. The 5% Pd/Ce-MOF sample had improved T<sub>50%</sub> and T<sub>100%</sub> values of 77 °C and 92 °C. A further increase of the palladium content for 7% Pd/Ce-MOF sample had regressive T<sub>50%</sub> and T<sub>100%</sub> values of 140 °C and 148 °C. This is suspected to be due to the aggregation of palladium nanoparticles, which firstly hinder the active sites for

CO oxidation and secondly passivate the surface of the MOF. Passivation of the surface of the MOF inhibits oxygen interaction with Ce-MOF at the palladium-cerium interface, which explains the decrease in activity at higher loadings of palladium. The  $T_{100\%}$  of 92 °C for the 5% Pd/Ce-MOF sample is among the lowest reported for MOF samples. This sample is particularly efficient, even more than optimized palladium-doped CeO<sub>2</sub> samples because the unsaturated cerium centers store oxygen by adsorption. The oxygen is then transferred to the palladium, which has adsorbed CO molecules. The Ce-MOF sample alone did not exhibit any signs of catalytic activity under 200 °C, which is expected. Similar to CeO<sub>2</sub>, although Ce-MOF interacts with oxygen and has excellent CO<sub>2</sub> uptake, it cannot interact nor transfer oxygen to CO without higher temperatures. CO oxidation on non-doped metal oxides such as ceria require temperatures in excess of 400 °C.

The stability and lifespan of the material was tested. The material was observed to retain its activity for 8h when held on-stream at 90 °C. Figure 17 shows that there was no decrease in the catalytic conversion over time. The sample was able to achieve 100% conversion of CO gas into CO<sub>2</sub> gas at 90 °C for the full 8 hours. This is indicative of a few key points: first, the MOF is stable at this temperature, as proven by TGA measurements (Figure 13) and second, the palladium nanoparticles did not aggregate. These two points are the result of a synergistic catalyst-support system that allowed for the low-temperature CO oxidation to occur. MOFs are unfavorable for reactions that require high temperatures because most MOFs undergo thermal decomposition by 350 °C.[76, 79] This is disadvantageous compared to metal oxides, but this disadvantage is mitigated if the catalyst-support interaction is highly synergistic. The temperature requirement of a reaction is decreased to a suitable temperature.

Table 2 shows a comparison of  $T_{50\%}$  and  $T_{100\%}$  values for metals loaded onto a series of MOFs. This comparison shows the relatively low  $T_{50\%}$  and  $T_{100\%}$  of Ce-MOF compared to several

samples. 5 wt% Au nanoparticles with a size of nearly 4.2 nm supported on ZIF-8 was able to achieve a  $T_{50\%}$  value at 170 °C, which is a stark contrast to a  $T_{50\%}$  value at 77 °C achieved by 5 wt% Pd nanoparticles supported on Ce-MOF.[46] The measured surface area of ZIF-8 for that particular study was 1413 m<sup>2</sup>/g, which is significantly higher than the 62 m<sup>2</sup>/g surface area of Ce-MOF. This is further evidence of a synergistic interaction between Ce-MOF and the support palladium nanoparticles. Another study optimized the Pd wt% on HKUST-1 and found that the lowest achievable  $T_{50\%}$  and  $T_{100\%}$  values were 190 °C and 205 °C, respectively, using 1 wt% Pd.[55] It must be noted that the HKUST-1 was partially degraded into copper oxide after the reaction due to the high temperature. Another study with HKUST-1 doped 5% Ag and achieved  $T_{50\%}$  and  $T_{100\%}$  values of 100 °C and 120 °C, respectively, which were more favorable.[56] HKUST-1 is particularly interesting because HKUST-1 and Ce-MOF both share the same trimesic acid linker, and the difference in activity must be attributed to the interaction between palladium and cerium nodes rather than palladium and the organic linkers. 5 wt% Pd, Pt, and Au nanoparticles supported on Ce-MOF were compared in Figure 18. Compared to palladium, neither Pt nor Au are particularly active at the same wt%. 5% Au/Ce-MOF achieved  $T_{50\%}$  and  $T_{100\%}$  values of 170 °C and 240 °C, which is similar to  $T_{50\%}$  and  $T_{100\%}$  values of 170 °C and 210 °C for 5% Au/ZIF-8.[46]

The comparison of MOFs shows two things: MOFs such as MIL-101, MIL-53, and HKUST-1 possess the high surface area advantage of MOFs over metal oxides but do not possess the synergistic effects displayed by Ce-MOF in regards to oxygen capture by cerium nodes. It is evident in this study that a synergy exists between palladium and cerium nodes for this application, as seen from previous cerium-modified HKUST-1 studies.[80] However, in past studies this

resulted in the formation of CuO and CeO<sub>2</sub>. [81-82] The structure of the Ce-MOF crystal is maintained for this catalyst due to the low temperature of the reaction.

### **3.4 Synergistic Effect between Unsaturated Cerium Nodes and Palladium**

The catalyst-support interaction between cerium and palladium is highly synergistic. It has been shown that low temperature oxidation of CO gas into CO<sub>2</sub> gas was achieved with this MOF, but irreproducible for many other MOFs. Most MOFs used for this application decomposed due to high temperatures. HKUST-1 was observed by XRD diffraction to convert into CuO<sub>2</sub> because of the high temperature requirement to achieve a full conversion of gases. [80-82] The Ce-MOF studied here did not decompose into CeO<sub>2</sub> because the reaction temperature was lowered and the stability of the MOF was never jeopardized. Pd/Ce-MOF, in this regard, demonstrate a unique affinity for this particular reaction.

The reason the Pd/Ce-MOF catalyst was able to achieve a low temperature is due to oxygen interaction by unsaturated cerium nodes, which allows the MOF to adsorb oxygen gas, allowing the cerium ion to oxidize from (III) to (IV), similar to OSC properties of CeO<sub>2</sub>. [63] However, unlike CeO<sub>2</sub>, this MOF is more porous and has a higher degree of unsaturation because OSC is dependent of oxygen vacancies, which are typically present in small amounts in the lattice of CeO<sub>2</sub>. During CO oxidation, it is suspected, that the adsorbed oxygen within the Ce-MOF are released when the temperature reaches 373K. The release of this oxygen to the palladium-cerium interface allows for the rapid conversion of CO molecules bound to the surface of palladium into CO<sub>2</sub>. In doing so, the cerium metal in the MOF returns from (IV) back to (III). This cycling of (III) and (IV) states allows for the rapid conversion of CO into CO<sub>2</sub> because the cerium acts as an oxygen reservoir that can capture and transfer oxygen molecules to the palladium active sites at the cerium-palladium interface. Another explanation could be due to electron transfer from palladium

nanoparticles to cerium during the  $Ce^{4+}$  state, resulting in reduction of  $Ce^{4+}$  to  $Ce^{3+}$ .<sup>[83]</sup> In this case, a second electron transfer occurs from  $Ce^{3+}$  to the  $O_2$  adsorbed at the palladium-cerium interface, promoting the formation of an active oxygen species for CO oxidation, as  $Ce^{3+}$  returns to  $Ce^{4+}$ . Despite the lower surface area of this MOF relative to other MOFs such as ZIF-8 and HKUST-1, this material is more active because the cerium plays a role in the reaction, enabling a synergistic effect in the catalyst-support interaction.

This material addresses a concern that metal oxides such as  $CeO_2$  cannot. This 5% Pd/Ce-MOF catalyst is capable of a low temperature full conversion of CO into  $CO_2$  gas by 373K, but it also allows for the capture of  $CO_2$  at 273K. The 5% Pd/Ce-MOF catalyst has a  $CO_2$  uptake of 3.5 mmol/g at 273K, which is impressive compared to other pristine MOFs. For example, UiO-66 has a  $CO_2$  gas uptake of 2.2 mmol/g at 273K.<sup>[75]</sup> This allows for the design of a modular system, one portion with a column packed with this catalyst and inserted into an oven for the conversion of toxic gas into greenhouse gas. As the temperature of the gas is cooled upon leaving the oven, a second cooled column can be packed with this same material to trap incoming  $CO_2$  gases. This can be sequestered for later use, such as when  $CO_2$  gas is required as a chemical feedstock. The hydrogenation of  $CO_2$  into methane is one potential application of this gas.



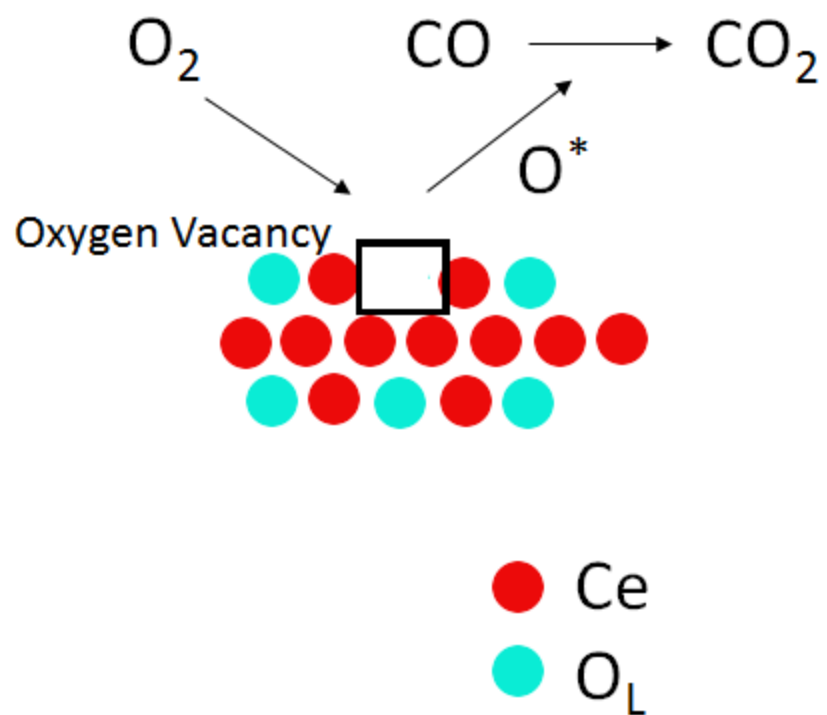


**Figure 3.** CO oxidation of CO into CO<sub>2</sub> mechanism and illustration of oxygen vacancy in CeO<sub>2</sub>.

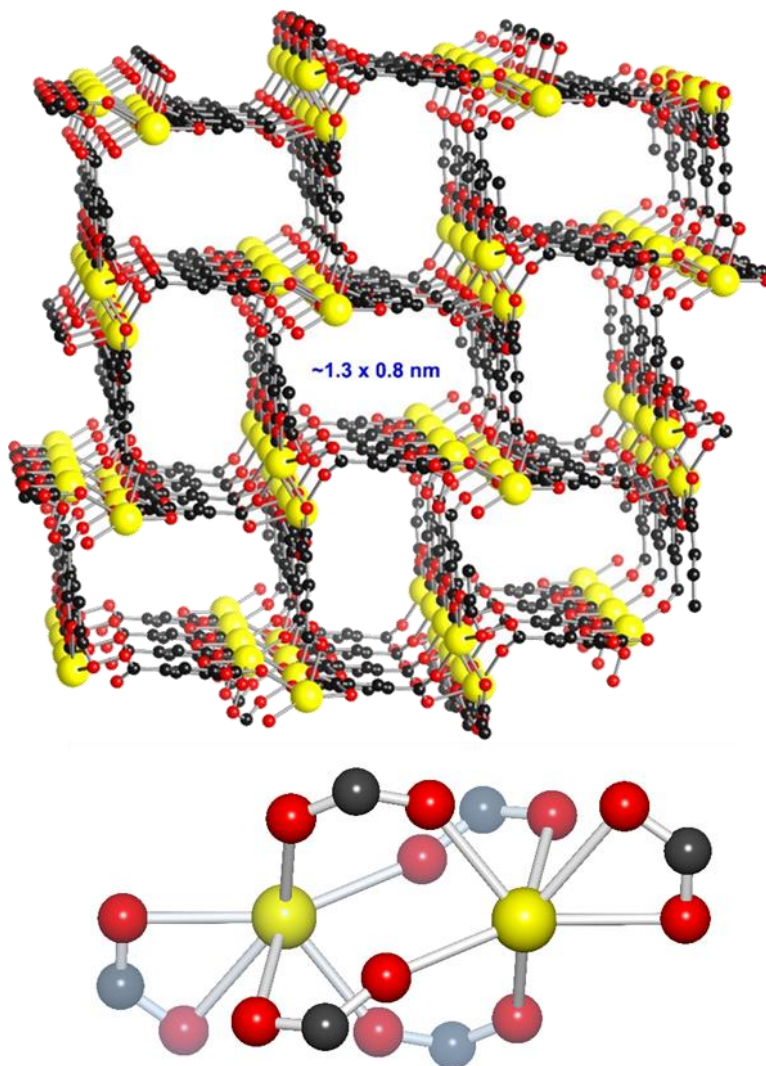


**Figure 4.** Structure and secondary building unit (SBU) of  $\{[\text{Ce}(\text{BTC})(\text{H}_2\text{O})]\text{DMF}\}_n$

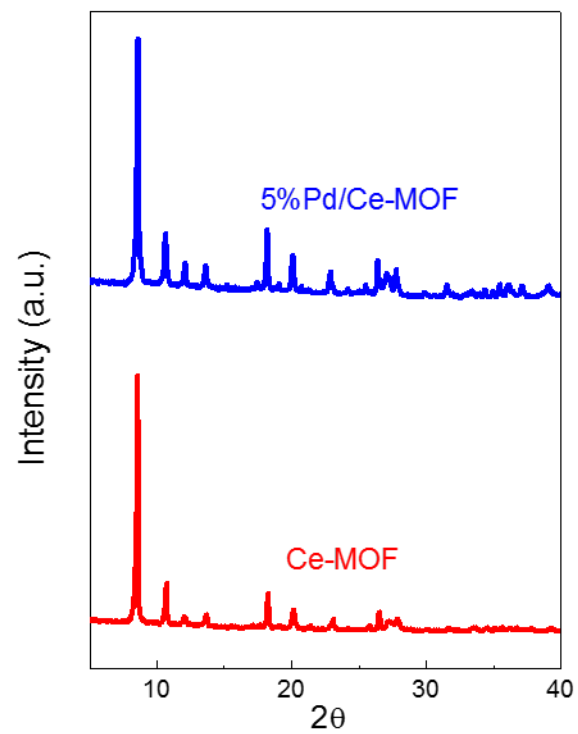


**Figure 5.** XRD diffractogram for Ce-MOF and 5% Pd/Ce-MOF.

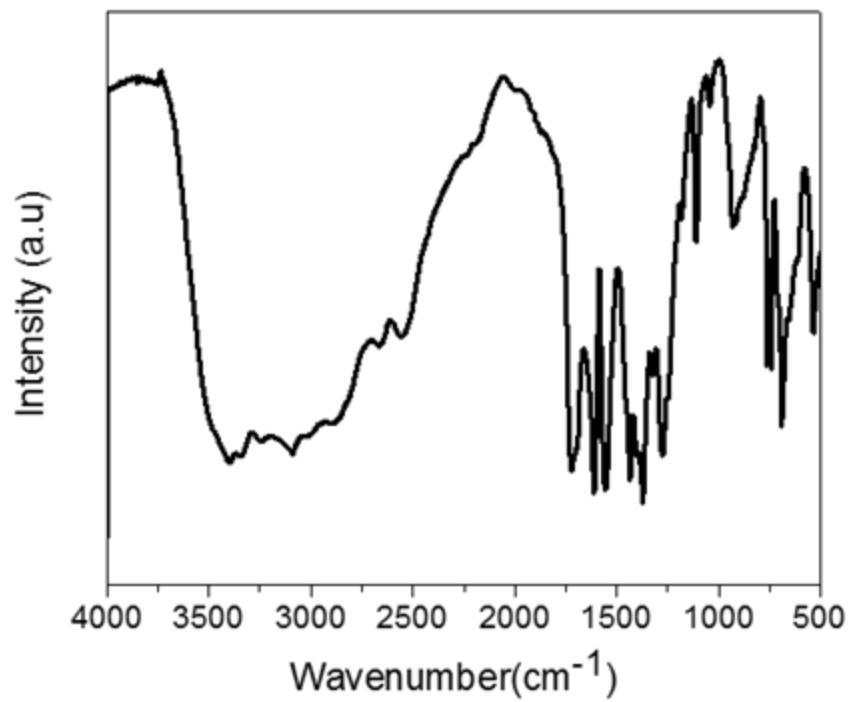


**Figure 6.** FTIR spectra of Ce-MOF.

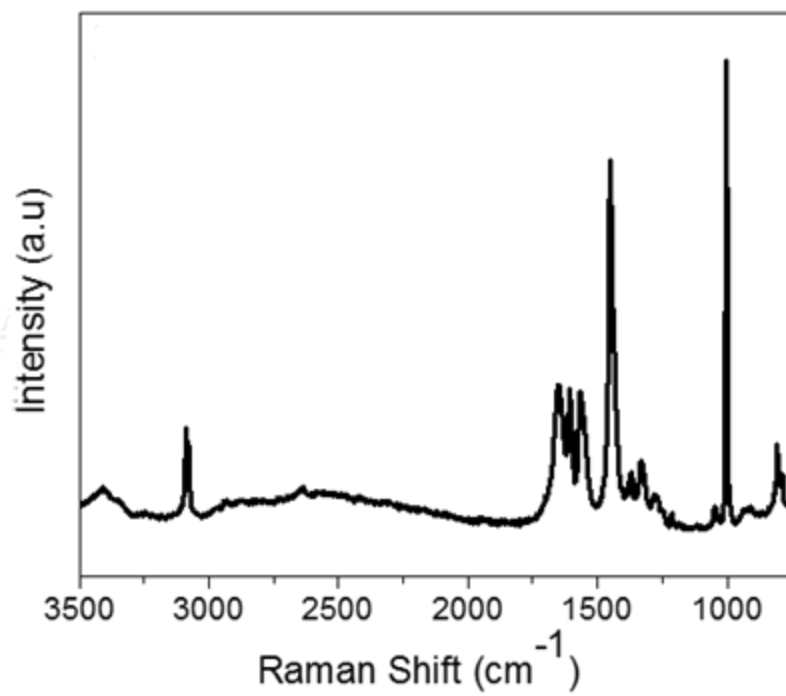


**Figure 7.** Raman spectrum of Ce-MOF.

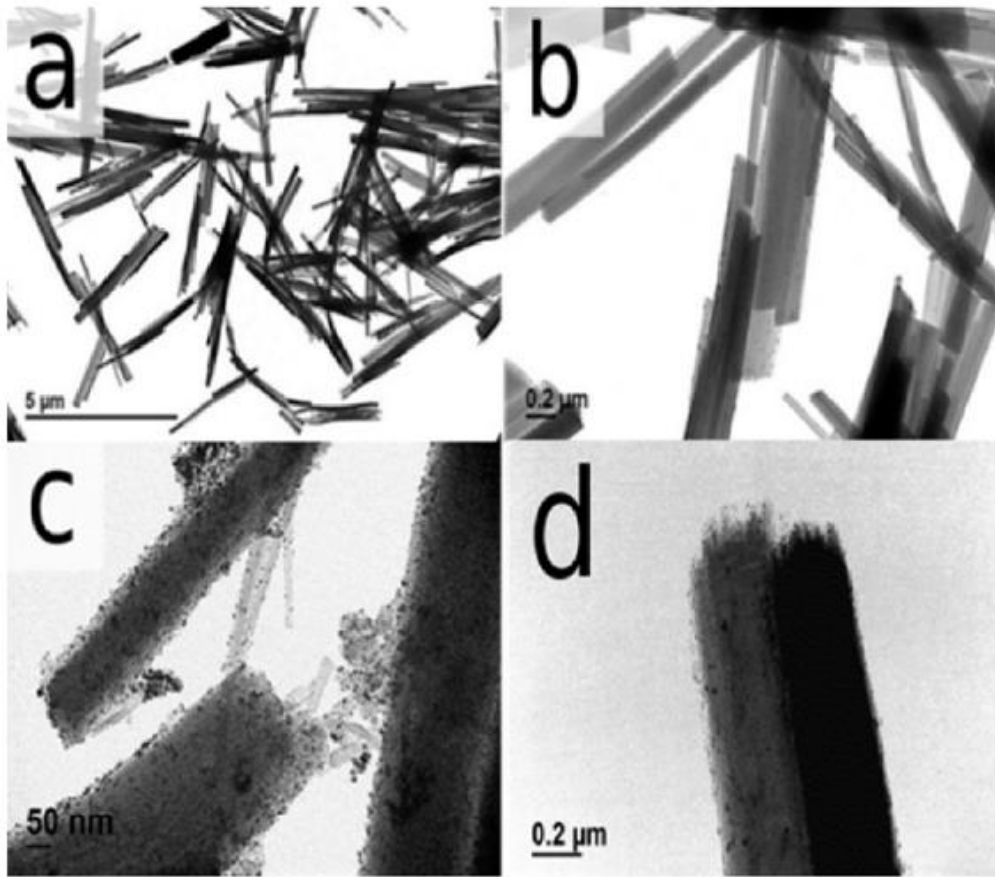


**Figure 8.** TEM images of Ce-MOF (a,b) and the 5% Pd/Ce-MOF catalyst (c,d).

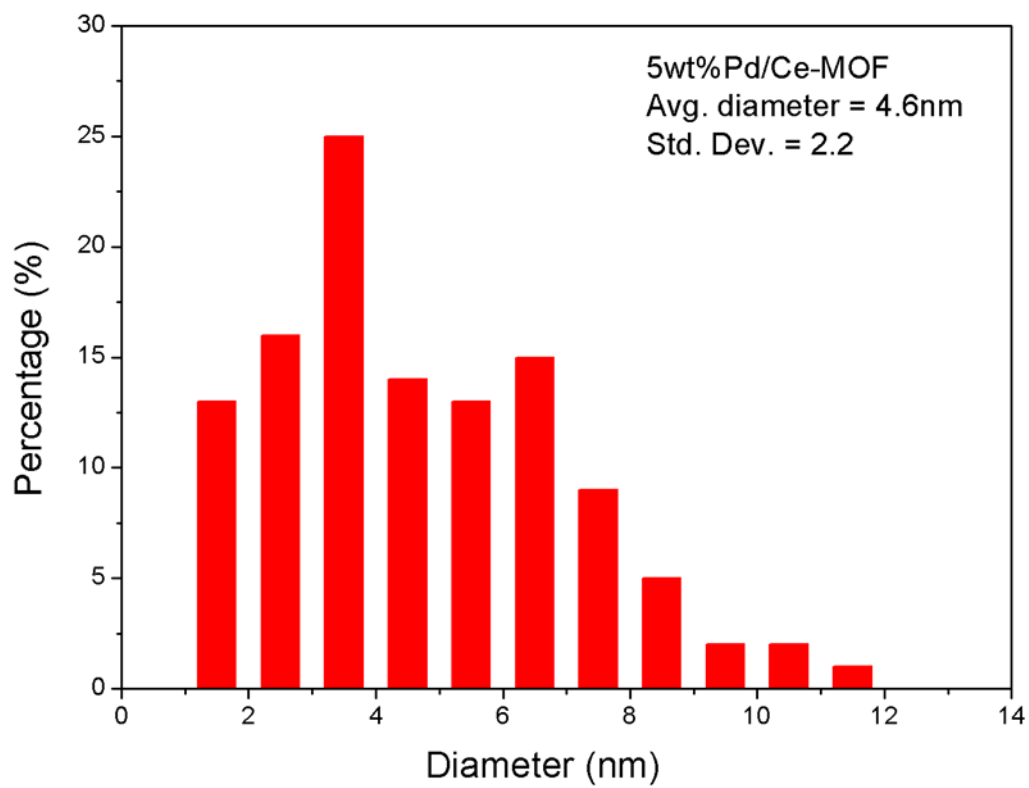


**Figure 9.** Palladium size distribution of palladium nanoparticles supported on Ce-MOF.

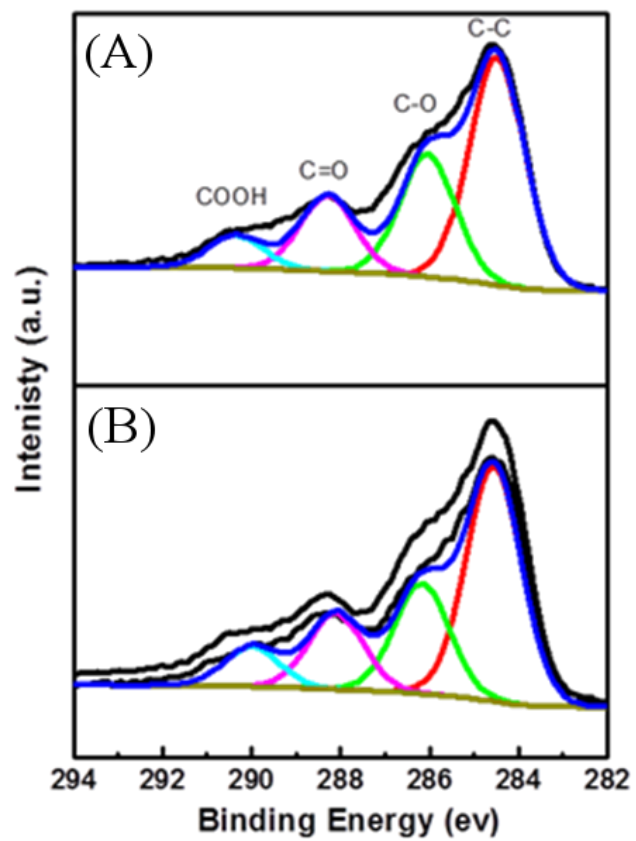


**Figure 10.** XPS C 1s spectra of Ce-MOF (A) and 5% Pd/Ce-MOF (B).



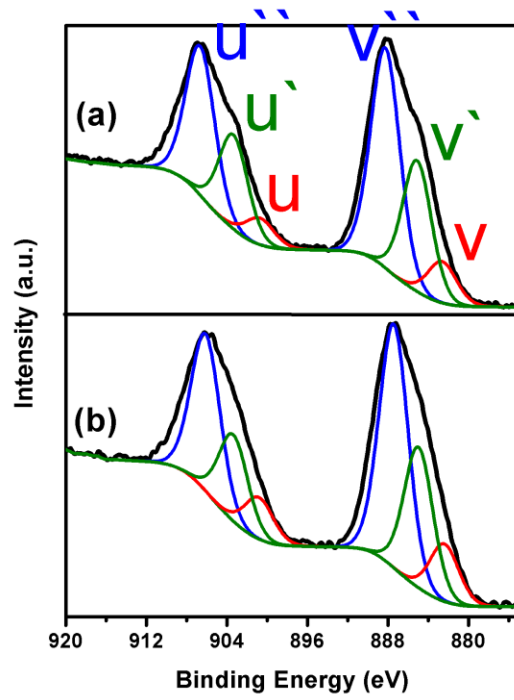


**Figure 11.** XPS Ce 3d spectra of Ce-MOF (a) and 5% Pd/Ce-MOF (b).

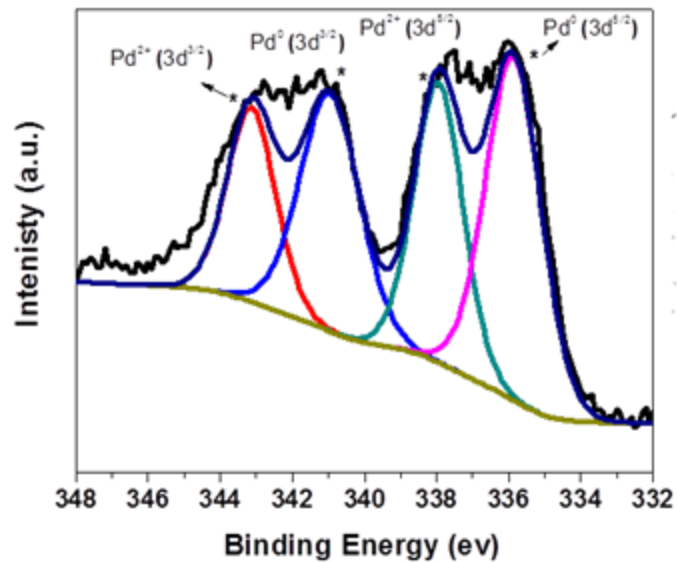


**Figure 12.** XPS Pd 3d spectra of 5% Pd/Ce-MOF.

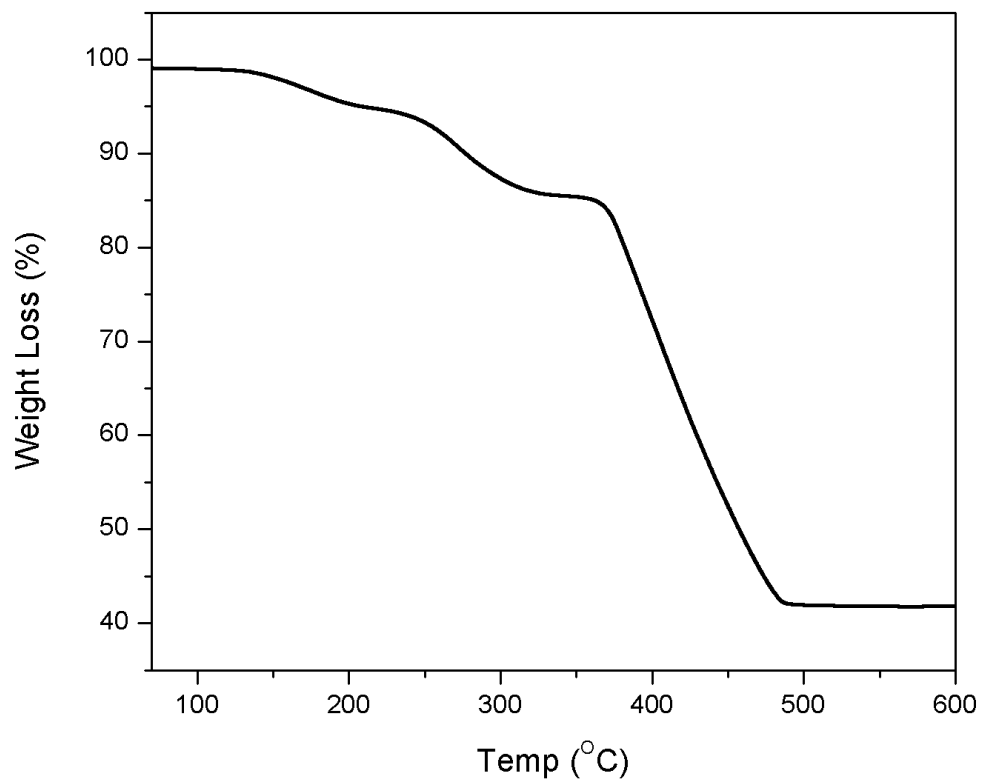


**Figure 13.** TGA plots of Ce-MOF and 5% Pd/Ce-MOF.

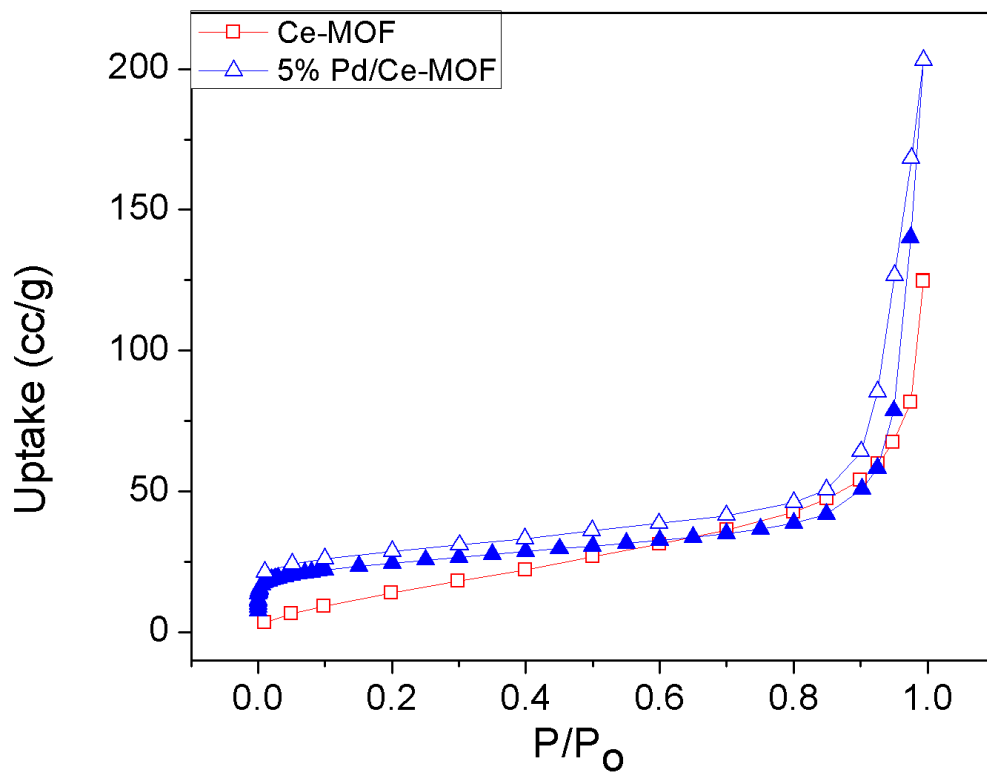


**Figure 14.**  $\text{N}_2$  gas adsorption and desorption isotherms of Ce-MOF and 5% Pd/Ce-MOF.

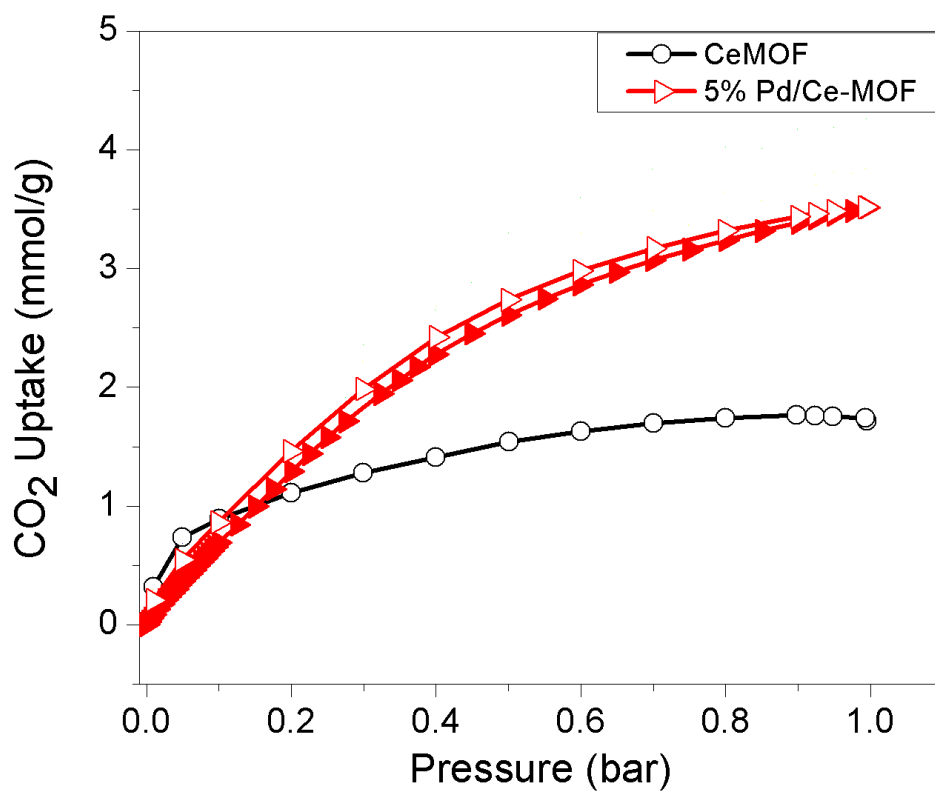


**Figure 15.** CO<sub>2</sub> uptake of Ce-MOF and 5% Pd/Ce-MOF at 273K.

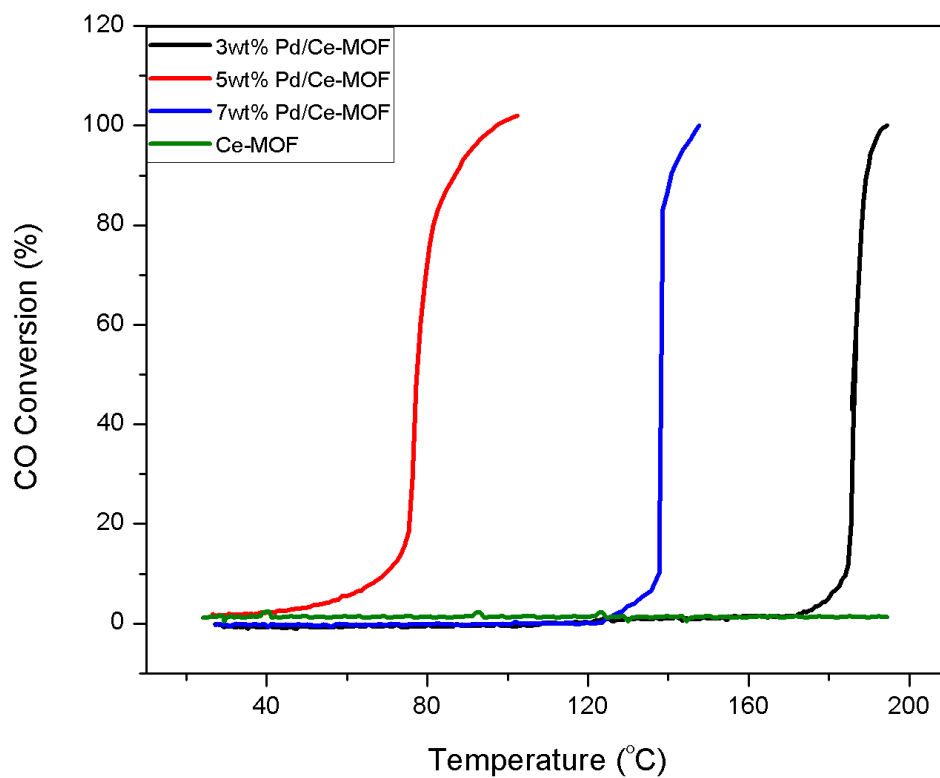


**Figure 16.** CO Oxidation activity of 3-7 wt% Pd/Ce-MOF as a function of temperature ramping for a gas mixture of 4% CO and 20% O<sub>2</sub> in helium balance (25 mg catalyst, flow rate of 100cc/min).

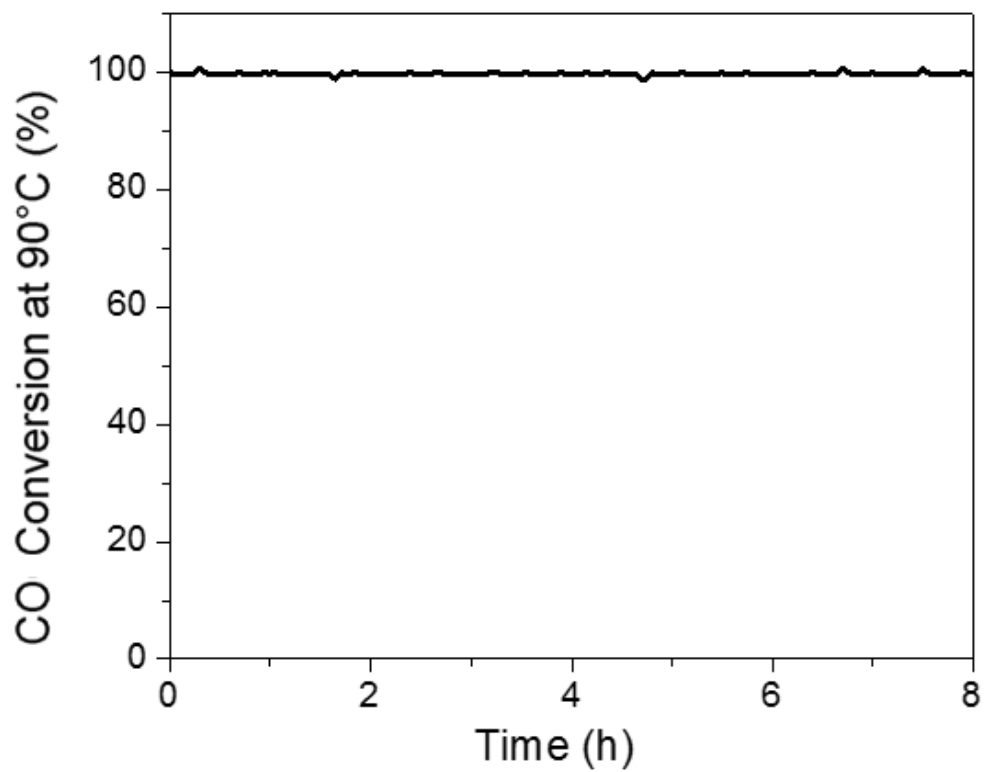


**Figure 17.** CO conversion for 5% Pd/Ce-MOF maintained at 90 °C as a function of time.

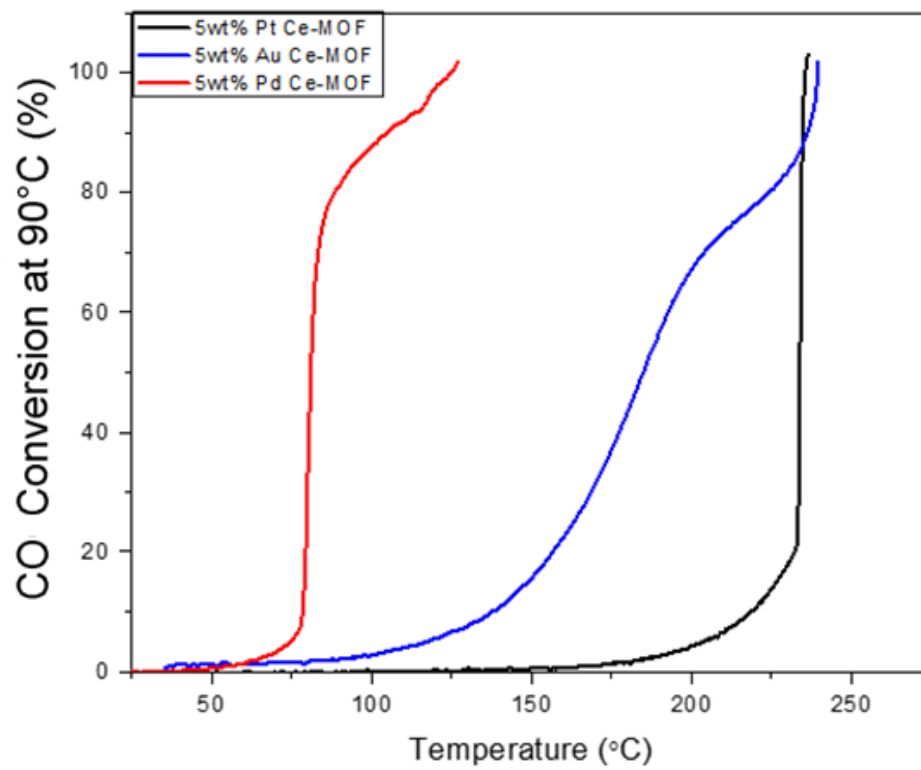


**Figure 18.** CO Oxidation activity of 5 wt% Pd, Pt, and Au on Ce-MOF as a function of temperature ramping for a gas mixture of 4% CO and 20% O<sub>2</sub> in helium balance (25 mg catalyst, flow rate of 100cc/min).



**Table 1.** BET surface area measured at 77K and CO<sub>2</sub> uptake at 273K.

---

| <b>Material</b> | <b>BET Surface Area<br/>(m<sup>2</sup>/g)</b> | <b>CO<sub>2</sub> Uptake<br/>(mmol/g)</b> |
|-----------------|---|---|
| Ce-MOF          | 62.2 (636*)                                   | 1.7                                       |
| 5% Pd/Ce-MOF    | 89.3 (620*)                                   | 3.5                                       |

---

\*BET surface area were obtained by CO<sub>2</sub> adsorption isotherms.

**Table 2.** Comparison of CO oxidation of supported nanoparticles on a series of MOFs.  $T_{50\%}$  and  $T_{100\%}$  are the temperatures for 50% and 100% conversion of CO gas into CO<sub>2</sub> gas.

| <b>Metal wt%</b> | <b>MOF</b>   | <b>T<sub>50%</sub> ( °C)</b> | <b>T<sub>100%</sub> ( °C)</b> | <b>Reference</b> |
|------------------|--------------|------------------------------|-------------------------------|------------------|
| 5% Au            | ZIF-8        | 170                          | 210                           | [46]             |
| 2.7% Pd          | MIL-53 (Al)  | 100                          | 115                           | [57]             |
| 5% Ag            | HKUST-1      | 100                          | 120                           | [56]             |
| 1% Pd            | HKUST-1      | 190                          | 205                           | [55]             |
| 2.9% Pd          | MIL-101 (Cr) | 92                           | 107                           | [42]             |
| 5% Pd            | Ce-MOF       | 77                           | 96                            | This work        |

## **Chapter 4: Palladium Nanoparticles Supported on a Metal-Organic Framework-Partially Reduced Graphene Oxide Hybrid for the Catalytic Hydrodeoxygenation of Vanillin as a Model for Biofuel Upgrade Reactions**

This chapter is based on the publication “Palladium Nanoparticles Supported on a Metal-Organic Framework-Partially Reduced Graphene Oxide Hybrid for the Catalytic Hydrodeoxygenation of Vanillin as a Model for Biofuel Upgrade Reactions” by Amr A. Ibrahim, Andrew Lin, Fumin Zhang, Khaled M. AbouZeid, and M. Samy El-Shall, which was published on November 2016 in ChemCatChem. This chapter has been re-written to departmental dissertation guidelines.

### **4.1 Introduction**

One of the challenges of the 21<sup>st</sup> century is the ongoing investigation for a renewable source of energy. Natural hydrocarbon reserves, in the form of gas, coal, and oil, formed millions of years ago. These reserves are nonrenewable. These hydrocarbon reserves are depleting at an unsustainable rate after only 200 years of usage while rate of consumption continues to increase rapidly despite environmental concerns.[84] Recent research into alternative energy sources have included windmills, solar energy,[85-87] fatty acid methyl esters (FAMES), and bio fuels.[88-90] Windmills, while promising, are not suitable everywhere due to topography, altitude, and wind consistency. Solar energy suffers from the issue of cost and even the best semiconductors have peaked in efficiency. Any steadfast gain in solar cell efficiency is exponentially more costly.[91] Biofuels, the refined hydrocarbon liquid products of biomass, have potential because of renewability and abundance. Biomass upgrade studies often use plant matter with little other value or are a common commodity. Common feedstock include cellulose, corn, rye, oats, and

agricultural residues. Lignin, found in vascular plants and wood alongside cellulose, is one such material that is investigated as a potential renewable feedstock due to its abundance.[92]

However, such materials must be refined. Lignin has very high oxygen content and must be refined.[93] High oxygen content in fuels must be purged because oxygen contributes to lower energy density, instability of the biofuel molecule, and is corrosive towards machinery. Fast pyrolysis is one method of refining such compounds.[93] This method uses very high pressure and temperatures to catalytically upgrade a highly complex and variable structure such as lignin for use as a biofuel. The energy required for the catalytic upgrade process can be reduced with a catalyst, and these lignin upgrading reactions are modelled with oxygen-containing agricultural compounds such as furfural,[94-95] cinnamaldehyde,[49, 96] or vanillin,[97] all of which are common fractionated products of lignin. Vanillin is often used as a model substrate for conversion into 2-methoxy-4-methylphenol because vanillin shares many similar functional groups as lignin.[98]

Heterogeneous catalysts are one method for the conversion of biomass into biofuel. The catalytic activity of a catalyst is highly tunable and can be tailored for applications. For example, a support with a high surface area can better disperse nanoparticles. A support can also be chosen for acid-base properties to affect chemoselectivity of a product.[99] Supports can be modified for a specific application.

Metal oxides are widely used in a wide variety of applications due to their ease of synthesis and excellent activity. However, metal oxides often face problems in terms of selectivity of products.[100-103] These supports are difficult to chemically modify due to inertness at lower temperatures. Modifications in the synthesis procedure of metal oxides only allow for the adjustment of surface area by introducing mesoporosity or macroporosity. As a result of their

limited modifiability, despite their ease of synthesis and wide commercial use, many other materials are emerging as competitors to metal oxides in catalysis.[37, 44, 48, 104-106]

The advantages of MOFs as supports were previously discussed.[44] Chapter 3 was focused on the exploitation of unsaturated cerium centers of a Ce-MOF as oxygen reservoirs. This was a method of enhancing the synergy between the catalyst palladium and the support. Like metal oxides, MOFs have several properties, such as a high surface area from microporosity. The high surface area property of MOFs can be used for specific applications.[48, 104] Unlike metal oxides, a MOF can be modified to induce new properties. Supported catalysts can be rationally synthesized.[107] The interest in MOFs is derived from not just a high surface area and a highly ordered crystal structure; MOFs have tunable pore size and can be chemically modified.[42] There are several ways to incorporate metal nanoparticles within MOFs, such as encapsulation and impregnation.[108-109] Encapsulation, or the *bottle-around-the-ship* method, is the synthesis of nanoparticles as seeds followed by the *in-situ* crystallization of a MOF around the seeds.[108] Impregnation, or the *ship-in-a-bottle* method of palladium loading, is the synthesis of a MOF followed by loading of metal nanoparticles into the crystal structure. There are several sites for nanoparticles to nucleate and impregnate within the pores of a MOF: coordination with unsaturated metal centers or catalytic sites inherently present within the MOFs' structure.[110]

Carbon-based supports, such as graphene oxide, carbon nanotubes, and nitrogen-doped carbons, are another emergent category of supports with highly tunable catalyst-support interactions.[105] Lower olefins, for example have been catalytically converted from CO and H<sub>2</sub> (syngas) using carbon-based nanofibers,[106] and selectivity has been studied for functionalized carbon nanotubes as supports for nanoparticles.[111-112] Graphene has also been considered as

a support material, but despite its high surface area of 2600 m<sup>2</sup>/g and high thermal stability, its applications have been limited due to lack of defect sites.[113-114]

Unlike MOFs, which can provide nucleation sites with unsaturated metal centers and facets, graphene-based materials are highly reliant on defect sites to anchor nanoparticles.[115] Without defects, nanoparticles are loosely attracted by van der Waals forces. Metal nanoparticles need to be anchored. The absence of defect sites allows for only weak catalyst-support interactions.[116] GO, reduced GO (RGO), and partially reduced GO (PRGO) have a higher ratio of surface defects relative to graphene that can be used as nucleation sites for nanoparticles.[117] These defect sites are a means to anchor metal nanoparticles to the surface of these supports to increase the catalyst-support interaction and also to induce new surface functionalities that enhance the synergistic activity of the catalyst.[118] RGO and PRGO have previously been shown to perform the role of support for metallic nanoparticles in heterogeneous systems.[119-121] The presence of structural defects not only allow for the anchoring of nanoparticles, but the localized properties of GO can be tuned with added functionalities, which will be discussed in Chapter 6.

The hybridization of these two discussed supports is an approach to further disperse palladium nanoparticle catalysts, which would allow for the increase of catalyst-support interaction and as well as an increase in catalytic activity.[122-124] The drawback of MOFs is, of course, the low atomic density associated with porous materials. As a result of the low atomic density, there is little catalyst-support interaction between impregnated nanoparticles and cages of the MOF except physical confinement. Additionally, MOFs are generally hydrophobic prior to functionalization with groups such as amines. In Chapter 3, a non-liquid catalytic reaction system was chosen for Ce-MOF due to this reason. RGO and PRGO are excellent supports for palladium nanoparticles, but the graphitic re-stacking of sheets quickly end the usefulness of these supports.

RGO and PRGO do, however, have strong dispersive forces for the increased dispersion of supported nanoparticles and can anchor nanoparticles onto their surfaces to enhance the catalyst-support interaction.[125] RGO and PRGO also have a high thermal stability. The restacking of RGO and PRGO layers can be solved by the intercalative growth of MOF crystals between layers to inhibit restacking by bulk hindrance. The hybridization of MOF and RGO would result in a support with higher dispersion and catalyst-support interaction, where the MOF crystals nucleate and grow from the defect sites of the carbon-based support.[122] In a hybrid MOF-PRGO, the nanoparticle size is expected to be controlled by the size of the generated mesopores of the MOF-PRGO interface. Additionally, because the PRGO is only partially reduced, present oxygen functional groups can provide acidic sites for the support to further improve catalytic reaction activity of the material. Figure 19 illustrates the design strategy for a Ce-MOF-PRGO support hybridized from Ce-MOF and GO, where the functional groups of GO promote MOF growth. GO provides defect sites for nucleation of Ce-MOF crystals. The GO re-stacking is prevented and the hybridized Ce-MOF-PRGO gains higher surface area and thermal stability than Ce-MOF alone.

Additionally, it can be observed that several palladium nanoparticle size regimes can exist. Smaller nanoparticles will embed within the pores of the Ce-MOF. Larger nanoparticles can be anchored to the defect sites of the PRGO. The dispersion is expected to be increased as a result.

The  $\{[\text{Ce}(\text{BTC})(\text{H}_2\text{O})]\text{DMF}\}_n$  Ce-MOF that was studied as a support for palladium nanoparticles for catalytic CO oxidation was chosen for hybridization with GO to form a Ce-MOF-PRGO material. The studied Ce-MOF is a cerium trimesate polymeric structure with cerium centers 6-coordinated to trimesic acid linkers, resulting in an average pore diameter of  $1.3 \times 0.8$  nm,[37] as shown in Figure 4. The  $\text{N}_2$  adsorption-desorption isotherm was previously performed and resulted in a BET surface area of approximately  $62 \text{ m}^2/\text{g}$ , which was consistent with previous

studies on cerium trimesate MOFs.[67] This MOF was chosen for hybridization with GO to create a composite MOF-PRGO in an effort to greatly increase the surface area.

The systematic design of the catalyst is illustrated in Figure 19. As previously mentioned, the design of the catalyst was designed rationally for a specific purpose. The hybridization of GO with Ce-MOF allows for the intercalative growth of MOF crystals between the layers of GO by ionic exchange and covalent bonding with oxygen-bearing functional groups to create a stacked layered material.[126] The sterics of GO restrict the growth of Ce-MOF crystals, which allows for smaller nanocrystals to form rather than micron-sized crystals of 2-6 $\mu\text{m}$  in length. The interaction between the GO and the MOF prevent aggregation of Ce-MOF crystals and the re-stacking of PRGO sheets, which assist in the enhancement of palladium dispersion. In a MOF-PRGO composite system, the reduced palladium can vary in size: smaller nanoparticles are formed within the cavities of the MOF and larger nanoparticles settle the outer surface of the MOF and the defect sites generated during the microwave-assisted reduction of GO into PRGO.

## 4.2 Characterization

The PRGO content for all characterized Ce-MOF-PRGO samples are 12.5 wt%. The XRD diffraction patterns of as-synthesized Ce-MOF, Ce-MOF-PRGO, and 5% Pd/Ce-MOF-PRGO is shown in Figure 20. The characteristic peaks of Ce-MOF are present at 8.4, 10.6, and 18.1° 2 $\theta$ , which is good agreement with a prior synthesis (Figure 5) and previous results.[67] GO typically has a  $d_{001}$  peak at 11.3°, which is indicative of d-spacing.[127] The absence of this characteristic peak indicates the reduction of GO and is an indicator of the formation of a Ce-MOF-PRGO composite. Characteristic peaks for palladium, typically observed at 38.0° 2 $\theta$ , are also unobserved, implying a high degree of dispersion and small nanoparticle size.[128-129] This is expected for low loadings of palladium. It can be seen that the Ce-MOF XRD diffraction pattern did not change



after hybridization nor loading of palladium. Hence, it is argued that the Ce-MOF crystal remains undamaged.

The FTIR spectra of GO, Ce-MOF, and Ce-MOF-PRGO are shown in Figure 21. GO has several distinctive strong bands: C=O stretches at  $1730\text{ cm}^{-1}$ , O-H deformations at  $1370\text{ cm}^{-1}$ , epoxide stretch vibrations at  $1230\text{ cm}^{-1}$ , and C-O stretches at  $1100\text{ cm}^{-1}$  are identifiable.[119, 130] After hybridization, some peaks become delinquent. The epoxy stretch at  $1230\text{ cm}^{-1}$  becomes reduced in intensity. Alcohol deformation peaks are still present due to the presence of O-H groups in terephthalic acid. Most of the remaining present bands overlap with peaks expected from Ce-MOF, including peaks at  $1612\text{ cm}^{-1}$ ,  $1435\text{ cm}^{-1}$ , and  $1373\text{ cm}^{-1}$ . These peaks are associated with  $\text{COO}^-$  asymmetric stretches, which are present in Ce-MOF as well (Figure 6 and Figure 21). A band at  $700\text{ cm}^{-1}$  is attributable to Ce-O stretching. A small C=O shoulder representative for DMF is visible at  $1666\text{ cm}^{-1}$ , indicating that the MOF structure contains DMF molecules, which are suspected to stabilize the MOF structure. This band disappears after microwave irradiation in the presence of palladium nanoparticles, as previously stated. The FTIR spectra after palladium loading into Ce-MOF and Ce-MOF-PRGO is in Appendix A (Figure A2).

The Raman spectra of GO, PRGO, Ce-MOF-PRGO and Ce-MOF are shown in Figure 22. Ce-MOF (Figure 22D) is expected to have several distinct peaks:  $800\text{ cm}^{-1}$ ,  $1000\text{ cm}^{-1}$ ,  $1385\text{ cm}^{-1}$ ,  $1470\text{ cm}^{-1}$ , and  $1600\text{ cm}^{-1}$ , all of which were previously described.[124] All five bands are present in the Raman spectrum of Ce-MOF-PRGO (Figure 22C). The Ce-MOF-PRGO Raman spectrum shows all five peaks in addition to the D and G-band contribution from GO, at  $1350\text{ cm}^{-1}$  and  $1600\text{ cm}^{-1}$  respectively. D bands are due to structural defect bands and G bands are from  $\text{sp}^2$  hybridized vibrational carbons. The graphitic quality and ratio of defects is often taken as a D/G ratio, where graphite and graphene have a ratio near 0. Graphene oxide has a ratio near 1.[131] Pristine

graphene often exhibits a 2D band at  $2800\text{ cm}^{-1}$ . Figure 22A shows GO has a D/G ratio of 0.95 prior to HH reduction in the presence of MWI. After reduction, the D/G ratio drastically decreases to nearly 0.55 (Figure 22B). This is indicative of a decrease in the number of defect sites in RGO relative to the initial unreduced GO.[130, 132] It is difficult to scrutinize the exact D/G ratio in the Ce-MOF-PRGO hybridized composite, but the intensities are relatively similar and nearly 1, which is similar to GO (Figure 22A). The defect sites in the Ce-MOF-PRGO support is preserved for the anchoring of palladium nanoparticles.

The BET surface area was calculated from the nitrogen adsorption-desorption isotherms, as shown in Figure 23.[37] Previous measurements yielded a surface area for the Ce-MOF material of  $62\text{ m}^2/\text{g}$ , which is in agreement with reported results.[67] The surface of the material was increased to  $89\text{ m}^2/\text{g}$  after loading with 5 wt% palladium nanoparticles (Figure 14). As previously discussed, a plausible explanation is the activation of the pores of Ce-MOF by evacuation of DMF molecules during MWI.[65-66] Here, the hybridization of the Ce-MOF with GO to form a Ce-MOF-PRGO composite by intercalative growth of crystals between the layers of GO increased the surface area as well.[133] The incorporation of a carbon-based support to the Ce-MOF resulted in a specific surface area measurement of  $112\text{ m}^2/\text{g}$  for the 5% Pd/Ce-MOF-PRGO. It should be noted that this is an estimated value based off  $\text{N}_2$  adsorption-desorption isotherms. The BET surface area of GO typically cannot be measured via  $\text{N}_2$  adsorption-desorption isotherms because  $\text{N}_2$  gas molecules cannot permeate the layers of GO, especially if the GO is reduced into RGO.[134] Two accepted methods of the measurement of the surface area of GO include methylene blue titration,[134] a method to determine saturation point of methylene blue on the surface of GO, or freeze-dry treatment of the GO. In freeze-dry treatments, GO is dispersed in water and frozen with liquid nitrogen. The water is slowly evaporated under vacuum, leaving the

GO layers exfoliated and accessible to N<sub>2</sub> probe molecules. The inclusion of GO to the Ce-MOF support resulted in a material with a relatively higher surface area.

The XPS spectra of C 1s (Figure 24), Ce 3d (Figure 25), and Pd 3d (Figure 26) were analyzed to characterize the composition of the surfaces of each of the catalysts. The C 1s spectra for Ce-MOF, 5% Pd/Ce-MOF, and 5% Pd/Ce-MOF-PRGO are shown in Figure 24A-C, and it can be observed that several peaks are present for oxygen interactions. Peaks at 285.6, 286.7, 287.7, and 289.0 eV are assignable to the C 1s of C-OH, C-O, C=O, and HO-C=O groups, respectively.[42, 135] These peaks are observed in similar intensities for all samples, which is to be expected. The spectrum for 5% Pd/Ce-MOF-PRGO (Figure 24C) shows the peaks associated with C-OH, C-O, C=O, and HO-C=O are still present after reduction of palladium, indicating partial reduction of GO during MWI treatment with HH reducing agent.[121, 130, 135-136] The C 1s spectrum of RGO is very different, whereby most the peaks correlated to interaction with oxygen are diminished or completely missing.

The Ce 3d XPS spectra (Figure 25) were collected because the oxidation state of the cerium nodes for Ce-MOF and Ce-MOF-PROG is expected to be Ce<sup>3+</sup>; the lack of Ce<sup>3+</sup> or the presence of a satellite peak at 917 eV are indicators of the formation of CeO<sub>2</sub>, which would indicate that the *in situ* formation of Ce-MOF-PRGO was unsuccessful. The Ce 3d peak for Ce<sup>4+</sup> are observable in Figure 11, where three doublets are confirmed at 882 (v), 885 (v'), and 888 eV (v'') and for 3d<sub>3/2</sub>, at 900 (u), 904 (u'), and 906 (u'').[69, 72] The u/v'' and u/v''' spinning-orbit pairs are characteristic of Ce<sup>4+</sup> 3d states. The 885 eV and 904 eV doublet for Ce<sup>3+</sup> are present in similar intensity across Ce-MOF, 5% Pd/Ce-MOF, and 5% Pd/Ce-MOF-PRGO, which indicates that the Ce-MOF successfully formed in the presence of GO.

The Pd 3d XPS spectra were also collected to determine the oxidation state of the catalyst palladium nanoparticles. Pd(0) is typically more catalytically active than Pd(II).[121] The relative peaks of the 335.8 eV and 340.1 eV doublet for Pd(0) can be compared to the peaks of 336.9 eV and 341.0 eV doublet of Pd(II).[119, 135] The 5% Pd/Ce-MOF (Figure 26A) and 5% Pd/Ce-MOF-PRGO (Figure 26B) have a Pd(0)/Pd(II) ratio of 1.37 and 1.54, respectively.

Morphologies of the cerium MOFs were observed for Ce-MOF and Ce-MOF-PRGO. TEM (Figure 27 and Figure 28) and SEM (Figure 29) micrographs were taken to observe the morphologies of the Ce-MOF and Ce-MOF-PRGO supports before and after loading of palladium, as well as to observe the interaction between Ce-MOF and PRGO. As previously discussed, the crystals of Ce-MOF were needle-like in structure, with a length of 2-6 $\mu$ m in range. This is illustrated in Figure 27A. Figure 27B shows the loading of palladium on the Ce-MOF support by MWI using HH as a reducing agent. The micrograph shows the relatively homogeneous distribution of palladium nanoparticle size. The measured palladium nanoparticle size for Ce-MOF was  $3.9 \pm 1.3$  nm, as shown in Figure 30. Larger nanoparticles are on the surface of the Ce-MOF. Very small (1-2 nm) palladium nanoparticles are expected to be physically confined within the pores of the Ce-MOF and thus are not accurately accounted for in the particle size distribution due to the resolution of the TEM images.

TEM images of the Ce-MOF-PRGO are visible in Figure 27C. Not only do the Ce-MOF appear to be intertwined in the sheets of the PRGO, but there is a differential in the length of the Ce-MOF needle-like crystals. When the GO is added during to the Ce-MOF precursors during synthesis, the resultant crystals appear to decrease in size and in length, down to <1 $\mu$ m, which confirms interaction between Ce-MOF and the PRGO. Ionic exchange or covalent bonding with oxygen groups present on GO during intercalative growth of Ce-MOF crystal is suspected. The

growth of the Ce-MOF crystals is restricted in the presence of GO sheets and is why the needle-shaped crystals decreased drastically in length. The concentration of GO is expected to be an important variable in the size of the Ce-MOF crystals in a hybridized system.

The distribution of palladium nanoparticles is viewable in Figure 28. It can be seen that the palladium nanoparticles are well dispersed on the surface of RGO in Figure 28A. The dispersion is homogeneous, but several aggregated particles are clearly visible. For a RGO system, the palladium nanoparticle size was calculated to be  $6.8 \pm 2.8$  nm. Figure 27C shows the Ce-MOF-PRGO composite; Figure 28B-F shows the dispersion of palladium nanoparticles through the Ce-MOF-PRGO composite. Agglomeration of palladium nanoparticles in the hybridized support is still visible, but the average particle size of  $4.8 \pm 1.3$  nm is much less than the palladium nanoparticles supported on RGO. It can be argued that the two nanoparticle size regimes induced by hybridization of the supports, where small nanoparticles are confined within the Ce-MOF pores and large particles are dispersed on the RGO, is further assisted by the generation of mesopores at the Ce-MOF-PRGO interface. The size distribution of palladium nanoparticles is shown in Figure 30.

The SEM images of 5 wt% Pd on the Ce-MOF-PRGO supports are shown in Figure 29. The needle-shaped Ce-MOF are clearly visible in Figure 29B. The dispersion of the surface-settled palladium nanoparticles is excellent. Figure 29C and Figure 29D show the interfacial interaction between the Ce-MOF and PRGO and confirm the hybridized nature of the material. The boundary between PRGO and Ce-MOF is visible; thin sheets of PRGO are wrapped around the Ce-MOF and an integrated scaffold is available for palladium nanoparticle dispersion. The PRGO sheets easily wrap around the Ce-MOF and can protect the Ce-MOF crystals by contributing to the overall stability and durability of the composite material. In addition to the larger palladium nanoparticles

on the RGO, nanoparticles can be seen present at the Ce-MOF-PRGO boundary interface (Figure 29D).

### 4.3 Acidity Measurement and Active Site Determination

The acid strength and total number of acid sites was measured by potentiometric nonaqueous titration with n-butylamine because it is suspected that acidity plays a part in this reaction, which will be investigated in Chapter 5. The initial electrode potential ( $E_i$ ) shows the acid strength, and the total number of acid sites (acidity) can be calculated from the value of the mequiv n-butylamine/g solid.[137] The  $E_i$  ranges from  $<0$  mV (weak acid sites) to  $>100$  mV (very strong acid sites).[138] The acid strength of acid sites were determined from the initial electrode potential. The saturation point determined by titration indicated the total number of acid sites.[41] The potentiometric titrations of 5% Pd supported on Ce-MOF, Ce-MOF-PRGO, and RGO are pictured in Figure 31.

The 5 wt% Pd/Ce-MOF catalyst was determined to have an acid strength,  $E_i$ , of 43 mV through potentiometric titration due to the presence of  $-\text{COOH}$  groups on linker trimesic acid coupled to cerium nodes. The 5 wt%Pd/PRGO sample was determined to be weakly acidic at 50 mV, which is expected due to the presence of  $-\text{COOH}$  groups as well. Such groups are typically not as easily removed as alcohol and epoxy groups during the simultaneous reduction of palladium and GO. The measured initial potential,  $E_i$ , for 5 wt% Pd/Ce-MOF-PRGO was approximately 148 mV, which is correlated to a higher acid strength. The acid strength of the composite material is higher because of the inclusion of acid sites from both Ce-MOF and PRGO as well as the higher dispersion of palladium. More palladium sites are accessible. The higher relative acidity of this material is expected to play a crucial role in the catalytic hydrogenation of vanillin.

The results of the n-butylamine titration are summarized in Table 3. The quantity of acid sites is significantly higher for the palladium-laden composite material than either of the constituent 5% Pd/Ce-MOF or 5% Pd/RGO catalysts. The acid sites were derived from the titration endpoint for saturation of materials with n-butylamine. It is apparent that the 5% Pd/Ce-MOF-PRGO sample had the most acid sites (0.72 mequiv/g) due to the intercalation of Ce-MOF between GO layers and the smaller Ce-MOF crystals providing a higher surface area, in addition to the partial reduction of GO sheets. The presence of acidic sites within the 5% Pd/Ce-MOF-PRGO sample correlates to the high TOF number calculated for the formation of 2-methoxy-4-methylphenol by 30 min, which also suggests that acidity is important in the selectivity for the final hydrogenation product. 5% Pd/RGO exhibited no selectivity for 2-methoxy-4-methylphenol. The lack of hydrogenolysis for this particular catalyst indicates an insufficient accessibility of vanillyl alcohol intermediates to the palladium sites.

The Lewis and Brønsted acid sites present in the materials were determined to approximate contributions of acidity to the enhanced catalytic activity of the 5% Pd/Ce-MOF-PRGO catalyst. Pyridine was adsorbed onto the catalysts, and the FTIR spectrum of each sample was taken before and after pyridine adsorption. The FTIR spectra of each sample is given in Figure 32. The spectrum for each sample shows an appearance of bands after pyridine adsorption, which are attributable to pyridinium ions on Brønsted acid sites and coordination of pyridine molecules with Lewis acid sites. The GO sample has new peaks at 1442 and 1622  $\text{cm}^{-1}$  for Lewis acid sites. Ce-MOF shares the two new Lewis peaks at 1442 and 1622  $\text{cm}^{-1}$ , but also has weak peaks at 1491 and 1583  $\text{cm}^{-1}$ , which can be assignable to either Lewis or Brønsted acid sites. The hybridized Ce-MOF-PRGO sample lacks a peak at 1545  $\text{cm}^{-1}$  so no strong Brønsted acid sites are present. It is suspected that the only sites present in the Ce-MOF-PRGO is Lewis acid sites. Quantification of

the exact number of total acid sites were not possible due to the overlap of FTIR peaks. The number of active sites, however, could be measured via H<sub>2</sub> pulse titration.

H<sub>2</sub> pulse titration was performed to determine several parameters of the catalysts: the surface dispersion (accessible surface palladium), average particle size, active sites, and metallic surface area (Table 4). These parameters will be correlated to the activity of the materials. The H<sub>2</sub> pulse titration showed that the degree of palladium dispersion was significantly higher on the hybridized Ce-MOF-PRGO support (13.9%) than either Ce-MOF (9.8%) or RGO (5.4%). It can be seen that the composite material had a higher Pd active site and metallic surface area overall, which is the expected advantage of hybridizing a MOF and GO. The lower metal dispersion on the RGO is expected due to the aggregation of palladium nanoparticles as shown in TEM (Figure 27). TOF values were also calculated.

#### **4.4 Effect of Ce-MOF-PRGO Hybridization on Vanillin Hydrogenation Selectivity**

The accepted hydrogenation pathway of vanillin is demonstrated in Figure 33, whereby two mechanisms exist. The most common pathway is a two-step hydrogenation-hydrogenolysis pathway where vanillin is converted into vanillyl alcohol as an intermediate, which is then hydrogenolyzed into 2-methoxy-4-methylphenol. The second accepted pathway is a one-step direct hydrogenolysis, which occurs at high temperatures and high H<sub>2</sub> pressure.[128, 139] Typically, the first mechanism is more easily achievable due to the lower energy requirement.

The catalytic hydrogenation of vanillin was investigated with four supports: Ce-MOF, RGO, Ce-MOF-PRGO hybrid, and a physical mixture of Ce-MOF and RGO. The physical mixture serves as a blank test to demonstrate any synergistic effects promoted by the *in situ* growth of Ce-MOF precursors on GO. The physical mixture was synthesized by the physical mixing of



pre-formed Ce-MOF and GO via mortar and pestle. 5 wt% Pd was incorporated into each sample and each catalyst was tested for the catalytic hydrogenation of vanillin.

The mol% composition of each sample as a function of time is depicted in Figure 34. It can be seen that 5% Pd/Ce-MOF (Figure 34A) had relatively low conversion; the mol% composition of vanillin remained high until about an hour. The selectivity towards 2-methoxy-4-methylphenol was also low. This is expected to be due to the low dispersion of a non-functionalized MOF in aqueous solution. 5% Pd/RGO (Figure 34B) also had low conversion, where only 60% conversion of vanillin into products was achieved after an hour; the selectivity towards 2-methoxy-4-methylphenol was nonexistent, which is expected in part due to the large palladium nanoparticles, which were shown to be aggregated in TEM images. A physical mixture of Ce-MOF and RGO (Figure 34C) had similar conversion of vanillin as 5% Pd/Ce-MOF and a similar low selectivity of 5% Pd/RGO, which is expected due to the low 12.5 wt% RGO contribution towards the mixture. However, it can be seen that, when hybridized, the total activity is greater than the sum of its constituent parts: Figure 34D shows that 5% Pd/Ce-MOF-PRGO has full conversion of vanillin into products within 60 min, similar to Ce-MOF, but the higher dispersion induced by the oxygen-groups of the PRGO allows for a greater selectivity of 60% 2-methoxy-4-methylphenol within the first 60 min. This is much higher than the other samples.

Ce-MOF is a better support for palladium nanoparticles than RGO in this reaction due to the low conversion and especially selectivity of RGO. Ce-MOF has a smaller and narrower nanoparticle distribution than RGO. In addition to the differential between the palladium nanoparticle size, it appears that the two-step reaction is more operative on Ce-MOF, and that the second step of the reaction, hydrogenolysis, does not occur on the RGO support very easily. Similar to the usage of Ce-MOF as a CO oxidation catalyst, it is expected that a promoting effect

due to the  $\text{Ce}^{3+}$  is involved in the reaction.  $\text{Ce}^{3+}$  nodes are expected to act as Lewis acid sites and can adsorb or activate vanillin to increase the selectivity towards the fully-hydrogenated product.

The physical mixture of Ce-MOF and RGO shows an additive effect of the individual constituents, rather than a promotive effect. After 120 min, 95% conversion is achieved, yet the desirable 2-methoxy-4-methylphenol mol% remained a trifling 5%. These results are very different from a hybridized Ce-MOF-PRGO support, where the rapid decrease in vanillin composition is observed with an increase in vanillyl alcohol composition that then decreases rapidly to give rise to the final product. The reactions shows a mol% composition of 100% 2-methoxy-4-methylphenol after 240 m.

The results achieved by the 5% Pd on Ce-MOF, Ce-MOF-PRGO, and RGO catalysts was consistent with the measured active sites and acidity measurements (Table 3 and Table 4). The results seen in Figure 34 indicate that hybridization of Ce-MOF and PRGO enhances the conversion of vanillin into products effectively due to the presence of acid sites (Table 3) and also due to greater dispersion of palladium (Table 4). The Ce-MOF-PRGO support has the highest acid sites, acid strength, metal dispersion, and palladium active sites. The simultaneous reduction of palladium ions and the Ce-MOF-PRGO composite resulted in only partial reduction of GO sheets, which lead to a higher acid strength. Additionally, the intercalation of Ce-MOF between layers of GO prevented the re-stacking of sheets, and enabled higher palladium dispersion. The RGO had the least metal dispersion due to inaccessibility of palladium sites as a result of re-stacking.

It is known that the acid sites available on a catalyst can enhance a reaction: the hydrogenation of methylcyclopentane into cyclohexane has a faster rate when the number of Brønsted sites present on zeolitic supports increases.[140] For vanillin, it was previously studied that sulfonic acid-functionalized MIL-101 MOFs resulted in faster hydrogenolysis of vanillyl

alcohol due to presence of additional acid sites.[141] Whereas it is known that acidity assists in certain hydrogenation reactions, it is unknown if there is any mechanistic changes in addition to the activation of reactants by acid sites. The effect of acidity is further studied in Chapter 5.

#### **4.5 Effect of RGO% in Ce-MOF-PRGO Supports for Vanillin Hydrogenation**

The PRGO ratio to Ce-MOF was investigated to determine the optimal wt% RGO, which was ultimately determined to be 12.5%. The effect of wt% RGO on the catalytic hydrogenation is shown in Figure 35. It can be seen that, for all samples with a low RGO content, full conversion is achieved within 120 min. The selectivity towards 2-methoxy-4-methylphenol differs as a function of RGO wt% for samples under 20% RGO composition. This is attributed to the presence of small nanoparticles within the cavities of Ce-MOF, high wt% Ce-MOF composition towards the support, and as the presence of Lewis acid sites contributed by PRGO. As can be seen from Figure 35, the conversion drops due to the lack of accessibility to palladium nanoparticles. As the PRGO content increases to 50%, 90% conversion is achieved. Pure PRGO resulted in less than 40% conversion, as seen in Figure 34. It is concluded that the stacking of PRGO sheets reduced accessibility to smaller nanoparticles, and the vanillin reactant could react with only the larger nanoparticles.

#### **4.6 Effect of Palladium Content, Temperature, and Pressure on the Conversion and Selectivity of Ce-MOF-PRGO Supports**

Palladium is a very expensive metal. Efficient utilization of lower quantities is preferable. Additionally, the hydrogenation of vanillin is a model for biofuel upgrade; it is detrimental to consume a lot of energy to produce a small amount of value-added chemicals.[142] Hence, the ideal temperature (energy) and pressure requirement should be low. The palladium content, temperature, and pressure of the system were evaluated for optimization.

The palladium content on Ce-MOF-PRGO (Figure 36) was varied from 1-10 wt% and the activity of the catalyst was measured. It is noted the full conversion of vanillin into products was achieved regardless of the amount of palladium, after 2 h. However, the selectivity varies. The selectivity towards 2-methoxy-4-methylphenol was maximized at 5% with 100 °C and 1 MPa reaction conditions. This is an indication that the conversion of vanillin into vanillyl alcohol occurred easily but the conversion of the intermediate into the 2-methoxy-4-methylphenol final product was more difficult. The aggregation of palladium nanoparticles at higher loading prevented the reaction from proceeding.

An increase in the temperature led to higher selectivity of 2-methoxy-4-methylphenol, as shown in Figure 37. At 150 °C, 100% conversion and 100% selectivity was achieved but 150 °C is incredibly high for this reaction and is inefficient for the generation of biofuel. An increase in the pressure led to slightly higher selectivity towards the fully hydrogenated product. It is ultimately concluded that the 5% Pd/Ce-MOF-PRGO catalyst is highly effective for the hydrogenation of vanillin into 2-methoxy-4-methylphenol as a biofuel upgrade model reaction.

#### **4.7 Recyclability of 5% Pd/Ce-MOF Catalysts**

The recyclability of the 5% Pd/Ce-MOF-PRGO catalyst was performed to determine the lifespan of the catalyst. The conversion of the vanillin to products by the 2 h interval remains unchanged over 4 recycles, as shown in Figure 39 under previous conditions. However, the selectivity towards the 2-methoxy-4-methylphenol was hampered with every run, decreasing steadily from 70% selectivity to 50% selectivity. This is attributed to the accumulation of residual products and unreacted vanillin on the surface of the catalyst. This is concluded because the XRD (Figure 40) of the MOF-PRGO hybrid before and after the reaction retain the same crystallinity and similar relative intensities of peaks.

#### 4.8 Proposed Mechanism and Literature Comparison

A reaction mechanism is proposed to illustrate the function of the hybridized Ce-MOF-PRGO support in the reaction. Prior to hydrogenation of vanillin,  $H_2$  is adsorbed and activated by palladium nanoparticles embedded within the Ce-MOF-PRGO. The vanillin has an aldehyde group that is hydrogenated into an alcohol, resulting in the formation of the vanillyl alcohol intermediate. This step appears to take place with either the Ce-MOF or the RGO catalysts, so it is concluded that this step is common to both supports. It is more efficient on the 5% Pd/Ce-MOF catalyst, however, because of the small nanoparticle size due to the confinement within the pores. In the second step, vanillyl alcohol intermediate is converted into 2-methoxy-4-methylphenol by hydrogenolysis. This does not occur for 5% Pd/RGO because of the lack of acid sites and because of the lack of accessibility to palladium active sites after restacking of layers. The composite 5% Pd/Ce-MOF-PRGO sample has both the acidic sites and the accessible palladium sites. The higher dispersion and accessibility promotes the conversion of vanillyl alcohol into the final product for the hybridized Ce-MOF/PRGO catalyst.

The catalytic conversion and selectivity of this catalyst is compared to other catalysts in Table 5. 100% conversion and 100% selectivity was achieved for the 5% Pd/Ce-MOF-PRGO catalyst after 240 m reaction time. It was found that 85% conversion and 47% selectivity could be achieved with palladium nanoparticles supported on a single wall CNT hybridized with inorganic oxides (SWNT-SiO<sub>2</sub>).[143] The results achieved by the 5% Pd/Ce-MOF-PRGO performs better than that of 2% Pd/MIL-101 (Cr).[141] The activity of 2% Pd/SO<sub>3</sub>H-MIL-101 (Cr) was attributed to the presence of Brønsted acidic sites present through the functionalized MOF. The 5% Pd/Ce-MOF-PRGO catalyst contains a high number of acid sites, as previously discussed.

However, it was determined that these sites are Lewis sites rather than the highly active Brønsted acidic sites through pyridine adsorption.

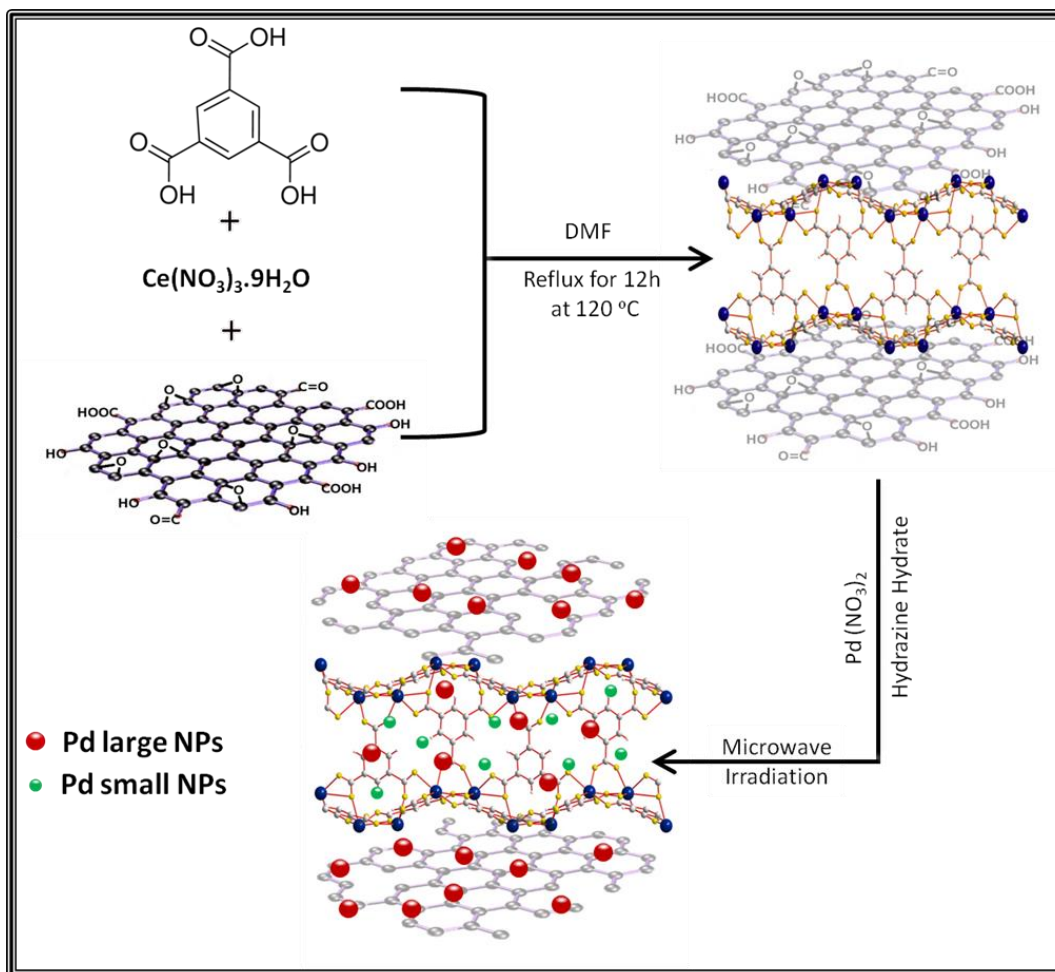


**Figure 19.** Design strategy of a Ce-MOF-PRGO hybrid.

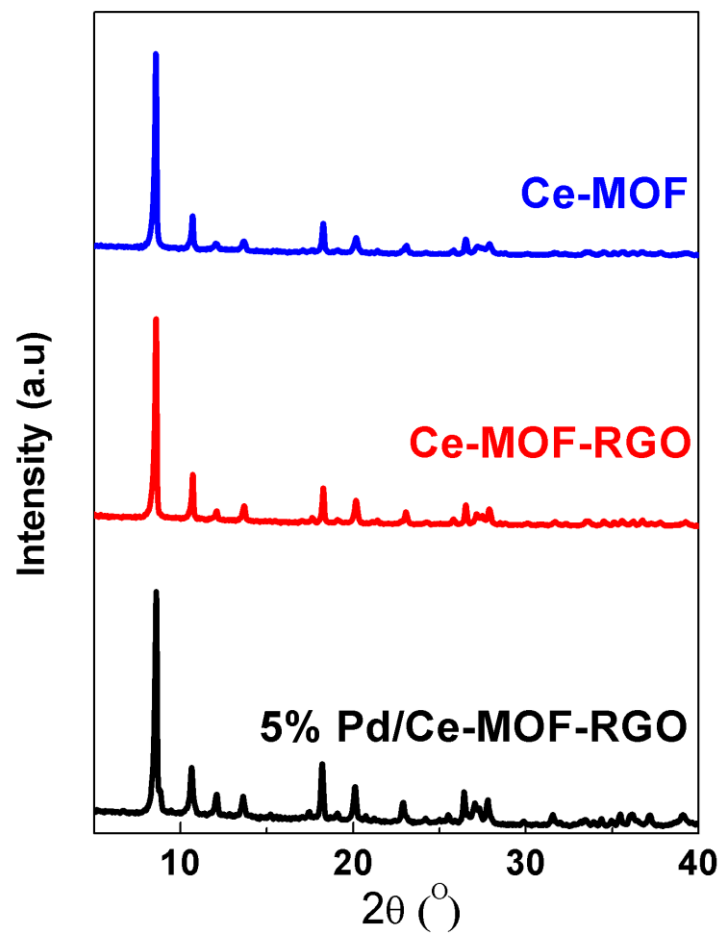


**Figure 20.** XRD Diffraction patterns of Ce-MOF, Ce-MOF-RGO, and 5% Pd/Ce-MOF-RGO.



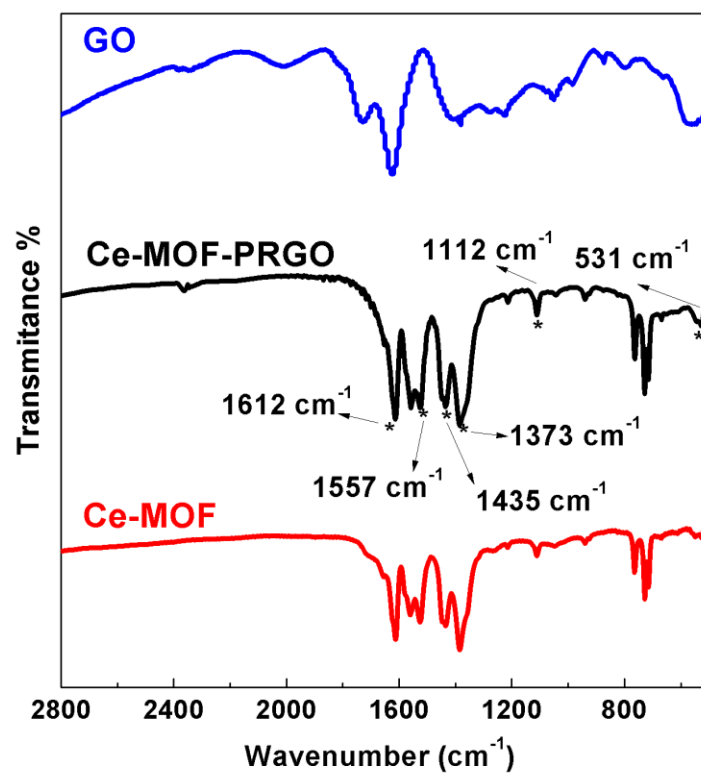


**Figure 21.** FTIR spectra of GO, Ce-MOF-PRGO, and Ce-MOF.

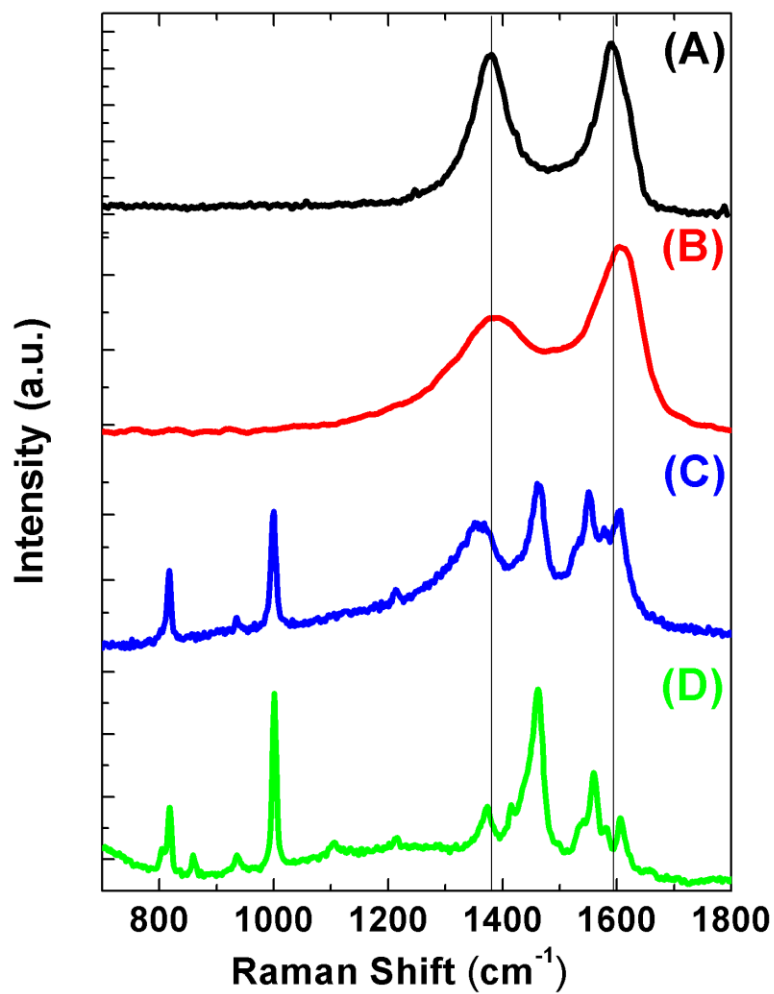


**Figure 22.** Raman spectra of GO (A), RGO (B), Ce-MOF-PRGO (C), and Ce-MOF (D).

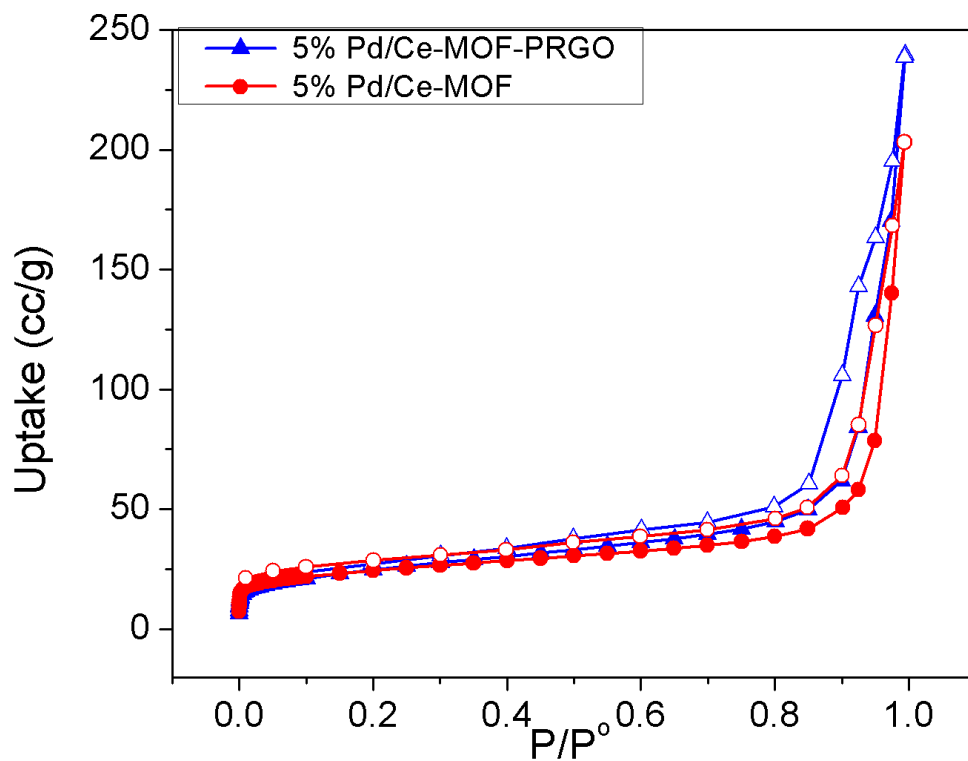


**Figure 23.** N<sub>2</sub> gas adsorption and desorption isotherms of 5% Pd/Ce-MOF and 5% Pd/Ce-MOF-PRGO.

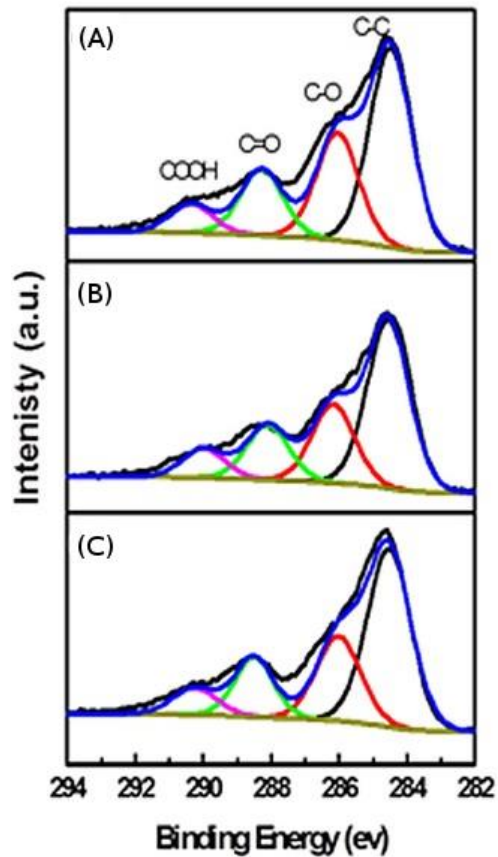


**Figure 24.** XPS C 1s spectra of Ce-MOF (A) and 5% Pd/Ce-MOF (B), and 5% Pd/Ce-MOF-PRGO (C).

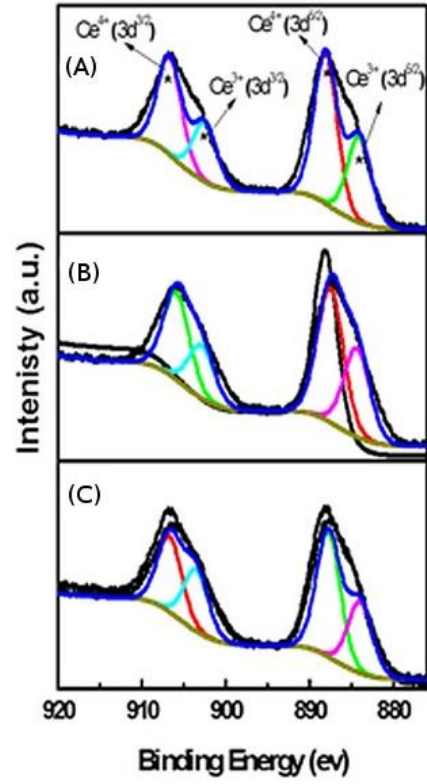


**Figure 25.** XPS Ce 3d spectra of Ce-MOF (A) and 5% Pd/Ce-MOF (B), and 5% Pd/Ce-MOF-PRGO (C).

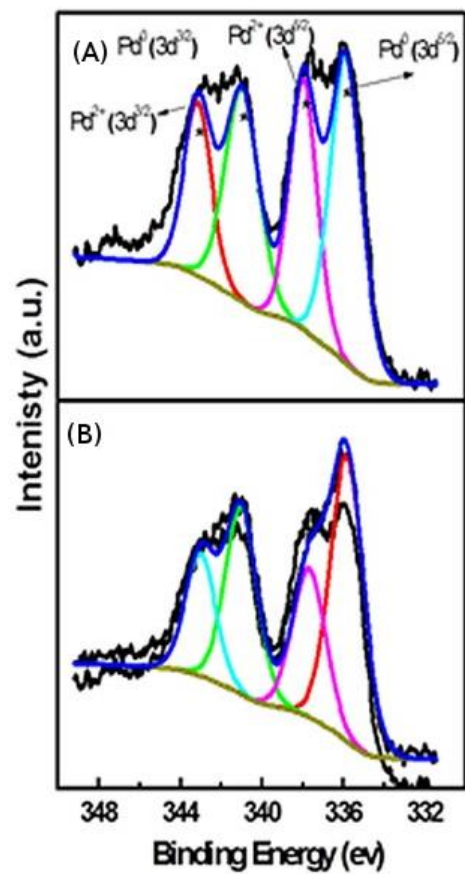


**Figure 26.** XPS Pd 3d spectra of 5% Pd/Ce-MOF (A), and 5% Pd/Ce-MOF-PRGO (B).

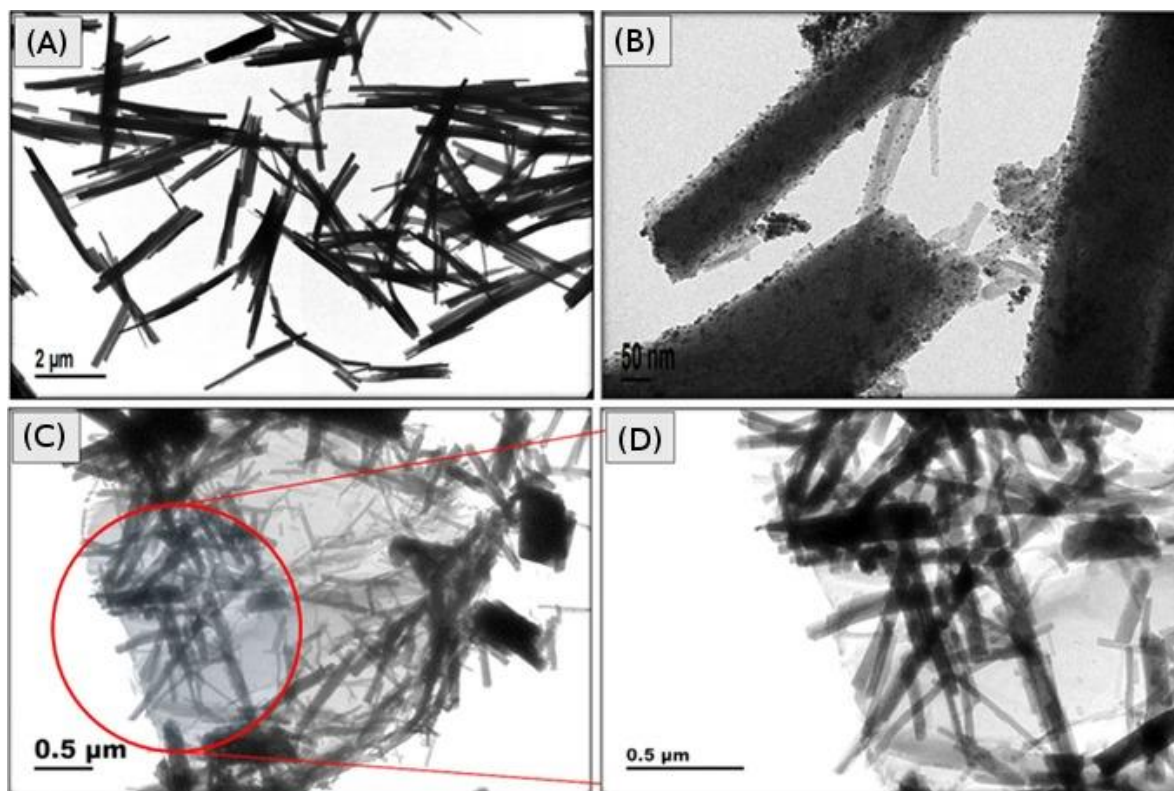


**Figure 27.** TEM of Ce-MOF (A), 5% Pd/Ce-MOF (B), and Ce-MOF-PRGO (C, D).

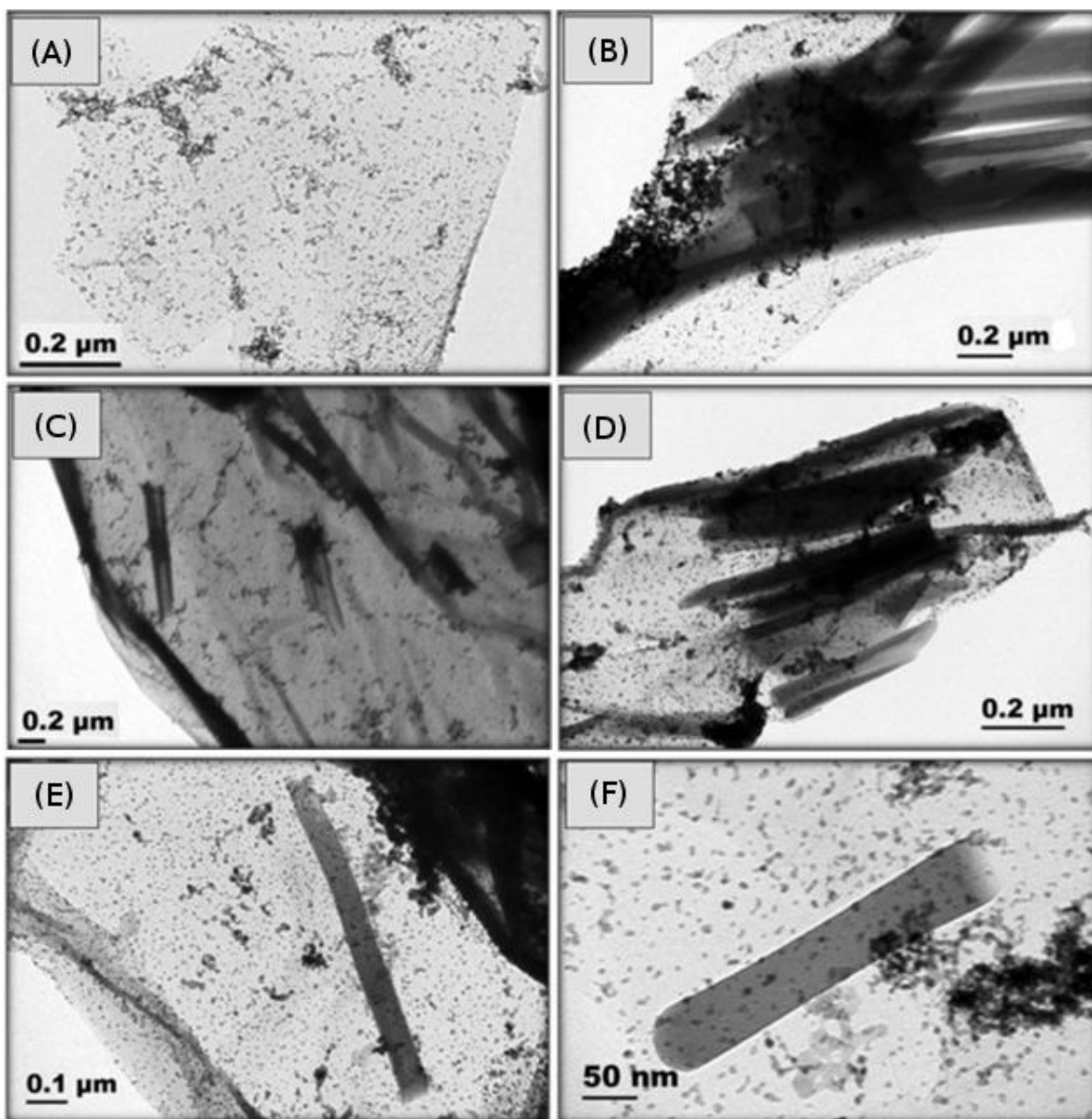


**Figure 28.** TEM of 5% Pd/PRGO (A), and 5% Pd/Ce-MOF-PRGO (B-F).



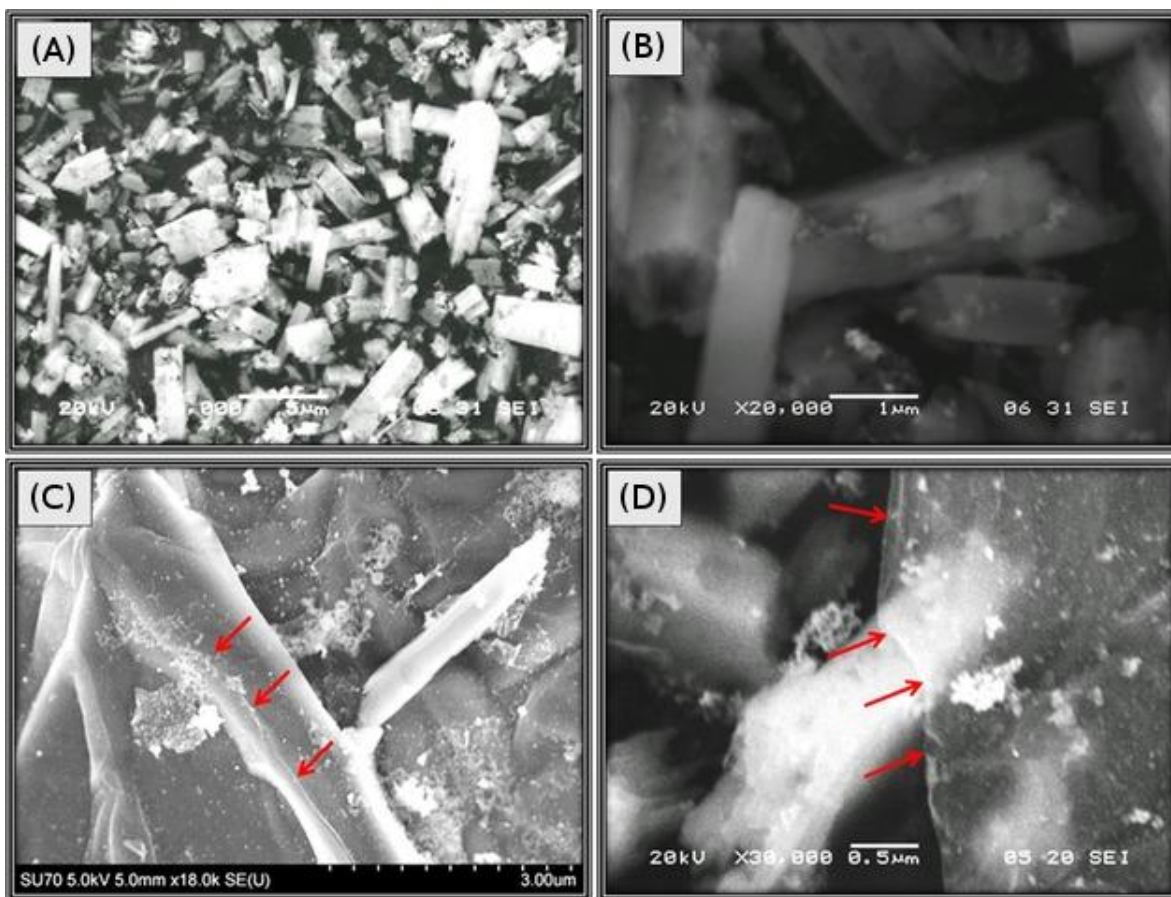


**Figure 29.** SEM of 5% Pd/Ce-MOF (A,B) and 5% Pd/Ce-MOF-PRGO.

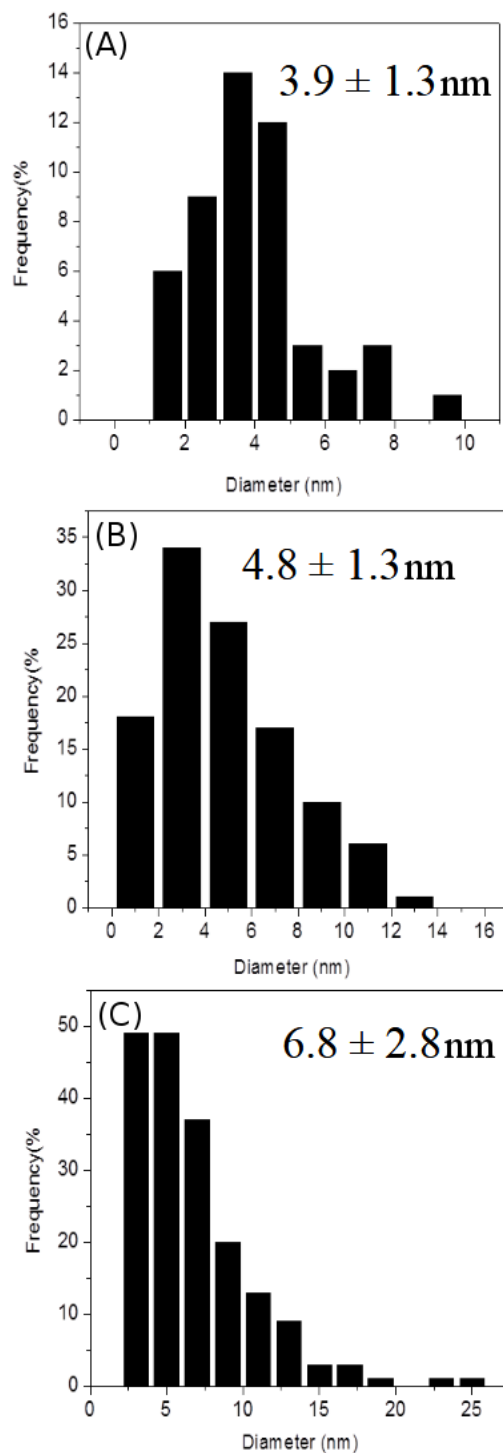


**Figure 30.** Palladium nanoparticle size distribution of 5% Pd supported on Ce-MOF (A), Ce-MOF-PRGO (B), and RGO (C).

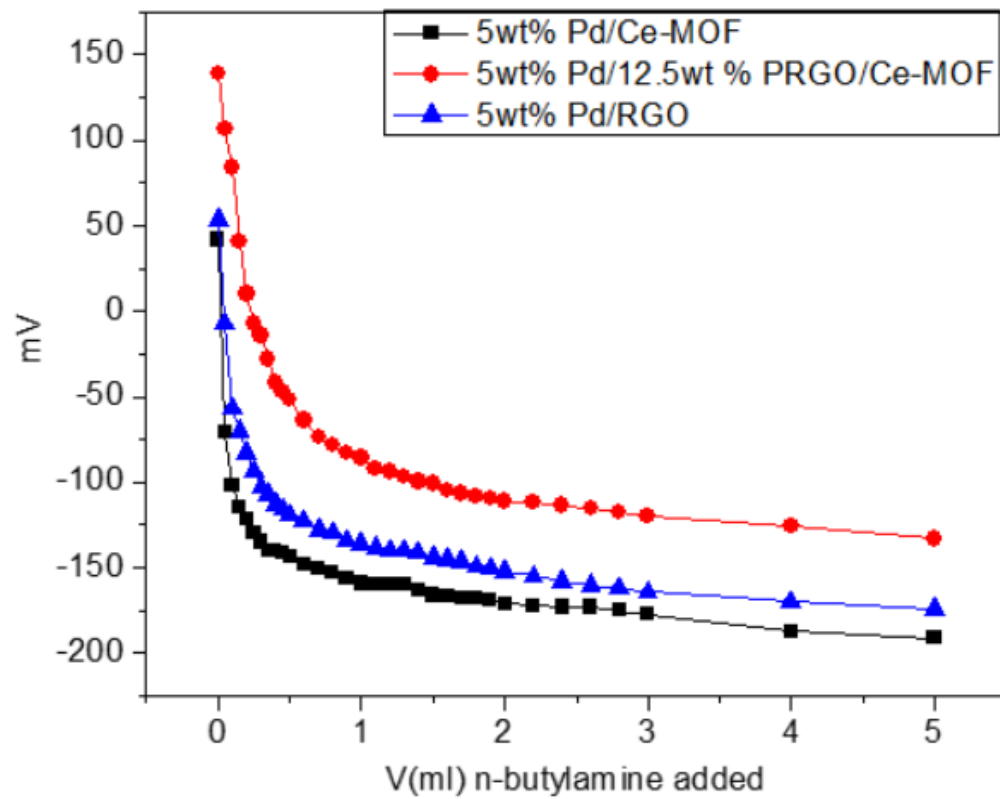


**Figure 31.** Potentiometric titration curves of 5% Pd supported on Ce-MOF, Ce-MOF-PRGO, and RGO.

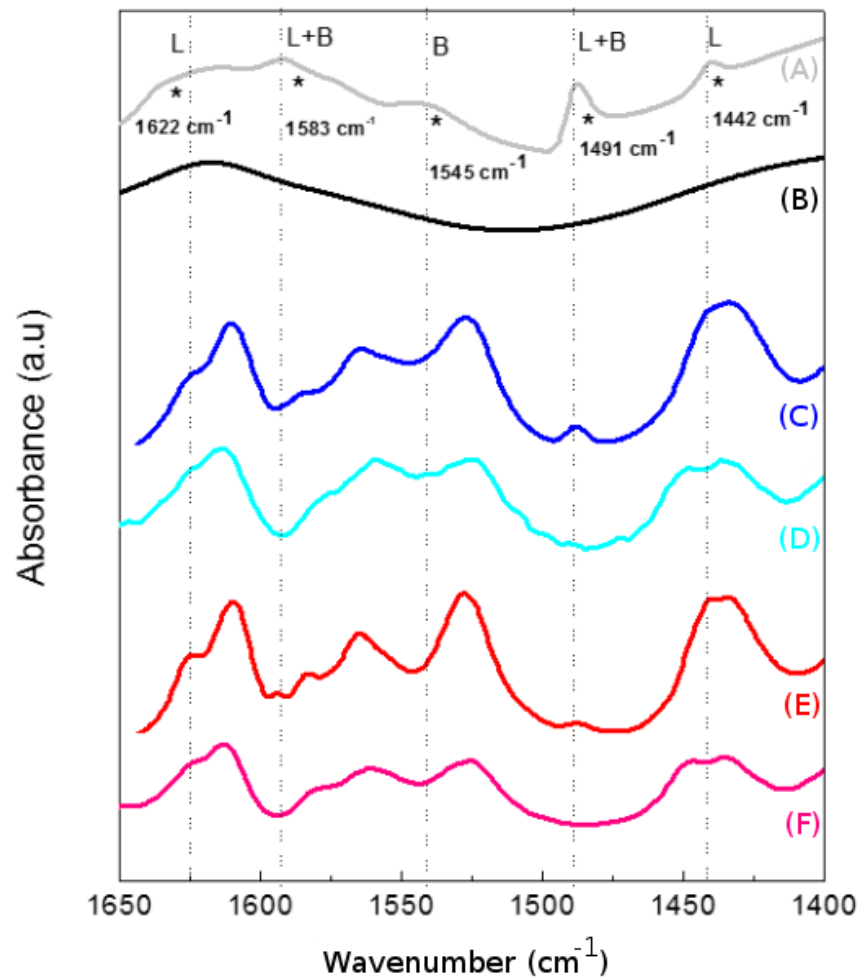


**Figure 32.** FTIR spectra of GO + pyridine (A), GO (B), Ce-MOF-PRGO + pyridine (C), Ce-MOF-PRGO (D), Ce-MOF + pyridine (E), and Ce-MOF (F). Peaks for Lewis or Brønsted acid sites are labelled as L and B, respectively.

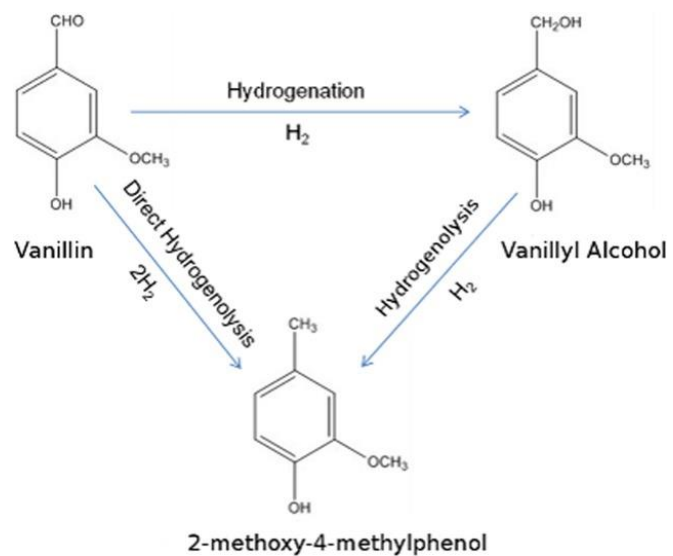


**Figure 33.** Hydrogenation of vanillin to 2-methoxy-4-methylphenol.

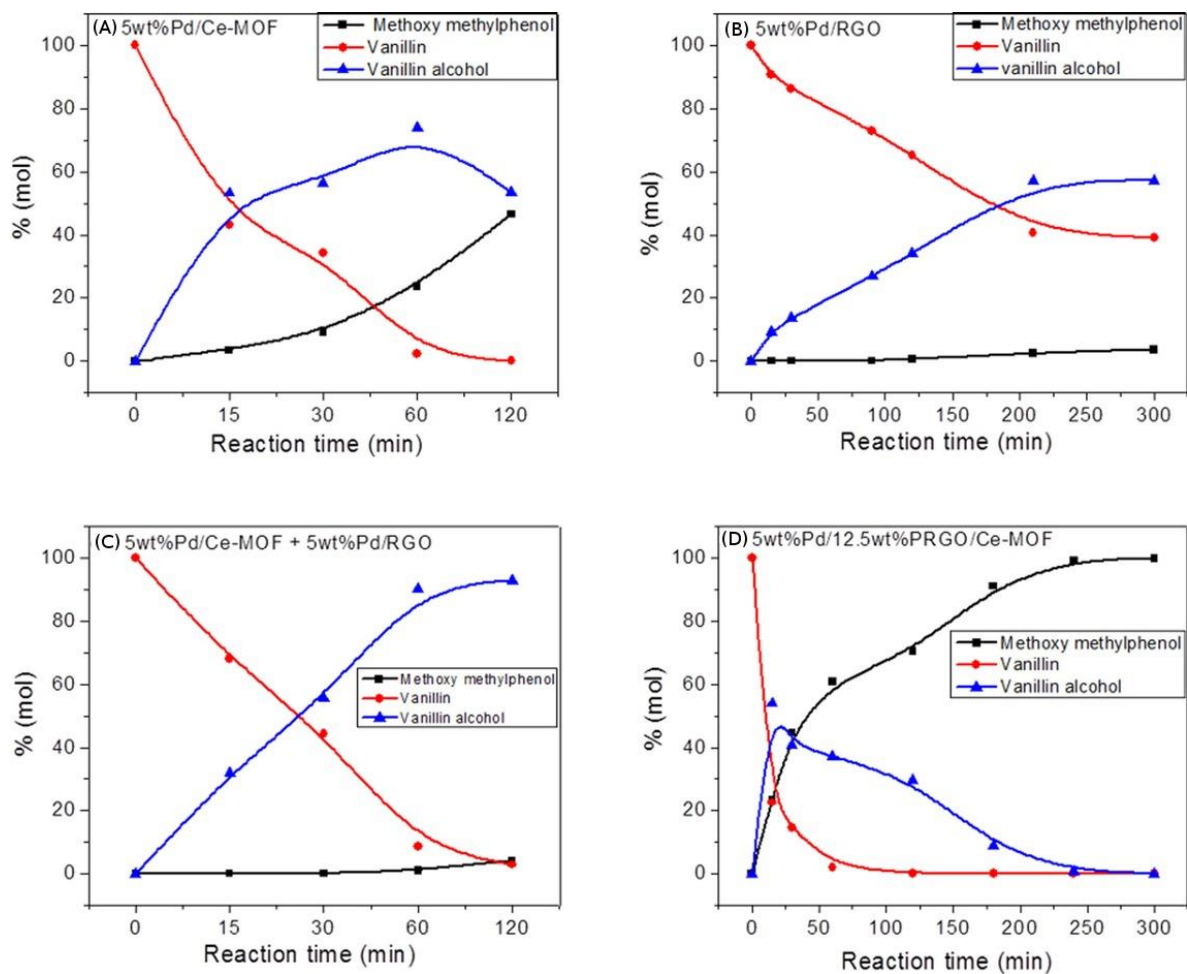


**Figure 34.** Mol% composition of vanillin, vanillyl alcohol, and 2-methoxy-4-methylphenol as a function of time for 5% Pd on Ce-MOF (A), RGO (B), a physical mixture of Ce-MOF and RGO (C), and Ce-MOF-PRGO hybrid. Reaction conditions: 0.3g vanillin, 40 mL water, 50 mg catalyst,  $T = 373\text{K}$ ,  $\text{H}_2$  Pressure = 1 MPA, and stir speed = 900 rpm.

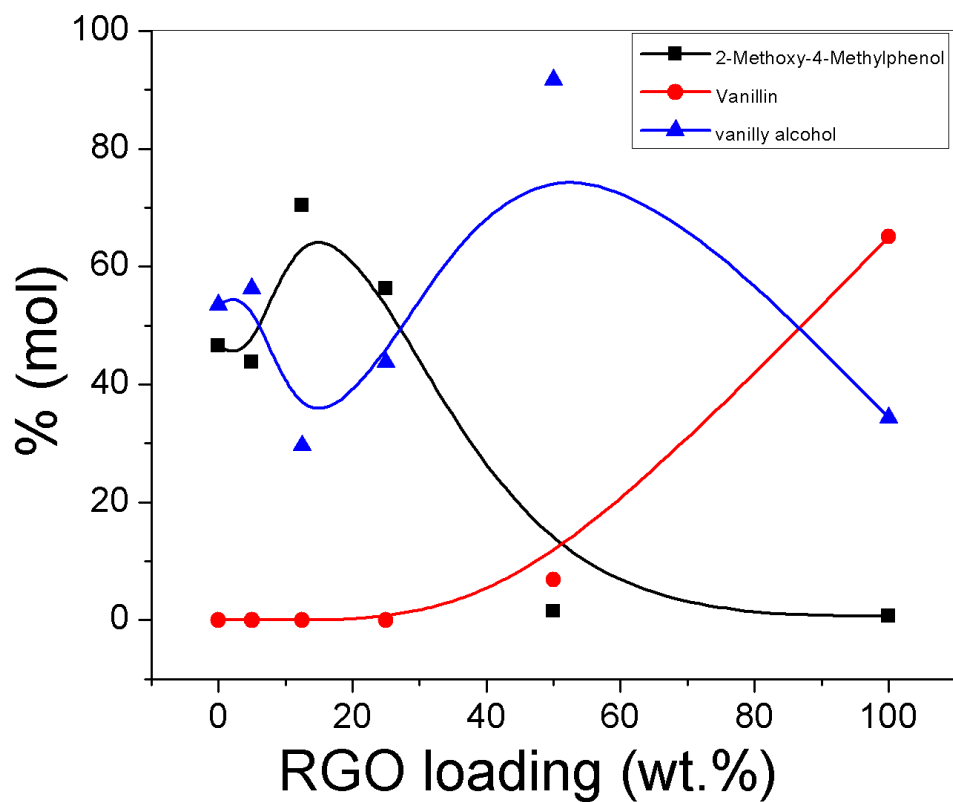


**Figure 35.** Mol% of vanillin, vanillyl alcohol, and 2-methoxy-4-methylphenol as a function of PRGO wt% in the Ce-MOF-PRGO support with 5 wt% Pd. Reaction conditions: 0.3g vanillin, 40 mL water, 50 mg catalyst, T = 373K, H<sub>2</sub> Pressure = 1 MPA, and stir speed = 900 rpm, t = 120 min.

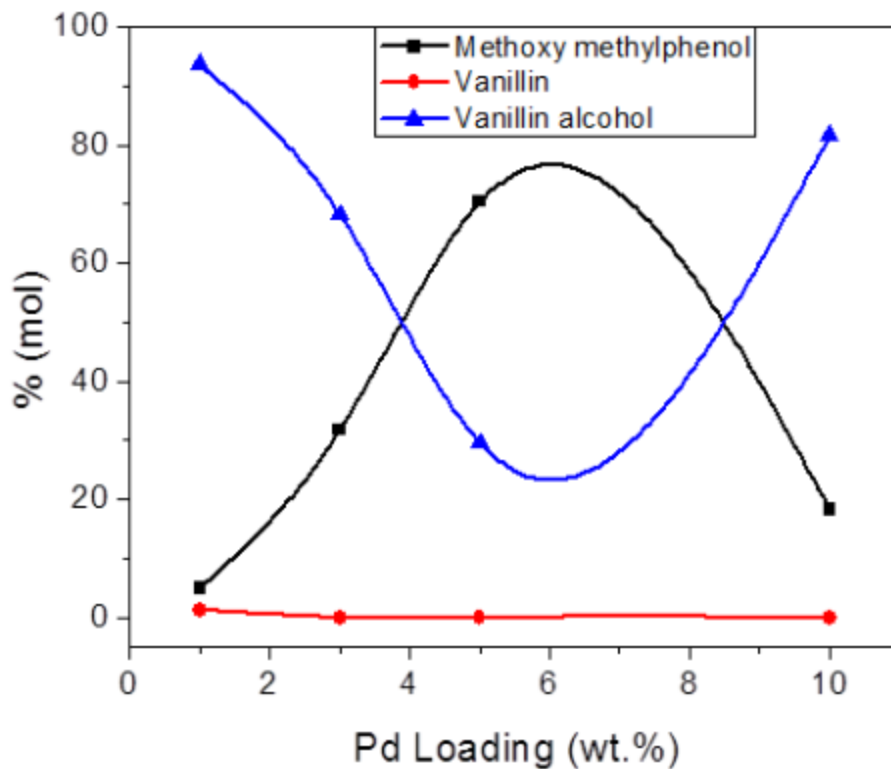


**Figure 36.** Mol% of vanillin, vanillyl alcohol, and 2-methoxy-4-methylphenol as a function of 1-10 wt% Pd in the Ce-MOF-PRGO support for the hydrogenation of vanillin. Reaction conditions: 0.3g vanillin, 40 mL water, 50 mg catalyst,  $T = 373\text{K}$ ,  $\text{H}_2$  Pressure = 1 mPA, and stir speed = 900 rpm,  $t = 120$  min.



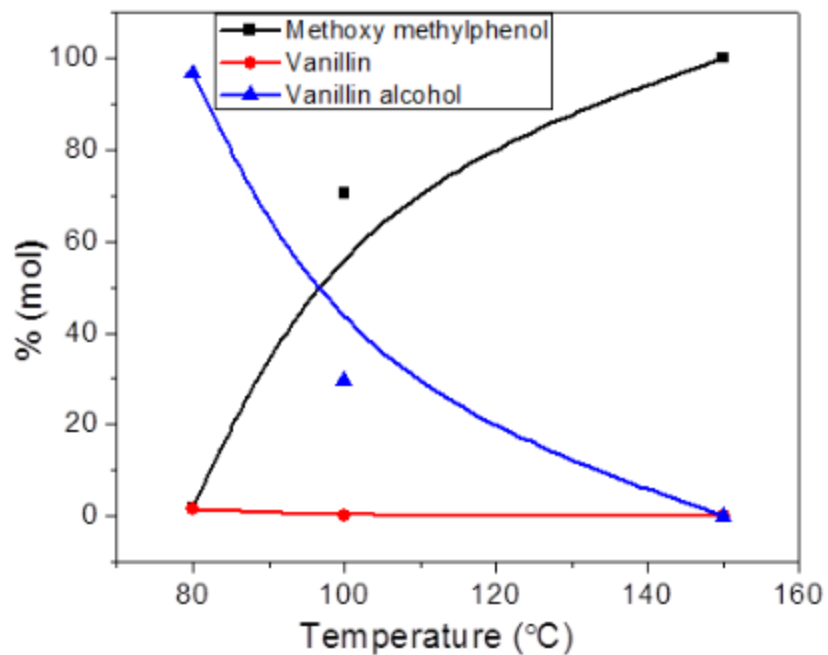


**Figure 37.** Mol% of vanillin, vanillyl alcohol, and 2-methoxy-4-methylphenol as a function of temperature for the 5% Pd/Ce-MOF-PRGO catalyst for the hydrogenation of vanillin. Reaction conditions: 0.3g vanillin, 40 mL water, 50 mg catalyst, H<sub>2</sub> Pressure = 1 mPA, and stir speed = 900 rpm, t = 120 min.

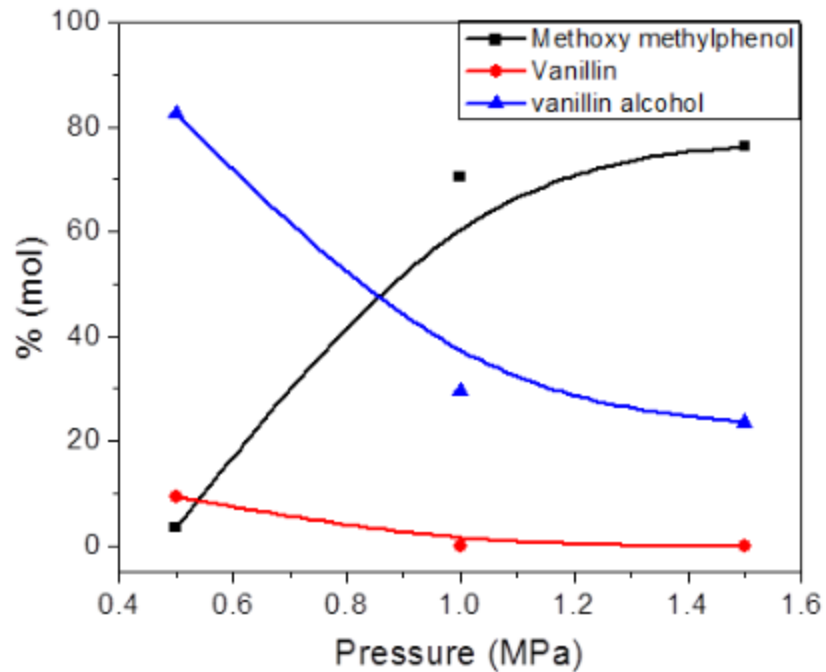


**Figure 38.** Mol% of vanillin, vanillyl alcohol, and 2-methoxy-4-methylphenol as a function of pressure for the 5% Pd/Ce-MOF-PRGO catalyst for the hydrogenation of vanillin. Reaction conditions: 0.3g vanillin, 40 mL water, 50 mg catalyst, Temperature = 373K, and stir speed = 900 rpm, t = 120 min.

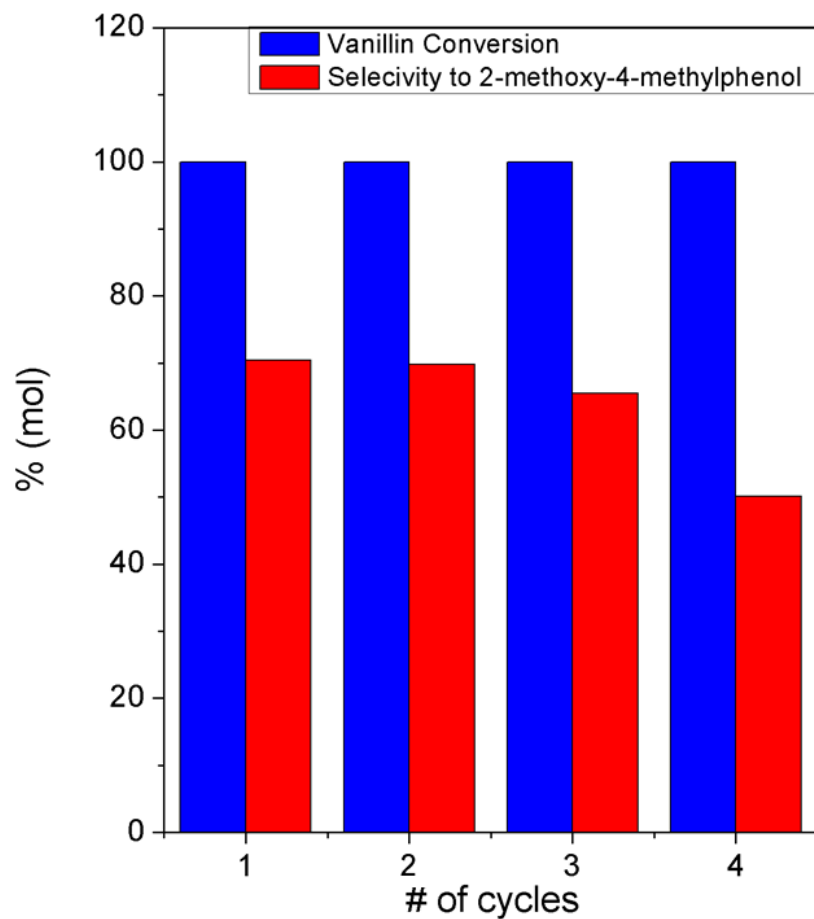


**Figure 39.** Reusability of 5% Pd/Ce-MOF-PRGO catalyst for the conversion and selectivity of vanillin into products. Reaction conditions: 0.3g vanillin, 40 mL water, 50 mg catalyst, T = 373K, H<sub>2</sub> Pressure = 1 mPA, and stir speed = 900 rpm, t = 120 min.

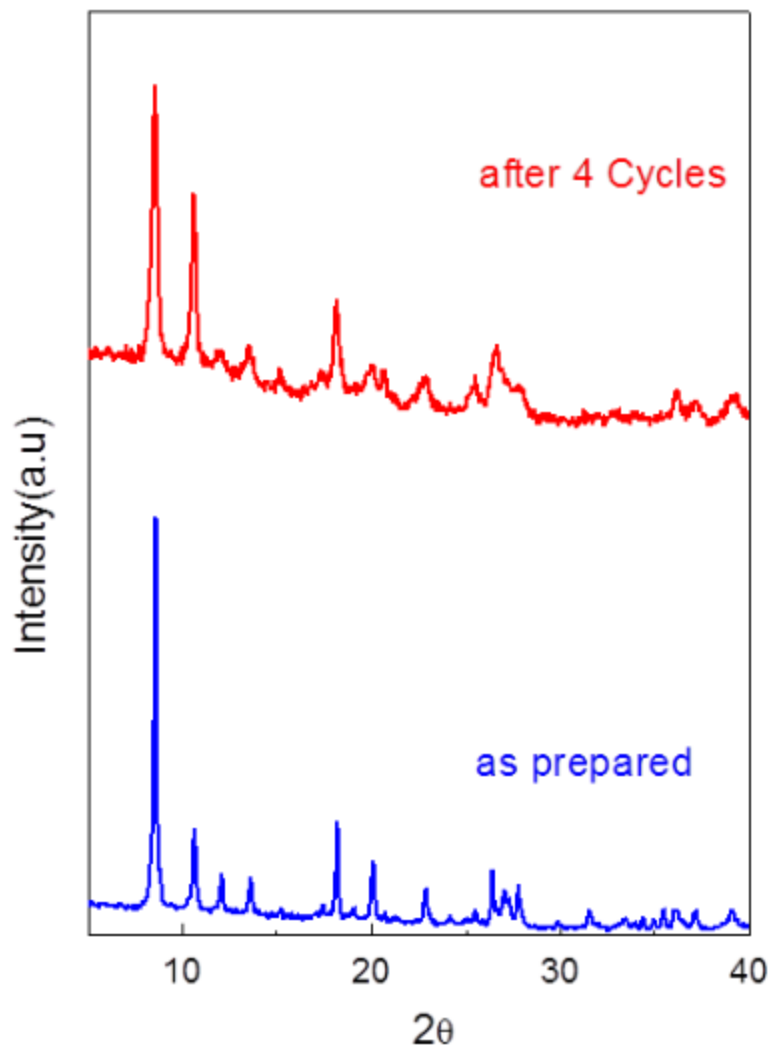


**Figure 40.** XRD of 5% Pd/Ce-MOF-PRGO before and after the vanillin hydrogenation reactions after recycling.

**Table 3.** Acidity values of 5 wt% Pd on Ce-MOF, Ce-MOF-PRGO, and RGO. TOF values calculated from number of active sites for mol% composition of 2-methoxy-4-methylphenol at 30 min.

| <b>Catalyst</b>   | <b>Number of Active Sites (mequiv/g)</b> | <b>Acid Strength (mV)</b> | <b>TOF (h<sup>-1</sup>)</b> |
|-------------------|--|---------------------------|-----------------------------|
| 5% Pd/Ce-MOF      | 0.52                                     | 43                        | 33.5                        |
| 5% Pd/Ce-MOF-PRGO | 0.72                                     | 148                       | 722.3                       |
| 5% Pd/RGO         | 0.55                                     | 50                        | 0                           |

**Table 4.** Pd dispersion, average particle size, number of active sites, metallic surface area, and TOF for 5% Pd supported on Ce-MOF, Ce-MOF-PRGO, and RGO. H<sub>2</sub> pulse chemisorption performed at 40 °C.

| Catalyst          | Palladium dispersion (%) | Particle size by pulse titration | Palladium active sites | Metallic surface area (m <sup>2</sup> /g) |
|-------------------|--------------------------|----------------------------------|------------------------|---|
| 5% Pd/Ce-MOF      | 9.8                      | 11.7                             | 1.4 x 10 <sup>18</sup> | 36.9                                      |
| 5% Pd/Ce-MOF-PRGO | 13.9                     | 11.0                             | 2.0 x 10 <sup>18</sup> | 84.3                                      |
| 5% Pd/RGO         | 5.4                      | 20.7                             | 1.2 x 10 <sup>18</sup> | 25.4                                      |

**Table 5.** Hydrogenation of vanillin over a series of different catalysts

| Catalyst  | Conversion (%) | Selectivity (%) | Reference |
|---|----------------|-----------------|-----------|
| 5% Pd/Ce-MOF-PRGO <sup>1</sup>                    | 100            | 100             | This work |
| 5% Pd/SWNT-SiO <sub>2</sub> <sup>2</sup>          | 85             | 47              | [112]     |
| Pd/CN <sup>3</sup>                                | 65             | 69              | [143]     |
| 4.5% Pd/MSMF <sup>4</sup>                         | >99.5          | 54              | [144]     |
| 2% Pd/MIL-101 (Cr) <sup>5</sup>                   | 86.4           | 82              | [128]     |
| 2% Pd/SO <sub>3</sub> H-MIL-101 (Cr) <sup>5</sup> | 100            | 100             |           |
| 2% Pd/UiO-66-NH <sub>2</sub> <sup>4</sup>         | 100            | 100             | [129]     |

[1] Reaction conditions: water, 40 mL; S/C (molar ratio of substrate to catalyst)=100,  $P_{H_2}$  =1 MPa;  $T$ =100 °C;  $t$ =240 min. [2] Reaction conditions: 1:1 v/v water/decalin, 20 mL; S/C=100;  $P_{H_2}$  =0.35 MPa;  $T$ =100 °C;  $t$ =30 min. [3] Reaction conditions: water, 20 mL; S/C=350;  $P_{H_2}$  =1.0 MPa;  $T$ =90 °C;  $t$ =60 min. [4] Reaction conditions: water, 20 mL; S/C=200;  $P_{H_2}$  =0.5 MPa;  $T$ =100 °C;  $t$ =60 min. [5] Reaction conditions: water, 20 mL; S/C=200;  $P_{H_2}$  =0.5 MPa;  $T$ =100 °C;  $t$ =120 min.

## Chapter 5: Acid Site Correlation to Selectivity of 2-Methoxy-4-Methylphenol in Hydrogenation of Vanillin

### 5.1 Introduction

The importance of the hydrogenation of vanillin was previously addressed in the introduction of Chapter 4. The hydrogenation of vanillin into 2-methoxy-4-methylphenol is an important model for the upgrade of biofuel into value-added chemical products. The feasibility of the reaction was previously demonstrated, but the activity of the catalyst can be improved further. It was noted that the acidity of a material is an interesting and unstudied variable on the catalytic hydrogenation of vanillin. The conversion of vanillin into 2-methoxy-4-methylphenol follows a two-step process: hydrogenation (favorable) followed by hydrogenolysis (unfavorable). In order to efficiently convert vanillin into the fully hydrodeoxygenated compound, a palladium and tungstophosphoric acid (HPW) co-catalyst is proposed as an acidified catalyst. It is believed that the high acidity of the material can alter the mechanism.

Metal oxides, such as zirconia,[145] titania, silica, and alumina have been used for the fast pyrolysis of grainstock into biofuel.[93] However, such material have very low surface area measurements (<100 m<sup>2</sup>/g) and are unsuitable for loading with significant amounts of noble metal catalysts due to low porosity. MOFs are a support that are able to fully encage nanoparticles due to higher surface areas, and MOFs have proven to be a stable heterogeneous catalyst for the catalytic upgrade of biomass into biofuel.[14-18]

A three dimensional zirconium-based UiO-66-NH<sub>2</sub> MOF (Figure 41)[146] with a tetragonal bipyramidal crystal structure was utilized for the hydrogenation of vanillin into products as a model for biofuel upgrade due to its thermal stability of up to 500 °C and high surface area from micropores. This material was incorporated with palladium and HPW as co-catalysts. Noble



metal nanoparticles such as palladium and platinum aggregate due to heat, reducing overall surface area and quickly ending their usefulness as a recyclable catalyst. [13] Thermally stable MOFs play an important role in catalysis and have been catapulted to the forefront of research because of their ability to confine nanoparticles in pores and prevent aggregation into bulk substance amidst a reaction,[21] while their porosity still allows catalysts to interact with substrate material.

HPW is included as a superacid co-catalyst to increase the acidity of the material.[147] Activity increases with the inclusion of solid acid Keggin polyanions such as HPW because such materials have a lower Hammett acidity value of  $\text{H}_2\text{SO}_4$ . [94, 148] HPW is the most acidic heteropolyacid, but leaching is a concern due to its high solubility in water. It must be supported. Some research has been done in the past to determine the correlation between number of acidic sites, BET surface area, and activity of materials such as MIL-101 and MCM-41.[42] It is known that the addition of HPW to a support drastically promotes catalyst activity. Confinement of HPW within the pores of a MOF is a strategy to prevent leaching of a hydrophilic polyoxometallate during catalytic testing.[148-149] Solid acids encapsulated into a support structure would allow for acid-catalysis to occur without concern for acidic waste elimination.[150]

This design strategy of using co-catalytic HPW and palladium nanoparticles is illustrated in Figure 42. Low loadings of palladium particles were impregnated into HPW/UiO-66-NH<sub>2</sub> where the cheaper HPW catalyst provides additional active sites for reactions while serving as a partial substitution for the palladium. High catalytic efficiency was achieved for the two-step reaction of vanillin hydrogenation with these catalysts, and a relationship between the acidic sites and the selectivity for the hydrogenation of vanillin into 2-methoxy-4-methylphenol was established. It is proposed that the mechanism of this reaction can be altered by the presence of a strong Brønsted acid.

## 5.2 Characterization

XRD analysis (Figure 43) suggests that the HPW was fully encapsulated and that the crystal structure of the material remain undamaged. The encapsulation of palladium does not affect the crystallinity of the UiO-66-NH<sub>2</sub>. The parent material XRD diffraction peaks are retained for all samples, as seen in Figure 43.[25, 151-152] No peaks were detected for palladium due to the high dispersion of palladium nanoparticles. [20, 38]. For lower HPW loading, the crystal structure remains unchanged.[153] The perfect crystallinity is maintained with additional HPW until 20% HPW. At 20% HPW loading, the HPW uptake into UiO-66-NH<sub>2</sub> has approached saturation leading to aggregation and layering of HPW on the surface of the MOF. The well-studied HPW Keggin polyanion has been reported to have sharp XRD peaks at 9.3°, 10.9°, and 26° 2 $\theta$ , [154] which are clearly present in the XRD patterns for 20% HPW/UiO-66-NH<sub>2</sub>.

Figure 45A show SEM micrographs of UiO-66-NH<sub>2</sub> loaded with HPW and Pd. The distinct tetragonal bipyramidal morphology of the UiO-66-NH<sub>2</sub> crystals give further evidence that the addition of HPW and palladium does not distort the crystallinity of the MOF. Figure 45B shows the TEM image of the 5% HPW UiO-66-NH<sub>2</sub> 0.4% Pd. Palladium nanoparticles are not easily seen in the 5% HPW UiO-66-NH<sub>2</sub> 0.4% Pd sample due to the small size of the nanoparticles encapsulation within the zirconium MOF structure. The palladium is expected to be around 1.2 nm in size.[155]

The TEM image of the as-synthesized UiO-66-NH<sub>2</sub> material (Figure 46A) was compared to the 5% HPW UiO-66-NH<sub>2</sub> material (Figure 46B). There is no difference in the morphology of the tetragonal bipyramidal UiO-66-NH<sub>2</sub> crystals after inclusion of HPW.

Further analysis was performed to confirm the presence of palladium inside the samples: XPS spectroscopy (Figure 47) revealed weak peaks at 334.93, 336.97, 342.42, and 343.7 eV,

which are related to  $\text{Pd}^03\text{d}^{5/2}$ ,  $\text{Pd}^{2+}3\text{d}^{5/2}$ ,  $\text{Pd}^03\text{d}^{3/2}$ , and  $\text{Pd}^{2+}3\text{d}^{3/2}$  respectively. These weak peaks may be due to the low loading of palladium on the sample relative to the intense  $\text{Zr}3\text{p}^{3/2}$  and  $\text{Zr}3\text{p}^{1/2}$  overlapping peaks, which is expected of palladium inside zirconium-based supports.[156] The majority oxidation state of the catalyst is shown to be Pd(0), as shown in Table 6. The actual loading of palladium was measured by ICP which indicated low uptake of 0.4 wt% for all samples except for the 20% HPW-UIO-66-NH<sub>2</sub>, which was 0.7 wt%.

FTIR spectroscopy (Figure 44) show that the incorporation of HPW inside the pores did not destroy or collapse the framework of the UIO-66-NH<sub>2</sub>. Intense peaks for N-H bending ( $1630\text{ cm}^{-1}$ ), secondary amides ( $1570\text{ cm}^{-1}$ ) and C-N stretches ( $1240\text{ cm}^{-1}$ ) are present.[156] Peaks correlated to HPW are difficult to differentiate at lower loadings due to full encapsulation. By increasing the loading of HPW to 20%, the spectrum shows peaks located at 1102, 1082, 985 and  $889\text{ cm}^{-1}$ , which are characteristic for the HPW.[157] This is in a good agreement with conclusions drawn from XRD patterns (Figure 43), where passivation of the zirconium MOF surface occurs due to overabundance of HPW.

Figure 48 shows that the surface area was unhampered with the addition of HPW, which is to be expected. A previous *in-situ* loading of HPW into a non-amine-functionalized water-modulated UiO-66 found that 25% HPW loading caused a decrease in surface area from 874 to  $806\text{ m}^2/\text{g}$ .[158] In our material, the surface area decreased from 1225 to  $1173\text{ m}^2/\text{g}$  (Table 7) with the addition of 20% HPW. The theoretical surface area of HCl-modulated UiO-66-NH<sub>2</sub> is approximately  $1200\text{ m}^2/\text{g}$ .[38]

### 5.3 Acidity Measurement by Pyridine Adsorption and n-Butylamine Titration

Pyridine adsorption is a technique typically utilized for determination and quantification of Lewis and Brønsted acid sites by peak area calculations in the  $1400\text{-}1640\text{ cm}^{-1}$  FTIR range.

Figure 49 shows the FT-IR spectra of the HPW/UiO-66-NH<sub>2</sub> catalyst systems before and after pyridine adsorption. Due to the 2-amino-terephthalic organic linkers, UiO-66-NH<sub>2</sub> typically exhibits strong peaks at 1574 (NH<sub>2</sub>), [25] 1498 (aromatic C=C), and 1429 cm<sup>-1</sup> (aromatic C=C). After exposure of pyridine probe molecules to the samples to determine the ratio of Brønsted to Lewis acid sites, it was observed that these peaks shifted slightly towards 1566, 1493, and 1441 cm<sup>-1</sup> respectively after adsorption of pyridine molecules. Typically, bands at 1440 and 1490 cm<sup>-1</sup> are observed for pyridine attached to Lewis acid sites, and a peak at 1545 cm<sup>-1</sup> is a strong indicator for the presence of Brønsted acid sites. [159] In this case, the adsorption of pyridine has resulted in some peak shifts due to overlap of previously existing organic linker functional groups with pyridine adsorption to strongly Brønsted or Lewis sites. This effect is more pronounced as the sample becomes more acidic; it can be seen for 20% HPW/UiO-66-NH<sub>2</sub> that shoulders develop at 1545 cm<sup>-1</sup> due to high acid site presence, but the exact ratio is indeterminate. While extensively studied for alumina [160] and zeolites, [161] no method of molecular site probing has been developed for MOF systems. Admittedly, the knowledge of Brønsted acid site probing has not been well studied and acid site ratios are thus difficult to quantify. [162-163] Ammonia and pyridine probe molecules are merely approximations for Brønsted and Lewis site determination due to overlap with amines, alkenes, and carboxyl groups present in the organic linker.

The acid strength and total number of acid sites have been measured by potentiometric nonaqueous titration with n-butylamine (Figure 50), where the initial electrode potential ( $E_i$ ) shows the acid strength. The total number of acid sites (acidity) can be calculated from the value of the mequiv n-butylamine/g solid. [137] The  $E_i$  ranges from <0 mV (weak acid sites) to >100 mV (very strong acid sites). [138] The acid strength of acid sites were indicated from the initial electrode potential. The titration saturation point indicated the total number of acid sites, [41] and Table 8

shows that the acid strength of UiO-66-NH<sub>2</sub> is 17 mV. The low acidity may be due to the presence of unsaturated Zr sites, which are weakly Lewis acidic.[155, 164-165] Following the incorporation of HPW, acidity increased significantly to reach the maximum initial acid strength of 108 mV for 5% HPW loading. This is a result of generation of new acid sites due to addition of HPW into the MOF cavity.[162, 166] At 20% HPW loading into UiO-66-NH<sub>2</sub> supports, the E<sub>i</sub> potential continues to increase to 239 mV due to passivation of surface with excess HPW. The total number of acid sites has been increased proportionally to an increased amount of HPW loaded into the prepared UiO-66-NH<sub>2</sub> support.

#### **5.4 Pore Volume and Kinetic Diameter for Uptake of HPW into UiO-66-NH<sub>2</sub> and Mass Transfer Limitations of Vanillin into the Pores of UiO-66-NH<sub>2</sub>**

The UiO-66 and UiO-66-NH<sub>2</sub> series are well-known to have a pore size of 0.6 nm, but the pore size distribution is tunable by varying the coordination of zirconium nodes. The usage of a modulator such as HCl during the synthesis is known to result in missing linker defects because HCl coordinates to the zirconium node secondary building unit synthesis and prevents full coordination of nodes to linkers, and surface area increases as well.[38] Modulators are typically required during synthesis of certain MOFs for the templated growth of crystal using assistive coordination molecules. The regular synthesis of UiO-66 employs a small amount of DI water for this purpose. As a result of substituting water with HCl as a modulator, the average pore size of UiO-66-NH<sub>2</sub> increase from 0.6 nm to of 0.8-1.15 nm as a function of HCl concentration due to missing linker defects.[38]

The full pore size distribution of UiO-66-NH<sub>2</sub> is shown in Figure 51. It can be seen that two distinct pore sizes are present, for tetrahedral and octahedral pores. Whereas the average is

1.15 nm, the full pore size distribution includes a range of 1-1.5 nm. Tetrahedral pores are seen around 10Å and larger octahedral pores are seen at 15Å.[167]

This pore window size is able to accommodate both the ultra-small palladium nanoparticles (~1.5 nm) and HPW (1.3 nm)[168] because the pore volume (0.38 cm<sup>3</sup>/g)[169] can still accommodate HPW particles (0.23 cm<sup>3</sup>/g).[168, 170] MIL-101 has enough pore volume (2.01 cm<sup>3</sup>/g)[171] to accommodate five HPW ions,[168] so UiO-66-NH<sub>2</sub> is expected to hold less due to lower surface area and pore volume, which is in accordance with the lower wt% HPW to achieve saturation relative to MIL-101. The size discrepancy between the 1.3 nm kinetic diameter of HPW and the snug 1.5 nm pore size of the UiO-66-NH<sub>2</sub> is an obvious point of concern, but there are multiple reasons as to why the loading of UiO-66-NH<sub>2</sub> was successful. Firstly, despite the slightly smaller diameter of the HPW relative to the UiO-66 pore size, the loading of HPW was successful due to greater diffusion induced by increasing of stir speed and time, which overcomes external mass transport limits. Secondly the uptake of the HPW into the MOF, or the wt% as determined by ICP analysis, was low with respect to nominal loading: an intended 5-50 wt% resulted in only 1-20 wt% after several hours of vigorous stirring. The uptake of HPW was low relative to nominal loadings, compared to *in situ* encapsulated HPW-MOF systems, so it is known that HPW fits snugly within this MOF.[172] It was previously discussed that such one-pot loadings of 25% HPW decreased the surface area of a water-modulated UiO-66-NH<sub>2</sub> from 874 to 806 m<sup>2</sup>/g.[158]

Diffusivity of molecules into a porous material is highly relevant for catalytic applications. In addition to the external mass transport limitations of HPW into the pores of the UiO-66-NH<sub>2</sub>, it is imperative that a reactant molecule is able to enter as well. UiO-66-NH<sub>2</sub> synthesized with DI water modulator has a pore size of 0.6 nm, as previously stated.[38] The difficult permeability of vanillin molecules (0.7 nm) into non-HCl modulated UiO-66-NH<sub>2</sub> has been a point of concern.

However, both the internal and external mass transport limitations of vanillin into such pores is easily overcome.[155, 173]

Given that a previous study suggested that a molecule of 0.7 nm can permeate a pore size of 0.6 nm for water-modulated UiO-66-NH<sub>2</sub>,[155] it is feasible to suggest an HPW molecule of 1.3 nm can enter a pore sizes up to 1.5 nm for HCl-modulated UiO-66-NH<sub>2</sub> given excessive stirring and time. This is in good agreement with characterization, low wt% with respect to nominal wt%, and catalytic vanillin hydrogenation results, where activity is measured as a function of incorporated acid sites.

A MOF with a mismatching kinetic diameter, MIL-53, was chosen as a blank study for uptake of HPW. MIL-53 has 1-D diamond-shaped pores with a size of 0.7 nm and is considered much too small for HPW.[174] The XRD showed that nominal loadings of 10-33 wt HPW completely passivated MIL-53 (Figure A3), resulting in highly distorted XRD peaks, similar to 20% HPW/UiO-66-NH<sub>2</sub>. ICP measurements of HPW present in 10-33 wt HPW/MIL-53 showed that all samples adsorbed only 0.5% HPW. It can be inferred that the pores sizes were too small for HPW and that very little were engaged as a result of immediate saturation. The XRD for 5% HPW/UiO-66-NH<sub>2</sub> did not lose any peak features due to successful encasement and accommodation of HPW molecules, which agreed with ICP measurements.

### **5.5 Effect of 0-20 wt% HPW/UiO-66-NH<sub>2</sub> for Hydrogenation of Vanillin**

The hydrogenation of vanillin into 2-methoxy-4-methylphenol is a two-step process, as shown in Figure 52, with vanillyl alcohol as an unwanted intermediate.[175] The accepted mechanism for the hydrogenation of vanillin into 2-methoxy-4-methylphenol is as follows: firstly, hydrogen is captured by a catalyst and transferred onto vanillin, resulting in hydrogenation of vanillin into vanillyl alcohol with addition of hydrogen to either end of a C=O bond with

conversion of an aldehyde into an alcohol; secondly, a C-OH bond is broken with the addition of another hydrogen-addition step through hydrogenolysis to yield 2-methoxy-4-methylphenol. The second step requires far more energy and is considered the rate limiting step due to low favorability of hydrogenolysis relative to hydrogenation. It is easier to add H<sub>2</sub> to a C=O bond than to break a C-OH bond with addition of H<sub>2</sub>.

The conversion of vanillin into products is shown in Figure 53 as a function of 0-20 wt% HPW. UiO-66-NH<sub>2</sub> 0.4% Pd with no HPW achieved a 95% conversion of vanillin into products within 30 min, but only 20% selectivity towards the desirable 2-methoxy-4-methylphenol product. Conversion is defined as the percentage of vanillin converted into products, where selectivity is the percentage of products that were desirable. All conversion and selectivity calculations were determined by analysis of peak areas from GC-MS; ratios of area-under-the-curve of eluting peaks were converted into percentages.

The majority of the product formed was the vanillyl alcohol intermediate. Incremental loading of the samples with HPW greatly affected the selectivity, but not the conversion. It can be seen from Figure 53B-E that incorporation of 1-20% HPW into UiO-66-NH<sub>2</sub> 0.4% Pd drastically increases the selectivity as a function of increased HPW content. UiO-66-NH<sub>2</sub> 0.4% Pd achieved 20% selectivity towards 2-methoxy-4-methylphenol. This is increased to 22%, 40%, 80%, and 98%, respectively, as a function of 1-20% HPW content. Figure 53F shows the mol% of 2-methoxy-4-methylphenol present at one hour, as determined by GC-MS area-under-the-curve analysis of retention peaks. The mol%, or mole fraction, is the fraction of all compounds identified by GC-MS as 2-methoxy-4-methylphenol. The total 2-methoxy-4-methylphenol by the 1 h interval is drastically increased because the selectivity increases as %HPW content despite conversion staying approximately the same. All samples achieved approximately 90% conversion



by 30 min regardless of HPW content. Figure 54A show the 2-methoxy-4-methylphenol mol% as a function of 1-20% HPW UiO-66-NH<sub>2</sub> 0.4% Pd catalysts over time.

It was previously discussed that the acidity of the HPW/UiO-66-NH<sub>2</sub> material increased as a function of HPW content. Potentiometric readings of initial acid strength were shown in Table 8. The acid strength of the materials are directly correlated to the mol% of 2-methoxy-4-methylphenol generated by an hour in Figure 54B. As the HPW content increased from 0 to 20%, the  $E_i$  of the material increased from 17 to 239 mV. The selectivity of the catalyst towards 2-methoxy-4-methylphenol over the intermediate vanillyl alcohol as a consequence. There is a direct trend between the acidity of a catalyst and its selectivity towards the fully hydrogenated product because no other parameters have changed. This is a strong indication that the acid sites play a role previously unexplored, but of utmost importance for this particular reaction. A mechanism is proposed for the role of a strong acid like HPW in the second step of the vanillin hydrogenation reaction.

### **5.6 Altered Vanillin Hydrogenation Mechanism in the Presence of a Strongly Acidic Catalyst and the Effect of HPW on Selectivity**

It is proposed the presence of a strongly acidic catalyst, such as a Brønsted acid like HPW, would affect only the second half of the reaction, the hydrogenolysis step. The first hydrogenation step is not affected by the presence of a strong acid. This is strongly evidenced by the change in selectivity of products, where the product is contingent on the hydrogenolysis of a C-OH bond. No effect of increased acidity from 0-20% HPW loading was observed on the first-step conversion of vanillin. This assumption was proved using comparing vanillin and vanillyl alcohol as initial stock.

Two starting materials (vanillin and vanillyl alcohol) and three different supports (UiO-66-NH<sub>2</sub>, 5% HPW UiO-66-NH<sub>2</sub>, and 5% HPW UiO-66-NH<sub>2</sub> 0.4% Pd) were subjected to the same conditions used in vanillin hydrogenation. It was important to observe which reactants could be hydrogenated by which catalysts. The conversion of initial reactant into product is exhibited in Table 9.

The catalytic activity of 5% HPW/UiO-66-NH<sub>2</sub> 0.4% Pd was as previously stated: conversion occurred regardless whether vanillin or vanillyl alcohol was used as reactant. On the other hand, it was observed that the parent UiO-66-NH<sub>2</sub> material failed to exhibit any activity. There was no conversion of vanillin into vanillyl alcohol, and when vanillyl alcohol was used as the initial reactant, there was no conversion of vanillyl alcohol into 2-methoxy-4-methylphenol. The 5% HPW/UiO-66-NH<sub>2</sub> sample is interesting and confirms the previous result, which was that the presence of HPW did not affect the conversion of vanillin into products and only affected selectivity. In Table 9, it can be seen that when vanillin is used as the initial stock, no conversion occurs for the 5% HPW/UiO-66-NH<sub>2</sub> sample due to absence of palladium. However, for 5% HPW/UiO-66-NH<sub>2</sub>, conversion occurs for vanillyl alcohol. 9% of the vanillyl alcohol is converted into 2-methoxy-4-methylphenol when only HPW is present within UiO-66-NH<sub>2</sub>. UiO-66-NH<sub>2</sub> was not able to convert the vanillin or vanillyl alcohol, but 5% HPW UiO-66-NH<sub>2</sub> was able to successfully convert some of the vanillyl alcohol into 2-methoxy-4-methylphenol within 15 min while being inactive for vanillin. This trend gives an interesting insight into the mechanism, which is proposed in Figure 55: HPW can help in the removal of –OH functional groups. Therefore, the inclusion of a strong acid catalyst could allow the reaction to proceed down a dehydration-hydrogenation pathway rather than the traditional hydrogenolysis pathway for the second step of the vanillin hydrogenation reaction.

The hydrogenation of vanillin into the intermediate vanillyl alcohol has been well studied.[97, 176] Figure 55 shows a proposed dehydration-hydrogenation of the intermediate vanillyl alcohol into 2-methoxy-4-methylphenol by a new pathway. The alcohol is protonated in the presence of a strong acid and is dehydrated by the removal of water. The benzylic carbocation undergoes several intermediate states by benzylic resonance within the aromatic ring, and the alcohol is oxidized to a ketone to fill the cation. The alkene is hydrogenated by hydrogen provided by palladium catalyst to yield 2-methoxy-4-methylphenol.

It has been previously reported that bifunctional catalysts increase the selectivity of products for glycerol hydrogenation.[177-178] In this case, it is believed that acid catalyzed dehydration occurs quickly due to the high acidity of the HPW.[179] The *syn* addition of hydrogen via hydrogenation of C=C bonds is more favorable than the hydrogenolysis of C-O bonds, and could be why the incremental increase of HPW resulted in a proportionally increase in selectivity. Similar to the case of glycerol hydrogenation, the intermediate resonance structure are never detected by the GC-MS due to its small concentration relative to the presence of water.[177-178] Therefore, it is asserted that the loading of a Keggin acid diverts the hydrogenolysis of intermediate vanillyl alcohol pathway into an alternative dehydration-hydrogenation pathway, resulting in a higher selectivity for 2-methoxy-4-methylphenol in the vanillin hydrogenation reaction.

Because of the altered pathway, less palladium is necessary. In this system, only 0.4% palladium is necessary to catalyze the first step of the reaction, where vanillin is hydrogenated into vanillyl alcohol. In the second step, having a co-catalyst such as a cheaper HPW allows for the rapid conversion of vanillyl alcohol into the final desired product. One of the challenges of green energy sources is the efficient usage of palladium metal catalysts. Noble metal catalysts are

expensive. Here, full conversion of vanillin into 2-methoxy-4-methylphenol is demonstrated with minimal palladium catalyst.

A comparison of turnover frequency (TOF) numbers in terms of palladium content is calculated in Table 10 for the 30 min interval. The TOF is determined from:

$$TOF = \frac{N_{product}}{N_{catalyst}} \times \frac{1}{h}$$

**Equation 2.** Turnover Frequency (TOF) formula.

where N is Avogadro's number. The molecules of 2-methoxy-4-methylphenol formed is compared to the molecules of catalytic palladium present, as a function of time.

Typical catalysts for this particular reaction utilize 2-10% Pd. A TOF of 1670h<sup>-1</sup> is achieved with the 5% HPW/UiO-66-NH<sub>2</sub> 0.4% Pd catalyst, which is higher than the TOF numbers of many other supports due to the low content of noble metal utilized. The 20% HPW/UiO-66-NH<sub>2</sub> 0.4% Pd (TOF = 1170) was determined to be less efficient than the 5% HPW/UiO-66-NH<sub>2</sub> 0.4% Pd catalyst because the reaction for both are nearly complete within 30 min. However, leaching is a concern for the 20% HPW/UiO-66-NH<sub>2</sub> 0.4% Pd sample, making the 5% HPW/UiO-66-NH<sub>2</sub> 0.4% Pd catalyst better overall. It can be seen that UiO-66-NH<sub>2</sub> is an excellent support for palladium for this reaction. When the amount of palladium loaded is decreased to merely 0.4% Pd, this catalyst is still highly competitive with several other supports, including carbon-based supports (CNT, carbon microspheres), MOFs (MIL-101 (Cr)), and metal oxides (TiO<sub>2</sub>). With the addition of HPW, the %mol composition of the desired product surges and is far better than similar catalysts for the hydrogenation of vanillin. A UiO-66-NH<sub>2</sub> with only 0.4% Pd but 5% HPW has equal activity and recyclability compared to UiO-66-NH<sub>2</sub> 2% Pd, but HPW is a far cheaper catalyst

component. Comparison against the UiO-66-NH<sub>2</sub> 2% Pd sample shows that a very small amount of palladium would yield full conversion of vanillin into vanillyl alcohol, but the hydrogenolysis reaction is the limiting step for selectivity. The advantages of the 5% HPW UiO-66-NH<sub>2</sub> system are twofold: First, this acidic catalyst is a cheap substitute for palladium noble metal; second the unfavorable hydrogenolysis step is bypassed with a dehydration-hydrogenation alternative permitted by the addition of such an acid catalyst. This further shows the promise of co-catalytic systems.

### **5.7 Recycling of 5% HPW/UiO-66-NH<sub>2</sub> and ICP Analysis for Leaching**

HPW excels as a homogeneous catalyst but has difficulties with regards to heterogeneous catalysis due to leaching.[39, 180-182] The 20% HPW UiO-66-NH<sub>2</sub> 0.4% Pd sample was not stable and could not be used for a second time due to dramatic leaching of both palladium (50% loss of 0.7% Pd) and HPW (80% loss of 20% HPW). In the first recovery test of this material, activity was decreased by 50%. 5% HPW UiO-66-NH<sub>2</sub> 0.4% Pd was reused 4 times without losing activity and without significant loss of HPW or palladium due to successful incorporation of catalyst within the confines of the HPW UiO-66-NH<sub>2</sub>. This trend is seen in Figure 56A. Figure 56B shows the XRD patterns for the catalysts after recycling. The 20% HPW UiO-66-NH<sub>2</sub> 0.4% Pd sample lost the characteristic peaks for the HPW after recycling due to leaching of surface HPW while the 5% HPW UiO-66-NH<sub>2</sub> 0.4% Pd sample remains unchanged. This proves the prior postulation that 20% HPW loading oversaturated of the support and lead to surface deposition while 5% HPW was an optimal amount successfully trapped in the pores with the highest activity.

Tungstophosphoric acid (HPW), a superacid, has been successfully incorporated into the structure of UiO-66-NH<sub>2</sub> alongside palladium nanoparticles with high activity and recyclability. Analysis of the trends in the E<sub>i</sub> in the n-butylamine titrations of these catalysts allowed for the

discernment of the HPW saturation in the UiO-66-NH<sub>2</sub> material and the optimal wt% of HPW was discovered. Additionally, a highly correlational trend was detected between the acid site concentrations determined by n-butylamine and the selectivity of a catalyst for the fully hydrogenated product 2-methoxy-4-methylphenol in the vanillin hydrogenation through heterogeneous catalysis.

A superacid can be used as a partial noble metal substitute in certain catalytic reactions, which are dependent on the presence of acid sites, such as the hydrogenolysis of vanillyl alcohol into 2-methoxy-4-methylphenol. The goal of this work was to encage HPW into a certain MOF as a symbiotic co-catalyst to noble metals. This is dependent on a kinetic diameter match of the HPW with the pore size and pore volume of such porous materials. The addition of noble metals to the HPW/MOF allows them to not only participate in the heterogeneous catalysis process but act as anchors or blockages that prevent significant HPW leaching into solution.

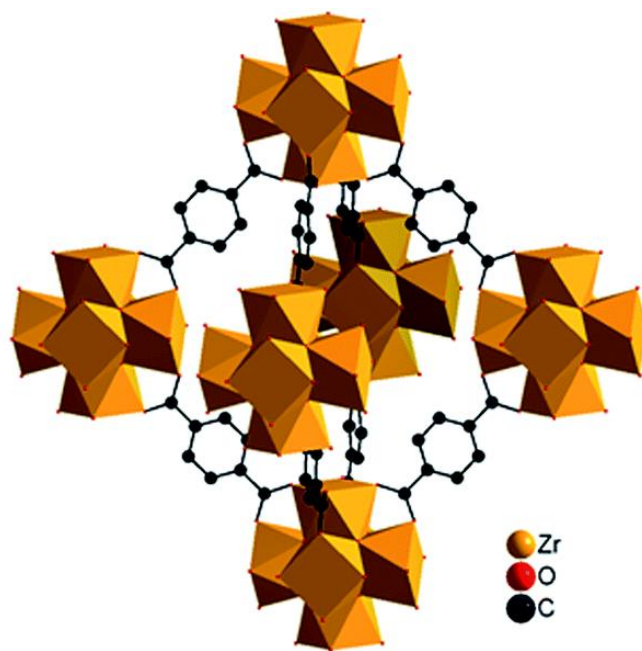


**Figure 41.** Crystal structure of UiO-66 (zirconium oxide secondary building units, or nodes, with 8-coordinated zirconium and 1.15 nm pore size).

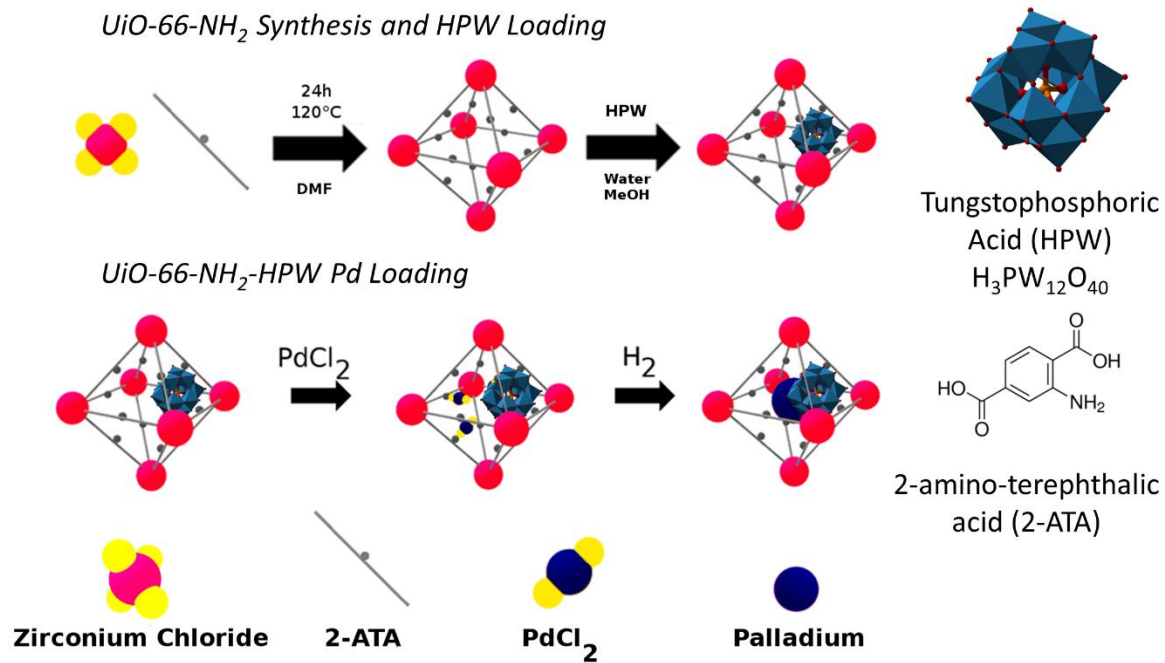


**Figure 42.** Pd nanoparticles on HPW/UiO-66-NH<sub>2</sub> design strategy.



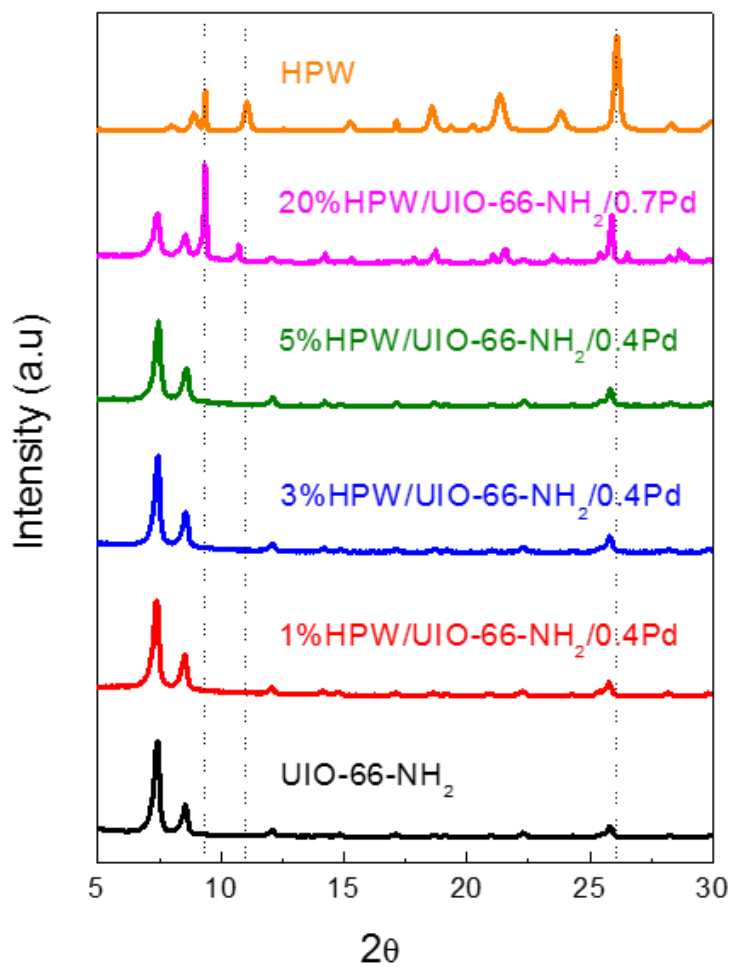


**Figure 43.** XRD diffractogram of UiO-66-NH<sub>2</sub> as a function of HPW content. All samples contain palladium nanoparticles.

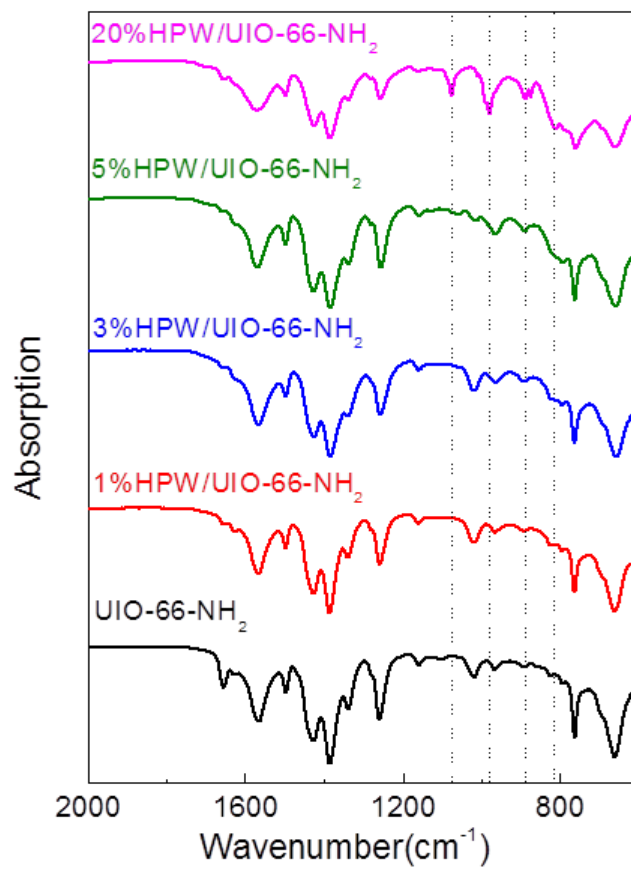


**Figure 44.** FTIR spectra of 0-20 wt% HPW/UiO-66-NH<sub>2</sub> 0.4% Pd

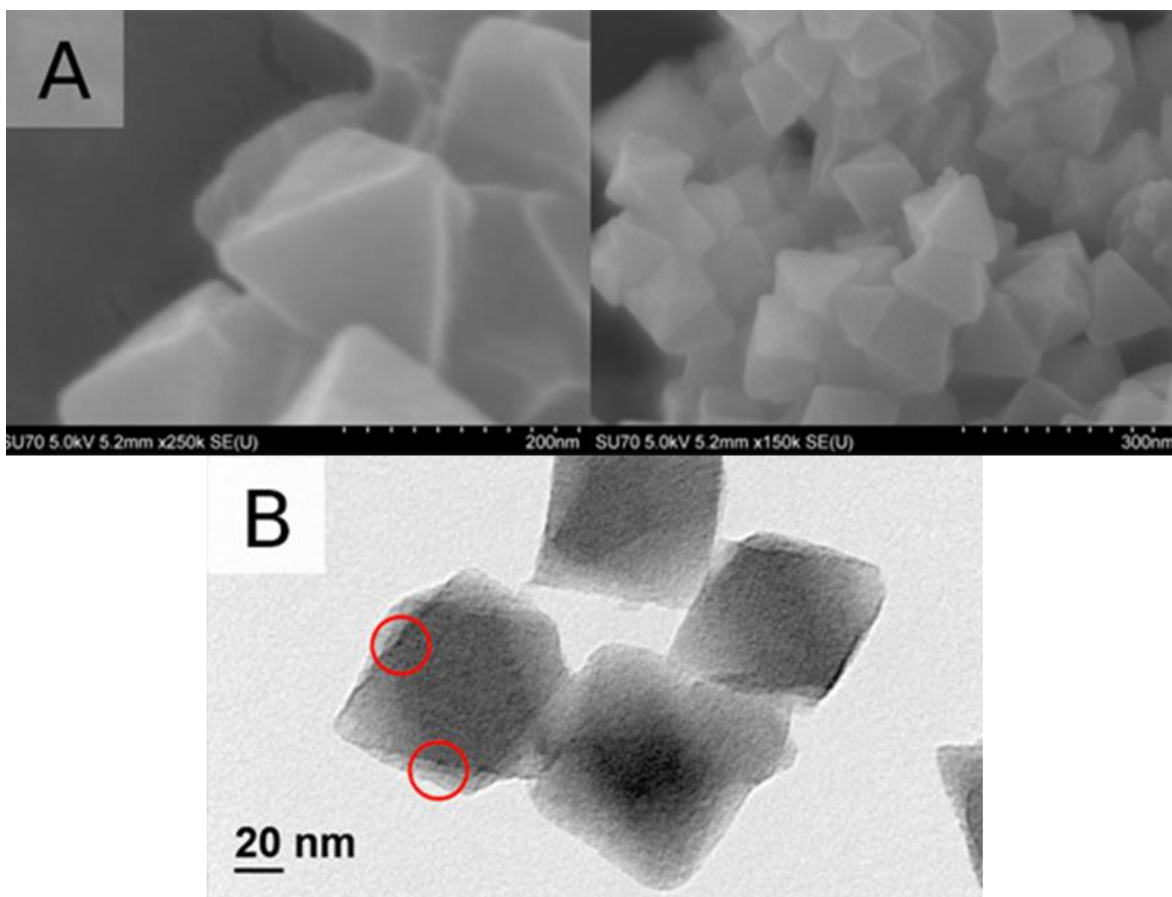


**Figure 45.** SEM (A) and TEM (B) of 5% HPW/UiO-66-NH<sub>2</sub> 0.4% Pd. Palladium nanoparticles are circled in red.

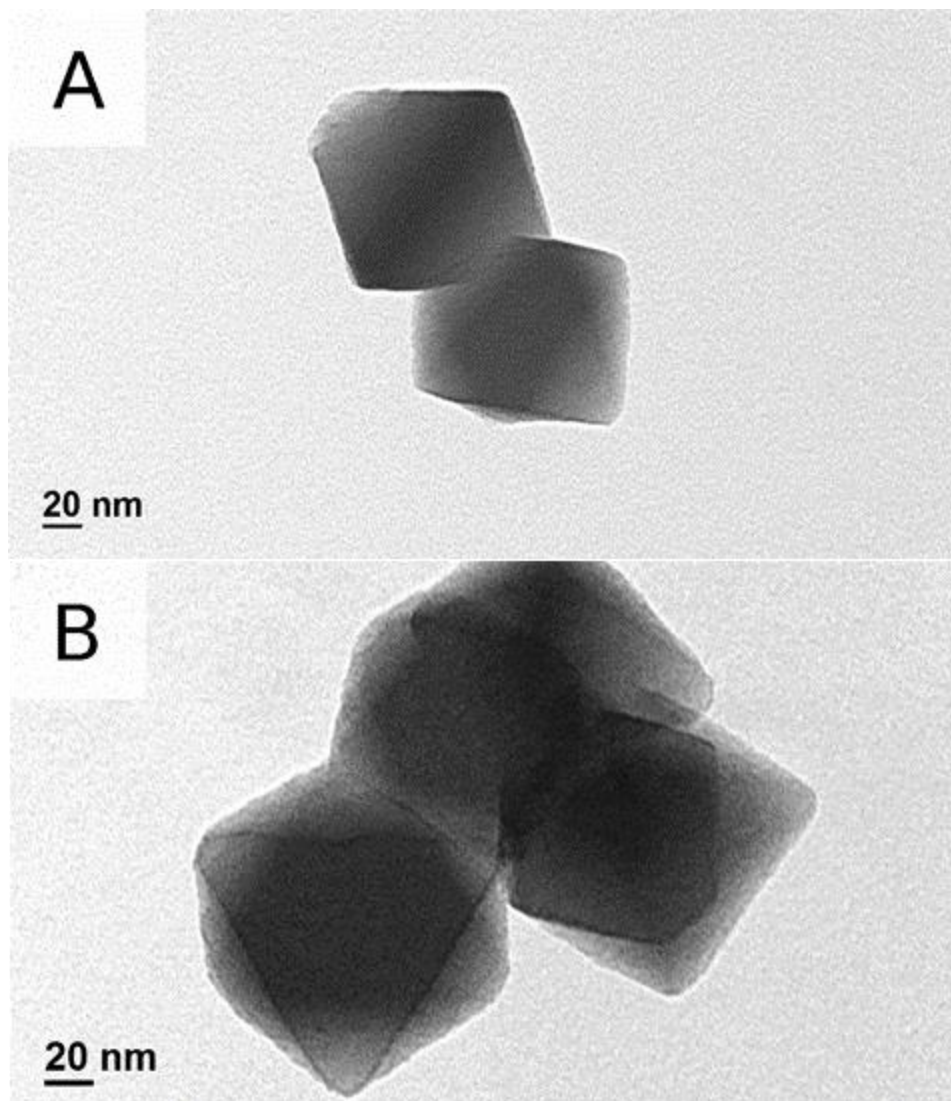


**Figure 46.** TEM of UiO-66-NH<sub>2</sub> (A) and 5% HPW UiO-66-NH<sub>2</sub>.

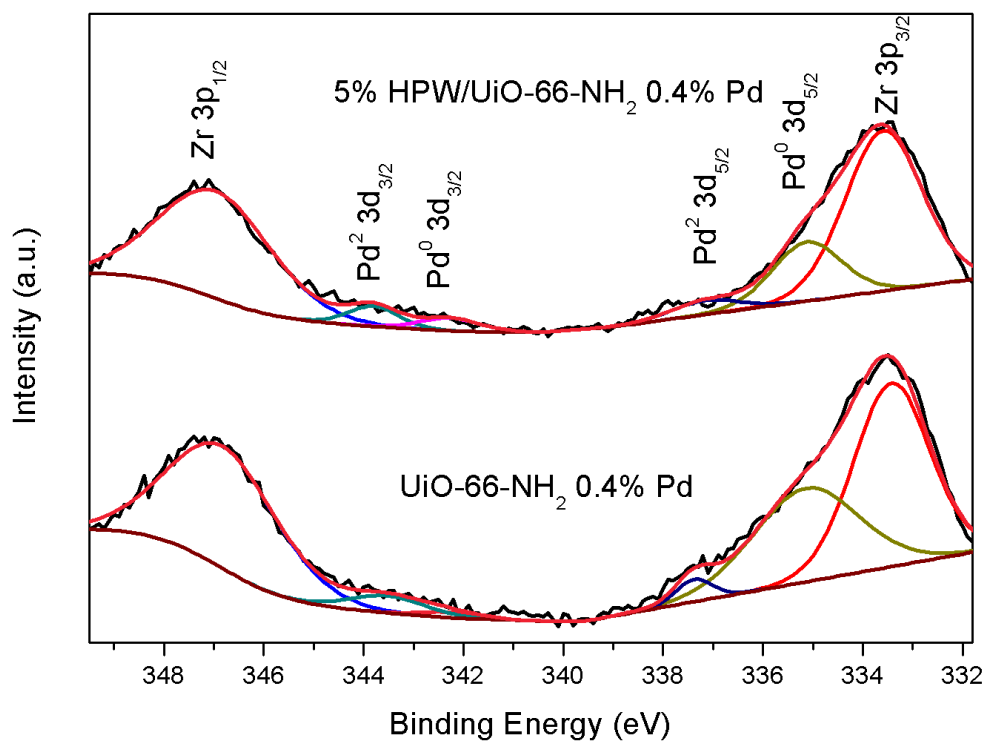


**Figure 47.** Pd 3d XPS spectra for palladium nanoparticles supported on UiO-66-NH<sub>2</sub> and 5% HPW UiO-66-NH<sub>2</sub>.

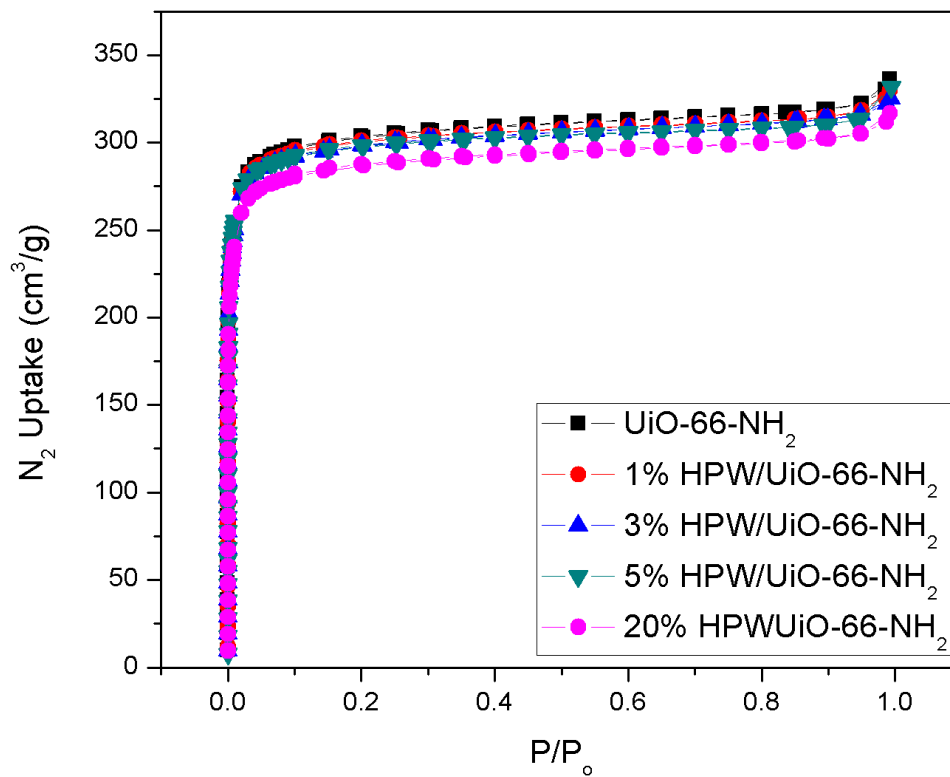


**Figure 48.** BET adsorption and desorption profiles of the 0-20 wt% HPW/UiO-66-NH<sub>2</sub> supports without palladium nanoparticles.

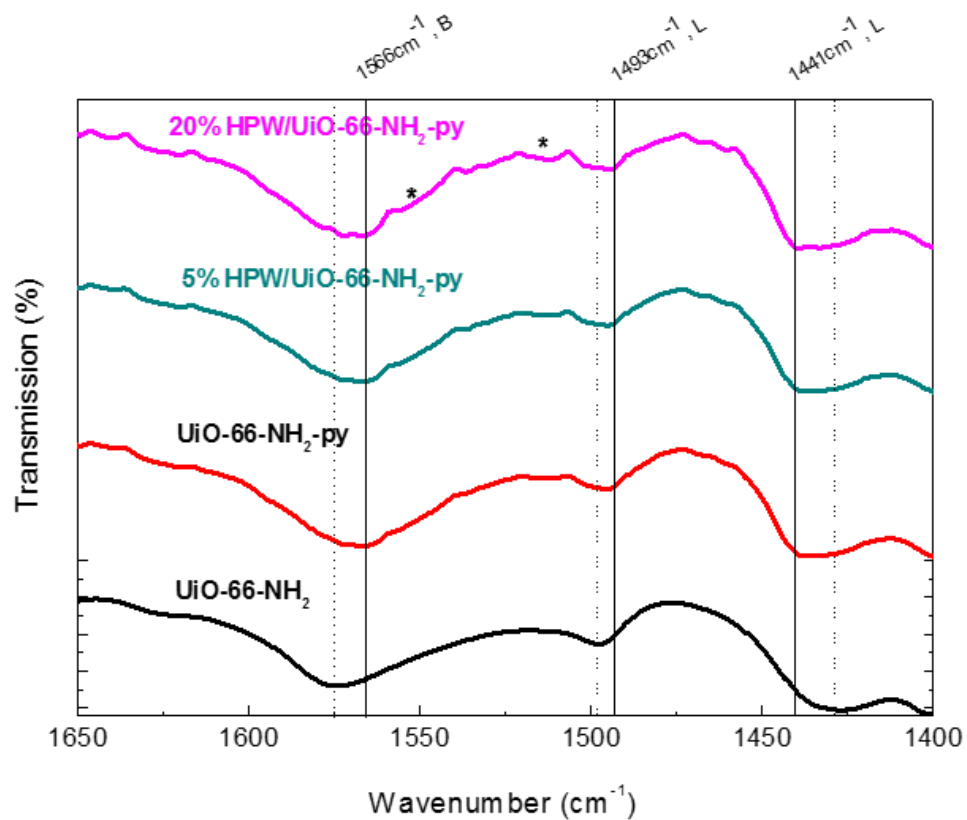


**Figure 49.** FT-IR spectra of pyridine adsorption into UiO-66-NH<sub>2</sub> with and without HPW loading.

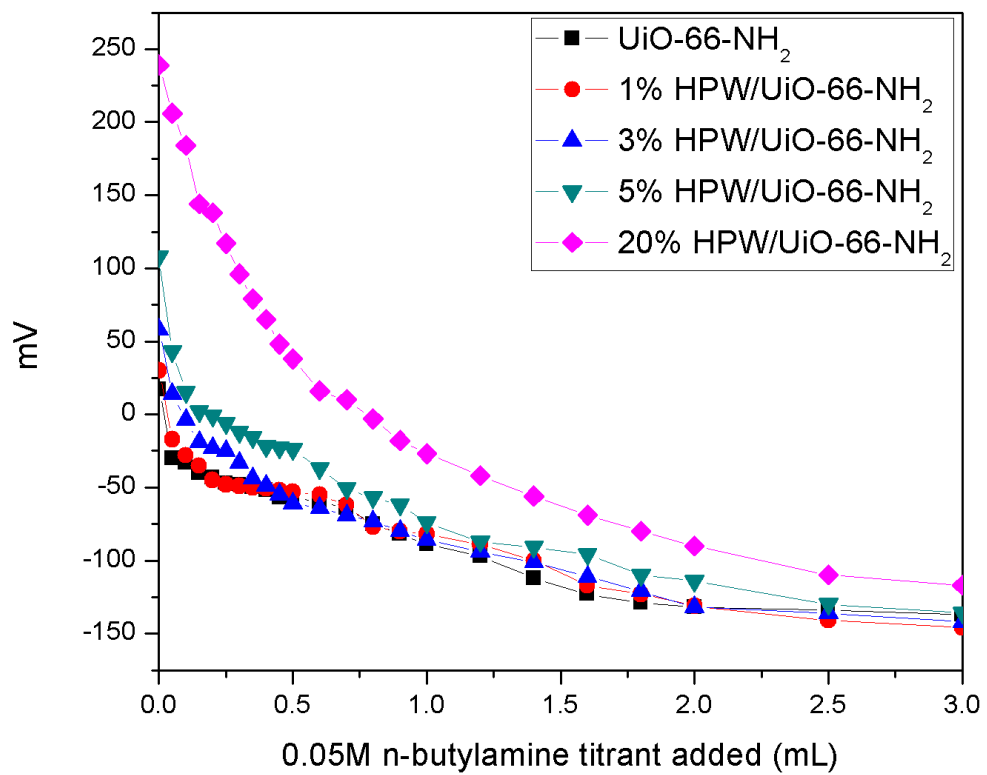


**Figure 50.** Potentiometric n-butylamine titration of 0-20 wt% HPW/UiO-66-NH<sub>2</sub> supports.



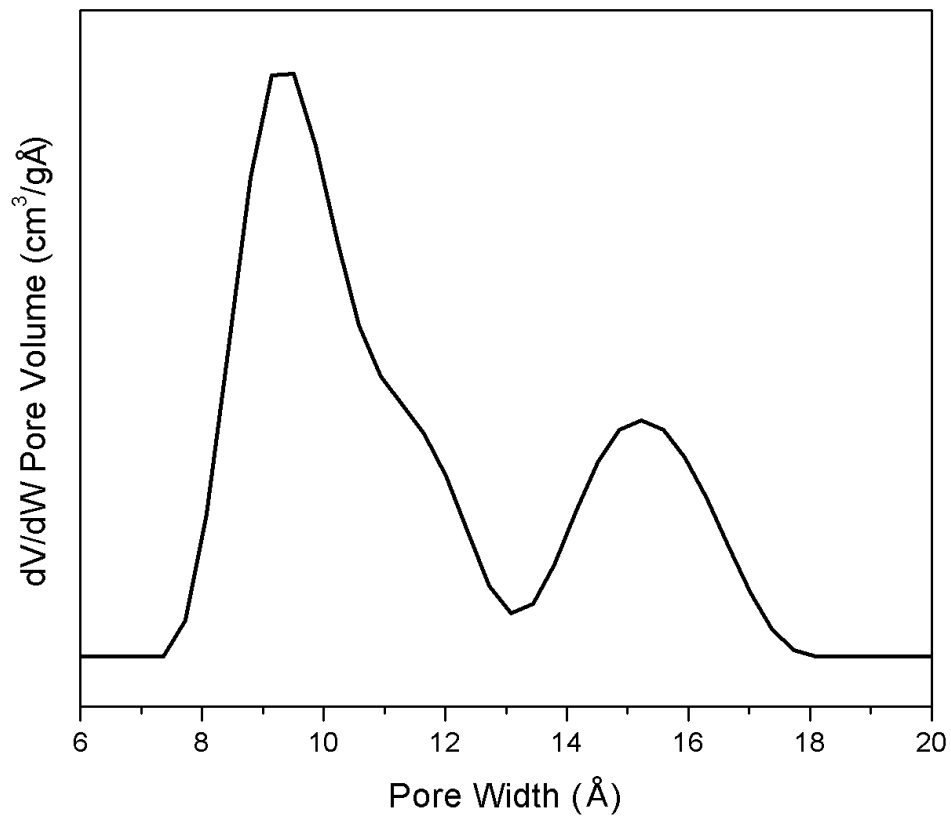


**Figure 51.** Pore size distribution of UiO-66-NH<sub>2</sub>.

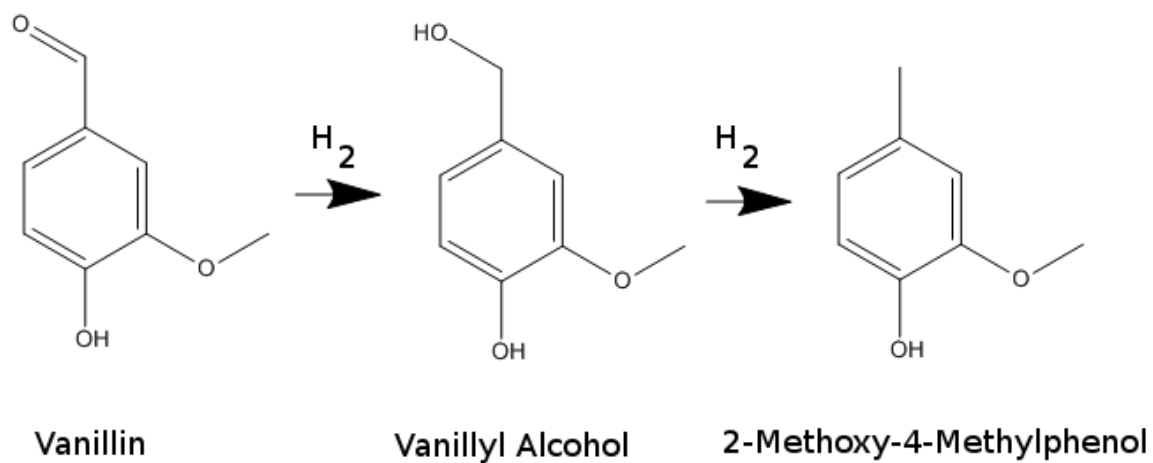


**Figure 52.** Two-step hydrogenation of vanillin into 2-methoxy-4-methylphenol. Reaction conditions: 300 mg vanillin (2 mmol) in 20 mL of DI water with 50 mg of catalyst (1:200 palladium catalyst:substrate ratio). 1 mPa H<sub>2</sub> gas, 100 °C, 960 rpm.

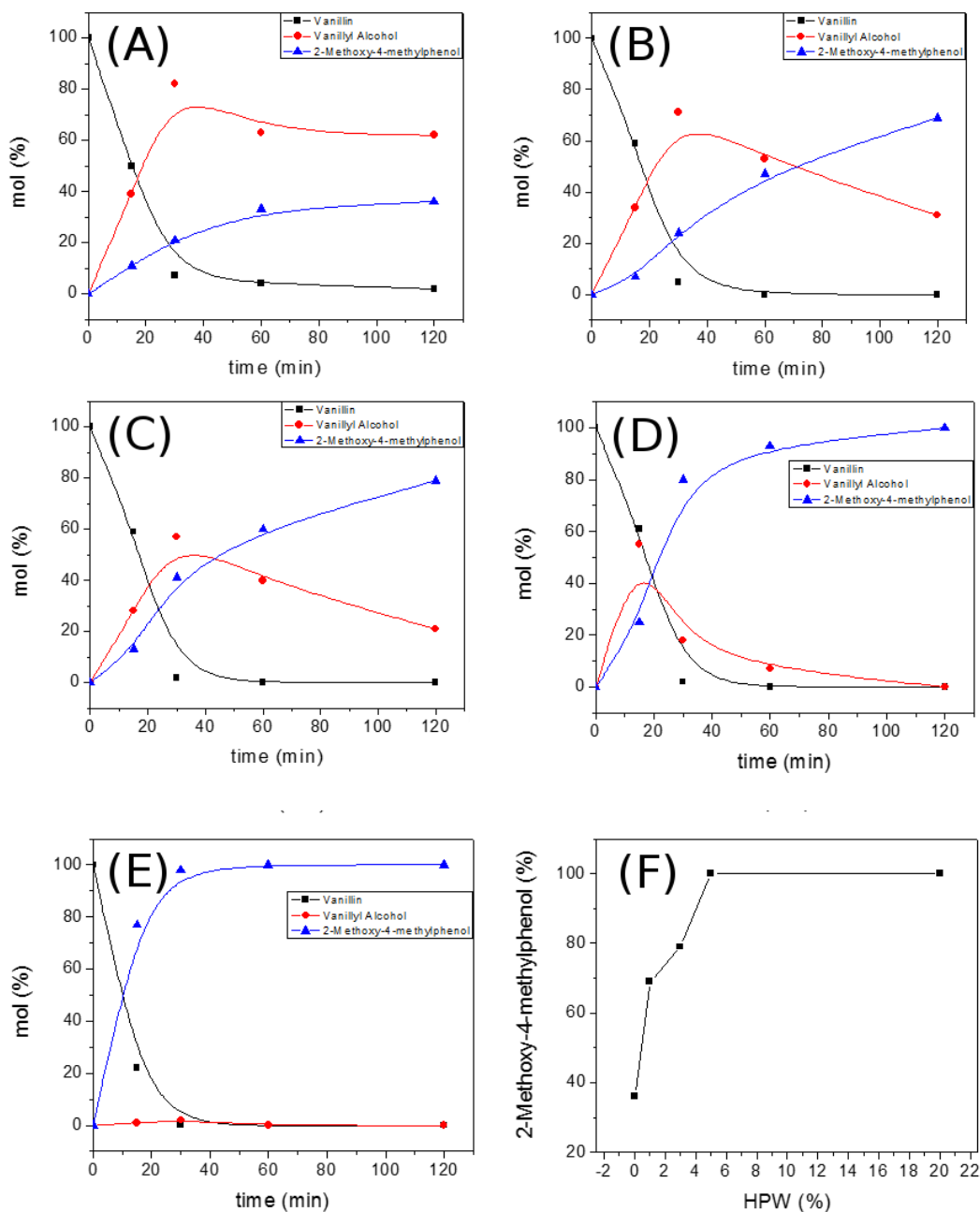


**Figure 53.** Vanillin hydrogenation activity as a function of time for palladium catalyst supported on UiO-66-NH<sub>2</sub> (A), 1% HPW/UiO-66-NH<sub>2</sub> (B), 3% HPW/UiO-66-NH<sub>2</sub> (C), 5% HPW/UiO-66-NH<sub>2</sub> (D), 20% HPW/UiO-66-NH<sub>2</sub> (E), and 2-methoxy-4-methylphenol mol% as a function of 0-20 wt% HPW by 60 min.

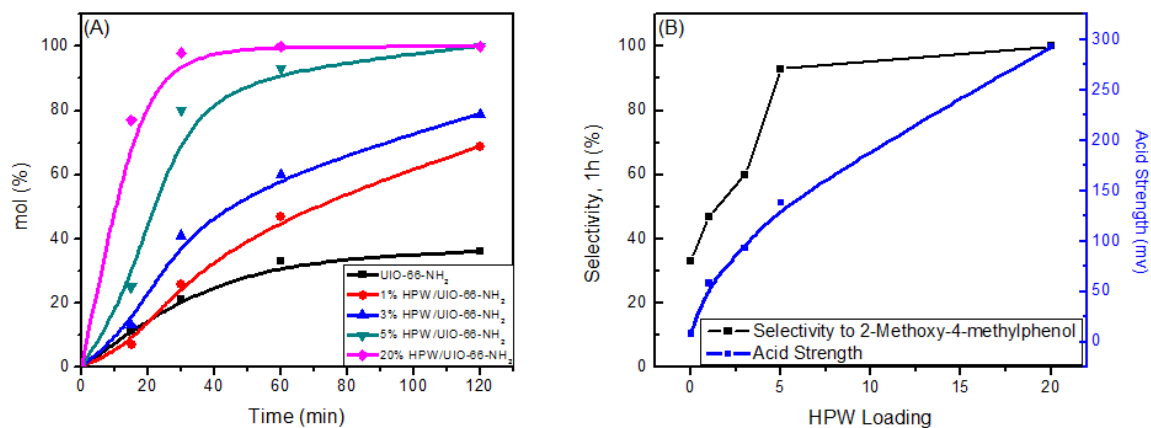


**Figure 54.** Mol% of 2-Methoxy-4-methylphenol as a function of time with 0-20% HPW loading (A) and 2-Methoxy-4-Methylphenol selectivity as a function of acidity (B) at the 60 minute interval for UiO-66-NH<sub>2</sub> 0.4% Pd with 0-20% HPW loading.

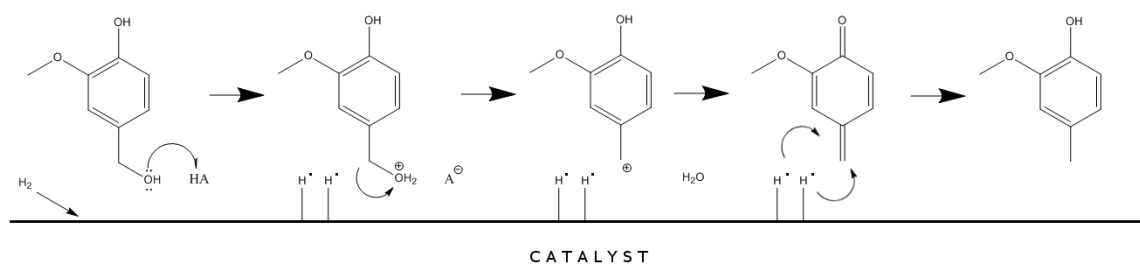


**Figure 55.** Proposed dehydration-hydrogenation mechanism of vanillyl alcohol into 2-methoxy-4-methylphenol.

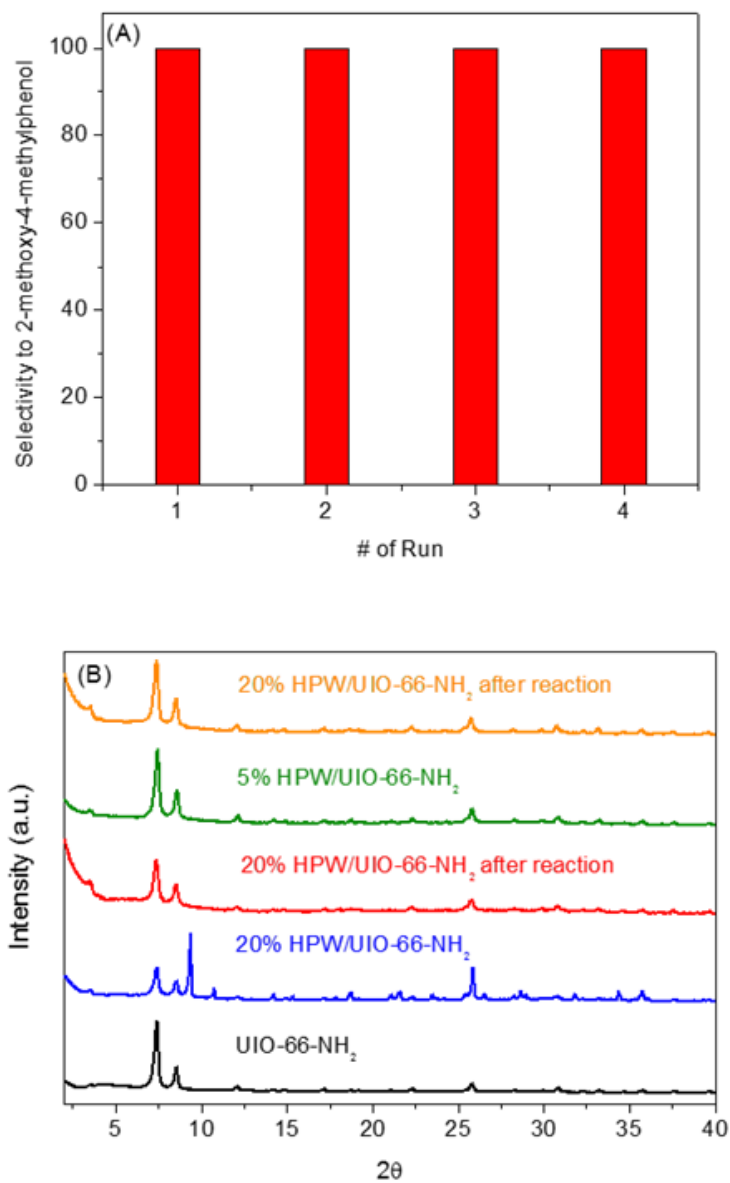


**Figure 56.** 5% HPW/UiO-66-NH<sub>2</sub> 0.4% Pd selectivity over 4 repeated runs (A) and XRD diffractogram of HPW/UiO-66-NH<sub>2</sub> 0.4% Pd catalysts before and after recycling.

**Table 6.** Palladium oxidation state calculated from Pd 3d XPS analysis of supports with and without HPW loading.

---

**UiO-66-NH<sub>2</sub> 0.4% Pd**

| <b>Oxidation State</b> | <b>FWHM (ev)</b> | <b>Atomic (%)</b> |
|------------------------|------------------|-------------------|
| Pd (0)                 | 335.2            | 96.6              |
| Pd (II)                | 337.0            | 3.4               |

**5% HPW/UiO-66-NH<sub>2</sub> 0.4% Pd**

| <b>Oxidation State</b> | <b>Oxidation State</b> |      |
|------------------------|------------------------|------|
| Pd (0)                 | 335.1                  | 88.1 |
| Pd (II)                | 337.4                  | 11.9 |

---

**Table 7.** BET surface area measurements of 0-20 wt% HPW/UiO-66-NH<sub>2</sub> supports without palladium nanoparticles.

---

| <b>Sample</b>                  | <b>BET Surface Area (m<sup>2</sup>/g)</b> |
|--------------------------------|---|
| UiO-66-NH <sub>2</sub>         | 1225                                      |
| 1% HPW/UiO-66-NH <sub>2</sub>  | 1220                                      |
| 3% HPW/UiO-66-NH <sub>2</sub>  | 1218                                      |
| 5% HPW/UiO-66-NH <sub>2</sub>  | 1206                                      |
| 20% HPW/UiO-66-NH <sub>2</sub> | 1173                                      |

---



**Table 8.** Acid strength and acidity of 0-20 wt% HPW/UiO-66-NH<sub>2</sub>.

---

| <b>Catalyst</b>                | <b>Pd (%)</b> | <b>HPW (%)</b> | <b>E<sub>i</sub> (mV)</b> | <b>Acidity (mmol/g)</b> |
|--------------------------------|---------------|----------------|---------------------------|-------------------------|
| UiO-66-NH <sub>2</sub>         | 0.4           | -              | 17                        | 0.8075                  |
| 1% HPW/ UiO-66-NH <sub>2</sub> | 0.4           | 1              | 30                        | 0.8480                  |
| 3% HPW/UiO-66-NH <sub>2</sub>  | 0.4           | 3              | 58                        | 1.028                   |
| 5% HPW/UiO-66-NH <sub>2</sub>  | 0.4           | 5              | 108                       | 1.124                   |
| 20% HPW/UiO-66-NH <sub>2</sub> | 0.7           | 20             | 239                       | 2.384                   |

---

**Table 9.** Conversion of vanillin and vanillyl alcohol into products with a series of UiO-66-NH<sub>2</sub> supports with and without HPW and palladium nanoparticles.

---

|                                       | <b>Chemical Conversion (%)</b> |                  |
|---------------------------------------|--------------------------------|------------------|
|                                       | Vanillin                       | Vanillyl Alcohol |
| UiO-66-NH <sub>2</sub>                | -                              | -                |
| 5% HPW/UiO-66-NH <sub>2</sub>         | -                              | 9%               |
| 5% HPW/UiO-66-NH <sub>2</sub> 0.4% Pd | 100%                           | 100%             |

---

**Table 10.** Comparison of TOF based of off palladium content in comparison to recent works.

| Sample                         | Catalyst | S/C Ratio | Temp. (°C) | Pressure (MPa) | Conv 30 min (%) | 2-methoxy-4-methylphenol %mol composition, 30 min (%) | TOF (h <sup>-1</sup> ) | Ref.      |
|--------------------------------|----------|-----------|------------|----------------|-----------------|---|------------------------|-----------|
| UiO-66-NH <sub>2</sub>         | 0.4% Pd  | 1050      | 100        | 1              | 93              | 21  | 440                    | This work |
| UiO-66-NH <sub>2</sub>         | 0.4% Pd  | 1050      | 100        | 1              | 98              | 80  | 1670                   | This work |
|                                | 5% HPW   |           |            |                |                 |   |                        | work      |
| UiO-66-NH <sub>2</sub>         | 0.7% Pd  | 650       | 100        | 1              | 100             | 98  | 1170                   | This work |
|                                | 20% HPW  |           |            |                |                 |   |                        | work      |
| UiO-66-NH <sub>2</sub>         | 2% Pd    | 200       | 90         | 0.5            | 100             | 81  | 340                    | [155]     |
| MIL-101 (Cr)-SO <sub>3</sub> H | 2% Pd    | 200       | 80         | 0.5            | 53              | 39  | 160                    | [141]     |
| TiO <sub>2</sub> @N-C          | 2.1% Pd  | 83        | 150        | 0.5            | 22              | 2   | 4                      | [183]     |
| CNT                            | 1.2% Ru  | 135       | 150        | 1              | 43              | 24  | 61                     | [184]     |
| Carbon                         | 2% Pd    | 200       | 90         | 0.3            | 78              | 9   | 36                     | [142]     |
| <b>Microspheres</b>            |          |           |            |                |                 |   |                        |           |
| N-doped Carbon                 | 10% Pd   | 350       | 90         | 1              | 62 (60 min)     | 42 (60 min)   | 146                    | [143]     |
| Carbon                         | 5% Pd    | 306       | 70         | 1              | 40              | 18  | 110                    | [185]     |
| <b>Nitride-CT</b>              |          |           |            |                |                 |   |                        |           |
| Carbon                         | 5% Pd    | 306       | 70         | 1              | 64              | 45  | 280                    | [185]     |
| <b>Nitride-CF</b>              |          |           |            |                |                 |   |                        |           |
| Carbon                         | 5% Pd    | 306       | 70         | 1              | 47              | 23  | 140                    | [185]     |
| <b>Nitride-CE</b>              |          |           |            |                |                 |   |                        |           |

## **Chapter 6: Partial Functionalization of Graphene Oxide with p-Phenylenediamine and Benzidine as Novel Supports for Palladium Nanoparticle Catalysts for Room Temperature Suzuki Cross Coupling Reactions**

### **6.1 Introduction**

The Suzuki cross coupling reaction is an important organic reaction for pharmaceutical industries whereby aryl halide derivatives are coupled to organoboronics in the presence of Pd(0) catalysts, resulting in desirable substituted biphenyls. Rational catalyst synthesis for this reaction is typically employed to design supports that promote the activity of supported Pd(0) nanoparticles. Typical Suzuki cross coupling reactions occur at higher temperatures (40-80 °C) or under microwave conditions.

GO is one of the more widely used supports for palladium nanoparticles for this reaction because it is an excellent charge donor and acceptor.[186] Modification of GO can affect the electronic properties, which would alter the catalyst-support interaction between GO and nanoparticles. One method for the reduction of graphene oxide is functionalization with aromatic amine molecules, such as phenylenediamine (PPD) and benzidine (BZD).[187-189] Such routes have been reported for the functionalization of GO with these intercalating agents, but the general application is in an electrochemistry context, such as high-capacity supercapacitors,[190-192] electrode materials,[193] or catalysts for oxygen reduction reactions.[194] For these applications, an excess amount of aromatic amines is added to fully reduce the GO. All oxygen-containing groups are expunged to improve GO's capabilities as an electrocatalyst.

Partial functionalization of this material has not been thoroughly investigated. Here, the effects of partial functionalization of graphene oxide by BZD and PPD was studied as a function of intercalant molecule concentration. Benzidine and p-phenylenediamine are known to be strong

reducing agents for graphene oxide capable of removing epoxy and alcohol groups. Partial functionalization of GO for the inclusion of nitrogen-bearing bulky aromatic groups implies partial reduction. The remnant oxygen groups, such as epoxies, alcohols, and carboxylic acids, can be exploited. These two compounds are diamine molecules with either one or two phenyl groups, as seen in Figure 57.[195] These compounds have previously been reported to reduce and/or functionalize GO by intercalative grafting or by nucleophilic substitution of present oxygen groups with the amine moieties.[187-188, 196]

Past works have described the co-reduction of graphene oxide and nanoparticles, where nanoparticles settle the generated defect sites on the GO during reduction.[119] Furthermore, the presence of oxygen groups on the surface of the GO permits the strong electrostatic adsorption (SEA) of cationic palladium salts. This technique can be implemented to allow adsorption of  $\text{Pd}^{2+}$  to the surface of GO prior to microwave irradiation (MWI) reduction in the presence of hydrazine hydrate (HH).[197] The fundamental theory of SEA is that the hydroxyl groups on GO can be protonated and deprotonated relative to its point of zero charge (PZC);[198] doing so allows the surface to be positively or negatively charged, which increases adsorption of either cationic or anionic salts. The loading of nanoparticles on carbon-based supports by the SEA method has been studied extensively,[198-199] but GO enhanced with aromatic amine groups is expected to be more catalytically active than GO alone. Not only is it expected to be more catalytically active due to the presence of amines that coordinate and reduce palladium salts, but the co-reduction of the GO and  $\text{Pd}^{2+}$  is also expected to generate smaller nanoparticles. This is because of the close proximity of adsorbed palladium ions to generated defect sites.

## 6.2 Strong Electrostatic Adsorption (SEA)

Cationic palladium salt  $[(\text{Pd}(\text{NH}_3)_4)]^{2+}$  was adsorbed onto the surface of GO prior to reduction by MWI in the presence of HH using the strong electrostatic adsorption technique.[197] The basis of SEA theory is that an aqueous solution can act as either a base or an acid to the surface of an oxygen-laden material such as metal oxide or GO and can induce a partial positive or partial negative charge on the surface of such materials, according to the PZC of a material. The PZC is the pH at which the surface charge of the material is at equilibrium with the aqueous solution, and a neutral charge exists on the surface of the material.[200-202] Here, the pH of the GO material is adjusted to pH 10 prior to reduction, which exceeds the PZC of GO (GO PZC is pH 3.3-3.8).[203] In this case, aqueous solution acts as a base relative to the surface of the GO. More hydroxide interactions than proton interactions occur from the aqueous solvent, leading to oxygen groups with a partial negative charge.[198] As a result, the uptake of cationic  $[(\text{Pd}(\text{NH}_3)_4)]^{2+}$  is enhanced.

This technique of adsorption prior to reduction is imperative to this work. A higher uptake of palladium via adsorption to oxygen groups would result in smaller nanoparticles after reduction. The functionalization of GO with PPD and BZD molecules will be shown to affect the availability of oxygen groups, which affect the uptake of palladium nanoparticles.

## 6.3 Characterization

Figure 58 shows the XRD patterns of the GO after functionalization with PPD and BZD. The  $d_{001}$  peak shifts as a function of aromatic amine concentration. The  $d_{001}$  peak typically represents d-spacing in graphitic materials. The XRD peak shifts as a function of aromatic amine intercalant concentration with respect to the initial GO peak of  $11.3^\circ$ . It is well known that GO has an XRD  $d_{001}$  peak at  $11.3^\circ$  (d-spacing = 0.78 nm), which is indicative of distance between

graphitic layers.[127] It is observed that the inclusion of a small amount (0.025 mmol) of benzidine or p-phenylenediamine leads to an atypical right-shift of the XRD peak. Figure 58B shows that the presence of a small amount of BZD (0.025 mmol) shifts the GO  $d_{001}$  peak from  $11.3^\circ$  to  $13.3^\circ$ , decreasing the d-spacing from 0.78 nm to 0.66 nm. The  $d_{001}$  peak then upshifts to  $6.2^\circ$  (d-spacing = 1.4 nm), indicating an increase in interlayer distance in proportion to the further addition of BZD, up to a concentration of 0.5 mmol. This result is in agreement with previous characterization of GO saturated with aromatic amines.[188] When GO is functionalized with PPD (Figure 58A), an identical trend for the XRD peak shift is observed with respect to the initial  $11.3^\circ$   $d_{001}$  peak for GO. The GO  $d_{001}$  peak right-shifts from  $11.3^\circ$  to  $13.1^\circ$  (d-spacing = 0.68 nm) with the inclusion of 0.025 mmol PPD, followed by a gradual increase to  $9.7^\circ$  (d-spacing = 0.91 nm) and then to  $7.3^\circ$  (1.21 nm) when the concentration of PPD is increased to 0.5 mmol and then to 6.0 mmol. There are several reasons for this phenomena: first, the GO sheets restack due to a loss of oxygen groups,[204] and second, the GO is believed to be partially functionalized, and incomplete reduction results in non-uniform d-spacing.[205]

Figure 59 shows the FTIR spectrum of GO, followed by subsequent functionalization by either 0.1 mmol of benzidine or p-phenylenediamine. C=O bands are present at  $1725\text{ cm}^{-1}$ , C-O-C bands are present at  $1383\text{ cm}^{-1}$ , and C-O alkoxy bands are present at  $1060\text{ cm}^{-1}$  for GO. After functionalization by either BZD or PPD, the  $1725\text{ cm}^{-1}$  carbonyl band and the  $1060\text{ cm}^{-1}$  are retained, but slightly reduced in intensity, whereas the  $1383\text{ cm}^{-1}$  epoxy band disappears. The disappearance of the  $1383\text{ cm}^{-1}$  peak indicates removal of epoxy groups and partial reduction of the graphene oxide. A C=C shift from  $1630\text{ cm}^{-1}$  to  $1563\text{ cm}^{-1}$  is also observed with the introduction of either PPD or BZD aromatic amine functionalization agents.[206] The stretching vibration at  $1563\text{ cm}^{-1}$  is assigned to the formation of new C-N-C bonds,[207] which is a direct

consequence of inclusion of new nitrogen groups. Additionally, a large peak at  $1181\text{ cm}^{-1}$  for C-N stretching provides further evidence for reaction between the GO and the functionalization agents by way of a C-NH-C bond, which is possible with either PPD or BZD.[208] A small peak appears at  $820\text{ cm}^{-1}$  for C-NH<sub>2</sub> which is consistent with previous findings.[207-208]

Figure 60A and Figure 60B show the FTIR spectral peaks as a function of increased BZD/PPD content. In Figure 60B, the peaks at  $1181\text{ cm}^{-1}$  and  $820\text{ cm}^{-1}$  are greatly increased in intensity for the GO-BZD ( 0.5 ) sample relative to the GO-BZD ( 0.025 ) sample, indicating a greater degree of presence of the functionalization molecules. The detected FTIR peaks is in good accordance with Figure 2. The same trend is observed for the GO-PPD ( 6.0 ) sample: the  $1181\text{ cm}^{-1}$  and  $820\text{ cm}^{-1}$  peaks become sharper when an excess of PPD is reacted with GO (Figure 60A). The high absorbance indicates saturation of GO with aromatic amines.

The XPS peak fitting of C 1s and Pd 3d into individual components is performed in Figure 61. Figure 61A shows the survey of GO, GO-PPD ( 0.1 ), and GO-BZD ( 0.1 ); all samples are partially reduced and include palladium nanoparticles. It is evident from the survey scan of the series of samples that a peak for nitrogen, at approximately 398 eV, is absent for GO. A peak for oxygen (532 eV) encompasses 41.2% of area, which decreases to 32.0% and 32.8% after inclusion of p-phenylenediamine and benzidine, respectively. For GO-BZD ( 0.1 ) and GO-PPD ( 0.1 ) samples, the displacement of oxygen content is followed by the appearance of a small nitrogen peak at 398 eV. For all samples, the carbon XPS peak at 284 eV remain constant at 60%.

In Figure 61B, the fitted C 1s spectrum for GO as palladium nanoparticles post reduction in the presence of HH reduction agent shows  $sp^2$  hybridized C=C bonds (284.6 eV), C-O bonds (286.2 eV), and C=O bonds (288.8 eV). [209] After functionalization with PPD and BZD, the 286.2 eV C-O and O-C=O peak is severely diminished, and a new shoulder at 285.1 eV becomes



prominent after deconvolution for C-N bonding. [195] This offers further evidence of substitution of surface-bound oxygen groups with amine moieties. No change is expected for the C=C peak at 284.8 eV.

The oxidation state of palladium cycles between Pd(II) and Pd(0) in the palladium-catalyzed Suzuki cross coupling reaction between the oxidative addition and the reductive elimination steps.[210] Pd(0) is required to initiate oxidative addition step.[211-213] Hence, a higher ratio of Pd(0) would result in a higher rate of reaction.[214] The presence of amine functional groups on the GO support altered the Pd(0)% because diamine molecules such as phenylenediamine act as reducing agents.[215-216] The Pd 3d XPS spectra is shown Figure 5C. The Pd(0)% for GO, GO-PPD, and GO-BZD increases (27%, 31%, and 37%, respectively) as the aromatic bulk, or steric size, of the amine-bearing compound increases. The highest percentage Pd(0)% was found in samples after recycling due to the cycling of palladium between the oxidation states, as seen in Figure 62.

The size distributions of palladium nanoparticles is dictated in Table 11. The palladium nanoparticle sizes were determined through TEM micrographs (Figure 63). Palladium nanoparticles supported on GO were determined to be  $7.1 \pm 0.9$  nm. At low concentrations of PPD and BZD functional groups, the palladium size distribution decreased to  $2.9 \pm 0.7$  nm for GO-PPD ( 0.025 ) and  $2.2 \pm 1.1$  nm for GO-BZD ( 0.025 ). For the GO-BZD samples, it is seen that the palladium nanoparticle size begins to drastically increase as a function of higher BZD content. As BZD content increased from 0.025 mmol to 0.5 mmol, the palladium size increases gradually until a final palladium nanoparticle size of  $11.9 \pm 19.9$  nm is achieved. From Figure 63, the aggregation of palladium nanoparticles for GO-BZD ( 0.5 ) becomes highly evident.

#### 6.4 Effect of PPD/BZD Concentration of GO Interlayer Distance

In order for GO to adsorb cationic palladium via the strong electrostatic adsorption technique, the GO sample must have oxygen groups present. It is believed that the total exfoliation of GO layers with a saturating concentration of aromatic amine agents would lead to the blocking of defect sites by bulky groups and the removal of all of the oxygen groups due to reduction. However, if the GO is partially reduced with such aromatic amines, then a portion of the oxygen groups would be preserved. PPD is well-known as a reducing agent for GO capable of nucleophilic substitution removal of alcohol and epoxy groups. The removal of carboxylic acids is more difficult and requires basic conditions or an excess concentration of amines.[188] The removal of oxygen groups from the surface of GO by PPD or BZD results in the restacking of graphitic layers, and a decrease in the d-spacing is expected because oxygen-containing groups are directly responsible for the spacing of GO layers.[217] It was previously stated that the upward shift of the GO  $d_{001}$  peak from  $11.3^\circ$  to  $13.3^\circ$  (GO-BZD ( 0.025 )) or  $13.1^\circ$  (GO-PPD ( 0.025 )) was the result of incomplete functionalization. At lower concentrations of PPD or BZD, non-uniform d-spacing occurs. A decrease in d-spacing of 0.78 nm to 0.66 nm implies removal of oxygen group spacers without sufficient aromatic amine molecules to act as replacement scaffolding groups, which resulted in restacked graphitic layers.

Figure 64 graphically demonstrates this concept. Figure 64C illustrates the expected behavior of PPD molecules in a GO system where a critical mass of concentration isn't achieved to saturate the surface of GO. The insufficient quantity of bulky aromatic amine spacers to act a scaffolding to replace reduced oxygen groups leads to inconsistent or non-uniform spacing. This property resulted in the atypical upshift of the XRD  $d_{001}$  peak for samples with low concentrations of PPD or BZD. This phenomena has been previously been reported by computational studies,

and the irregular interlayer spacing is believed to be a result of disorderly bonding and inconsistent interlayer distance.[205] It has been previously calculated that 25 wt% of the PPD intercalant is needed to achieve an exfoliation of GO layers to 1.4 nm, which is in good alignment with our results. A non-optimal concentration of PPD would lead to an in-plane configuration of the molecules between the layers of GO, as illustrated in Figure 64C.[205]

Figure 64B illustrates functionalization of GO with an excess concentration of PPD, which act as replacement spacers after removal of oxygen groups. Since aromatic phenyls act as spacers after the amine groups attach to the surface via an  $S_N2$  mechanism with the removal of oxygen, it is expected that the d-spacing would increase due to the addition of bulky aromatic molecules.[218-219] It was confirmed by XRD diffraction analysis (Figure 58) that higher concentration of aromatic amine functional agents caused exfoliation of GO layers. This was evidenced by a downshift in the  $d_{001}$  peak.

The amine functional groups on either of PPD or BZD molecules allow for cross-linking between GO layers.[219] Cross-linkage is possible, but not expected for these samples. Cross-linkage requires an excess amount of aromatic amine molecules for both ends to interact with different layers of GO. With a low concentration of PPD, cross-linking is not expected. Instead, nucleophilic substitution attachment of a single amine renders the other amine group free to interact with palladium, which increases the catalyst-support interaction. Polymerization of BZD has also been reported, but this type of interaction between aromatic amines and GO are not expected for these catalysts for similar reasons.[218]

## 6.5 Effect of PPD/BZD Concentration on Palladium Uptake and Nanoparticle Size

The SEA technique was employed for the adsorption of cationic  $[(\text{Pd}(\text{NH}_3)_4)^{2+}]$  salt to the negatively charged surface of GO.[197] The partial negative charge on the surface of GO assists towards the adsorption or uptake of cationic salts prior to reduction.

Partial functionalization preserves a greater abundance of oxygen groups, whereas full reduction of GO eliminates the oxygen groups on the surface of GO. A higher degree of intact oxygen groups on the GO surface allows SEA uptake of cationic palladium salts, leading to smaller nanoparticle size because such functional groups act as nucleation sites. A higher content of oxygen groups entails more nucleation.[220] More cationic palladium ions is adsorbed onto the surface of GO due to higher oxygen availability, and nucleation of nanoparticles is favored due to higher uptake of ions. It is believed that the amines help coordinate or reduce palladium, leading to a higher percentage of Pd(0),[216] which is in good agreement with XPS analysis. Table 1 shows a decrease in actual Pd% loading as the GO is reduced by higher BZD concentrations. Oxygen groups are fully substituted by amine moieties. The GO-BZD ( 0.025 ) sample had a palladium uptake of 3.3%, as determined from ICP. With additional functionalization, GO-BZD ( 0.5 ) had only a palladium uptake of 2.2%.

A lower oxygen availability on GO due to the presence of higher BZD loading would corroborate SEA theory: less palladium nanoparticles are electrostatically adsorbed onto GO via attraction of cationic salts to  $\text{O}^-$  groups. Less nucleation and more growth is favored at higher concentrations of aromatic amine functionalization. When more aromatic amines is functionalized to the surface of GO, less oxygen groups remain due to a greater degree of reduction. When this occurs, less interaction with cationic palladium decreases the amount adsorbed to the surface of the GO, which causes the few palladium seeds that nucleate to grow via aggregation into large

particles. When less aromatic amines is present, the GO is reduced to a lesser extent and the higher degree of oxygen allows for the attraction of cationic palladium at more sites, which allows for nucleation of more particles. The nanoparticles is well dispersed and have a smaller size. The TEM images exhibit aggressive agglomeration of nanoparticles for the GO-BZD ( 0.5 ) sample.

## 6.6 Effect of PPD/BZD Funtionalization of Suzuki Cross Coupling Activity

Figure 65 shows the conversion of bromobenzene and phenylboronic acid into biphenyl at room temperature. GO, GO-PPD ( 0.1 ), and GO-BZD ( 0.1 ) have a similar 3% palladium loading, but a trend is visible in terms of conversion of reactants into biphenyl: GO-BZD ( 0.1 ) > GO-PPD ( 0.1 ) > GO. GO-BZD ( 0.1 ) achieved 84% conversion by 15 min while GO-PPD ( 0.1 ) and GO lags behind with 18% and 17% conversion respectively. By 30 min, GO-BZD ( 0.1 ) has effectively attained full (98%) conversion, where GO-PPD ( 0.1 ) is at 64%, and GO is at 38%. In addition to coordinating palladium nanoparticles, the presence of amines is believed to assist in the reduction of palladium salts into nanoparticle. It was discussed in the XPS analysis (Figure 61C) that a higher Pd(0)% was seen for GO-BZD (37%) compared to GO-PPD (31%) and GO (27%). The coupling of aryl halides and phenylboronic acid into biphenyls was expected to be highest for GO-BZD ( 0.1 ) due to the higher Pd(0)%.

The relatively worse activity of the non-functionalized GO is expected. GO is established as one of the best supports for Pd(0) nanoparticles for the catalytic conversion of aryl halides and boronic acids into desired substituted biphenyls. GO is theoretically an efficient charge donor and acceptor and helps to activate the oxidation and reduction steps in palladium-catalyzed Suzuki cross coupling reactions.[186] However, harsher conditions are usually required. Typical Suzuki cross coupling reactions occur at higher temperatures (40-80 °C)[221] or under microwave conditions.[222-224] 0.3 mol% Pd supported on GO has previously been reported to take hours

under mild room temperature conditions.[119] The expedited conversion induced by partial amine functionalization of GO is expected to occur because amines such as phenylenediamine can reduce palladium to a higher Pd(0)%.[215] The reaction proceeds at a much faster rate because Pd(0) is critical for the Suzuki cross coupling reaction.

### **6.7 Effect of PPD/BZD Concentration on Suzuki Cross Coupling Activity**

A comparison of catalytic activity as a function of intercalant molecule concentration exhibited a rapid drop in the activity as the BZD or PPD content was increased. Figure 66B shows the effect of 0.025-0.5 mmol BZD concentration on GO. The sample with the minimal concentration of BZD, GO-BZD ( 0.025 ), was able to achieve over 90% conversion within 15 min. For GO-BZD ( 0.025 ), GO-BZD ( 0.2 ), and GO-BZD ( 0.5 ) samples, the biphenyl coupling conversion attained at 15 min were 82%, 21%, and 3%, respectively. GO-BZD ( 0.2 ) (21% conversion) had similar activity to non-functionalized GO, which had achieved 17% conversion by 15 min, and GO-BZD ( 0.5 ) had inferior activity to non-functionalized GO.

The drop in activity is inversely correlated to the size of the palladium nanoparticle size distribution. As the oxygen content on GO is displaced by the nucleophilic substitution of bulky aromatic amine groups, there is less oxygen for the strong electrostatic adsorption of cationic palladium, leading to fewer seeds and more aggregation of nanoparticles during reduction. This is suspected to be due to the lack of accessibility to defect sites generated on the graphene oxide as well, from blockage of the interlayers by the steric bulk of large aromatic amine molecules. The d-spacing plays an integral role in palladium's loss of accessibility to defect sites.

The nanoparticle size distribution, XRD  $d_{001}$  peak, and d-spacing of the GO, GO-PPD, and GO-BZD samples are summarized in Table 11. The smallest nanoparticle size distributions were

observed for GO-PPD ( 0.025 ) and GO-BZD ( 0.025 ). As previously stated, an increase in the concentration of BZD increased the particle size.

It was proposed that the aromatic amine functionalization of GO could tune the palladium nanoparticle size, which would in turn affect the catalytic activity of the material. It was demonstrated that GO-BZD ( 0.2 ) had similar activity compared to non-functionalized GO; Table 11 indicates that the particle size distribution between these two samples is similar, and this concentration of BZD served as the tipping point in correlating activity to both nanoparticle size and d-spacing. GO-BZD ( 0.2 ) had a palladium nanoparticle size distribution of  $7.5 \pm 3.2$  nm, which is similar to the size distribution of  $7.1 \pm 5.0$  nm for palladium nanoparticles supported on GO. When fully saturated with BZD intercalant molecules, GO-BZD ( 0.5 ) had a  $d_{001}$  peak at  $6.3^\circ$  (d-spacing = 1.41 nm) with a palladium nanoparticle size distribution of  $11.9 \pm 19.9$  nm. Full functionalization of GO caused full exfoliation of layers with spacer molecules, but activity is severely diminished because of the lack of palladium nucleation sites and absence of oxygen groups for the strong electrostatic adsorption of cationic palladium salts. This is further evidenced by the decrease in actual Pd wt% to 2.2% for the most saturated GO-BZD ( 0.5 ) sample.

It is proposed that the ultimate effect of functionalizing GO with amine-bearing PPD and BZD groups was the partial reduction/functionalization of GO, which allowed for smaller nanoparticles to form on defect sites. It is believed that the functionalized amines allowed for greater strong electrostatic adsorption of a cationic precursor, as these results could not be reproduced with palladium nitrate.

The Suzuki cross coupling activity for GO-BZD ( 0.1 ) as a function of palladium wt% is shown in Figure 67. It can be seen that a similar activity is observed for 1-5 Pd wt%. All samples had full conversion of reactants into biphenyl within 30-45 m, with 3% being optimal. The activity

of the samples comes from the strong catalyst-support interaction induced by the functionalization of graphene oxide with aromatic amine intercalants because even a minimal amount of Pd wt% is capable of coupling bromobenzene and phenylboronic acid into biphenyl.

The turnover frequency (TOF) was calculated based off of mol% of palladium relative to limiting reagent 0.32 mmol bromobenzene. Table 11 shows the calculated TOF values for each sample. GO-PPD ( 0.025 ) (TOF = 1740h<sup>-1</sup>) and GO-BZD ( 0.025 ) (TOF = 1230h<sup>-1</sup>) have significantly higher TOF values than GO (TOF = 182), which is reflective of the catalytic efficiency in the palladium-catalyzed Suzuki cross coupling reaction. The TOF for GO-BZD decreases as a function of concentration because of the decrease of reaction rates, for reasons previously discussed.

The TOF of these samples is compared to recent carbonaceous supports for palladium as catalysts for Suzuki cross coupling in Table 12. Table 12 also lists the reaction conditions of each sample. The TOF of all samples were calculated using mol% of palladium with respect to concentrations of limiting reagent reported. The TOF numbers of these partially amine-functionalized GO supports is vastly improved over most supports. It can be seen that most reactions required several hours, where the reaction is finished in 15 using 3 wt% Pd supported on GO-PPD ( 0.025 ) and GO-BZD ( 0.025 ).

### **6.8 Recycling of 3% Pd/GO-BZD ( 0.1 ) and ICP Analysis for Leaching**

The catalyst was recycled under microwave reaction conditions for Suzuki cross coupling reaction with ICP measurements between recycling runs to determine the extent of palladium leaching during the experiment. A microwave reaction was used to observe if palladium leaching would occur under harsher conditions. A total of 6 trials were performed with recovered samples, which were washed with hexane and ethanol, followed by overnight drying. Table 13 shows the



catalytic activity of catalysts as a function of repeated trials. A drop in activity was observed only after four runs under vigorous microwave conditions. Leaching of palladium nanoparticles did occur, but was minimal and restricted primarily to the first run, where loosely attached particles were washed out.

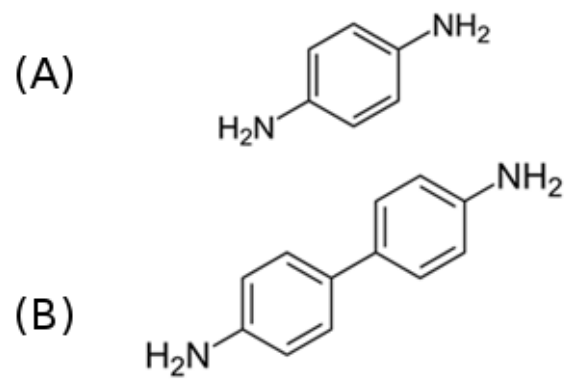


**Figure 57.** Structure of PPD (A) and BZD (B).

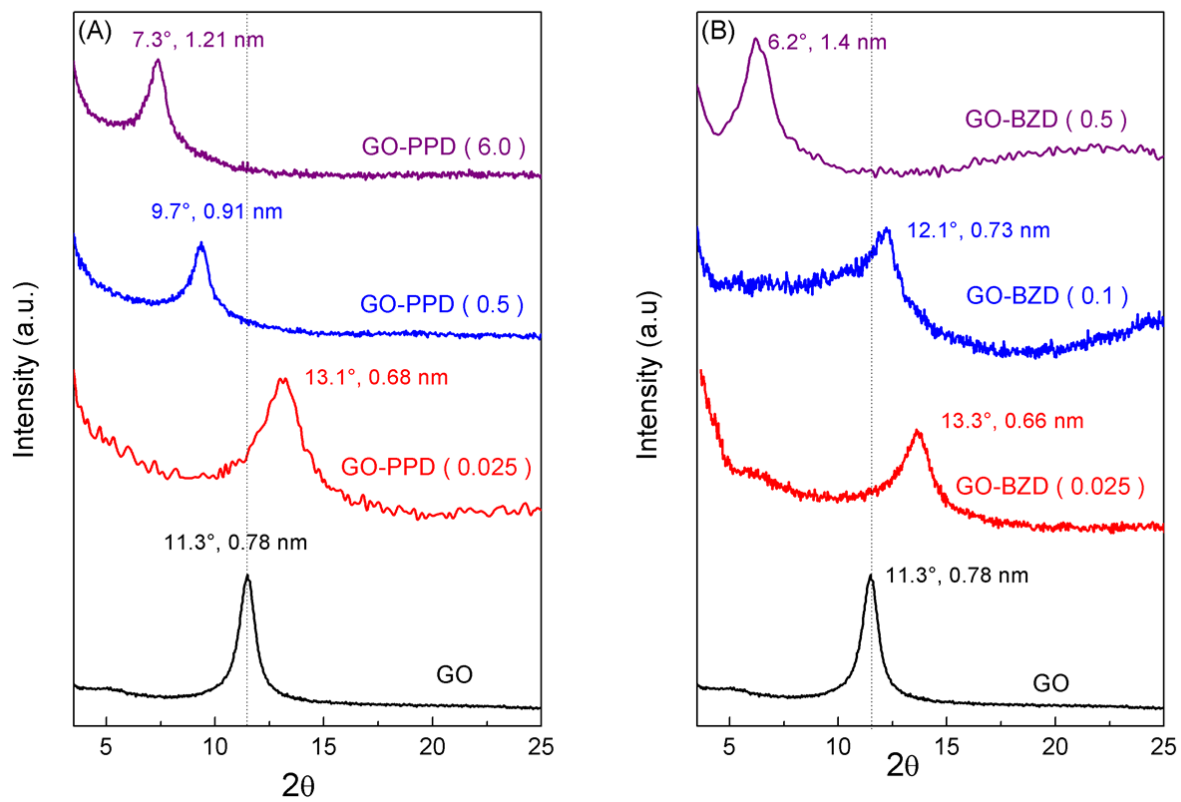


**Figure 58.** XRD of GO functionalized with PPD (A) and BZD (B) as an effect of concentration.

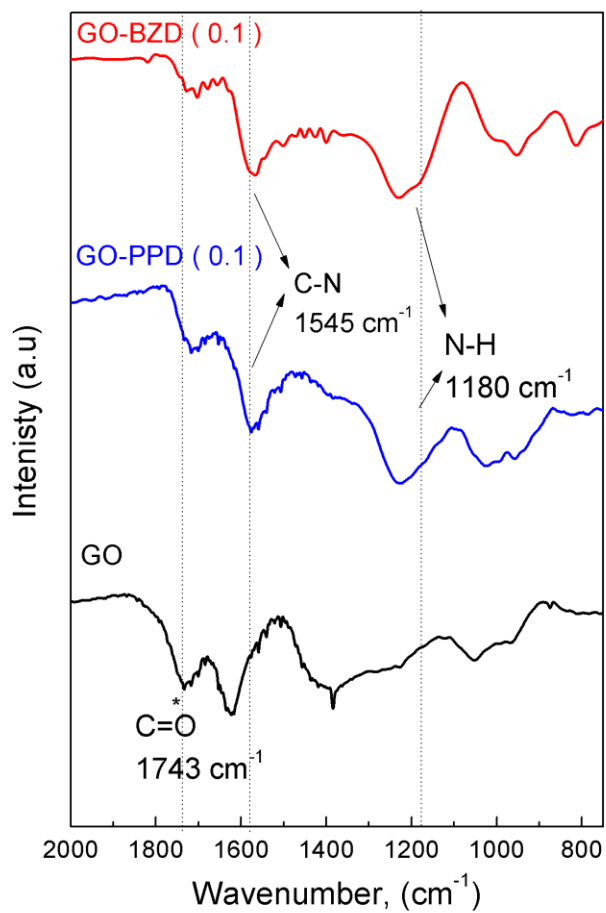


**Figure 59.** FTIR spectra for GO, GO-BZD, and GO-PPD

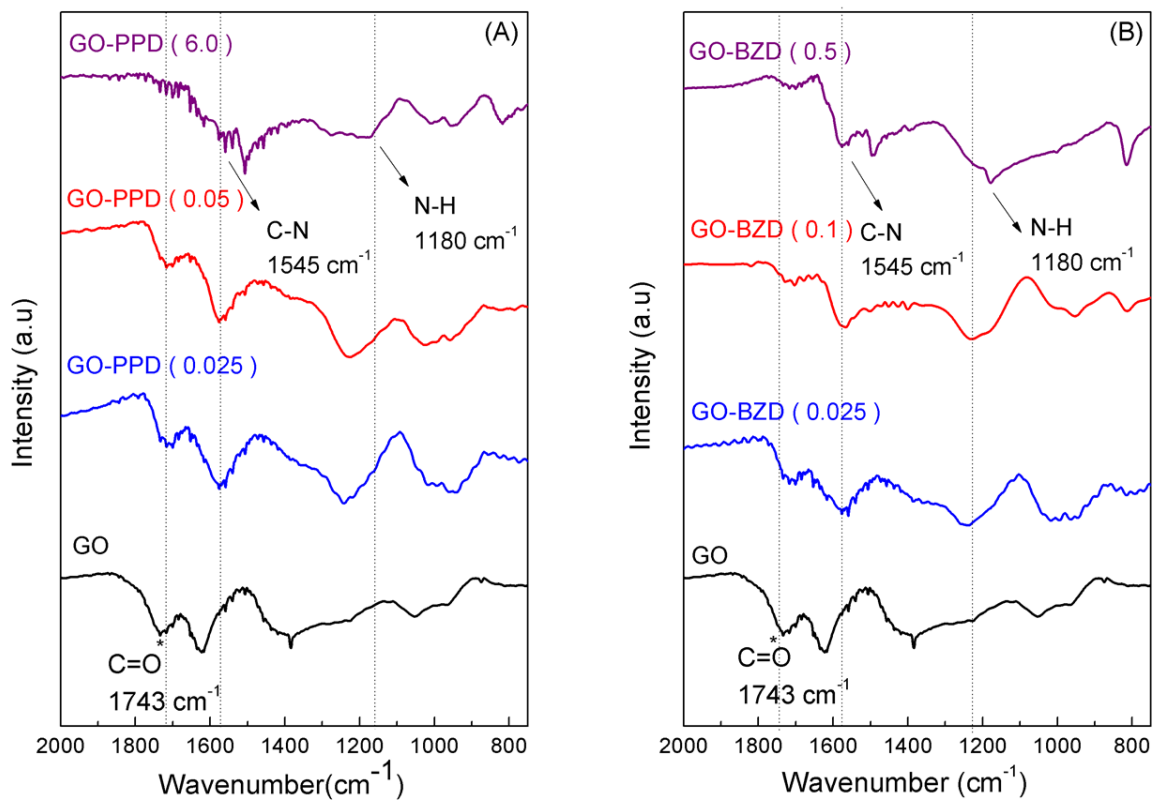


**Figure 60.** FTIR spectra as a function of PPD concentration (A), and as a function of BZD concentration (B).

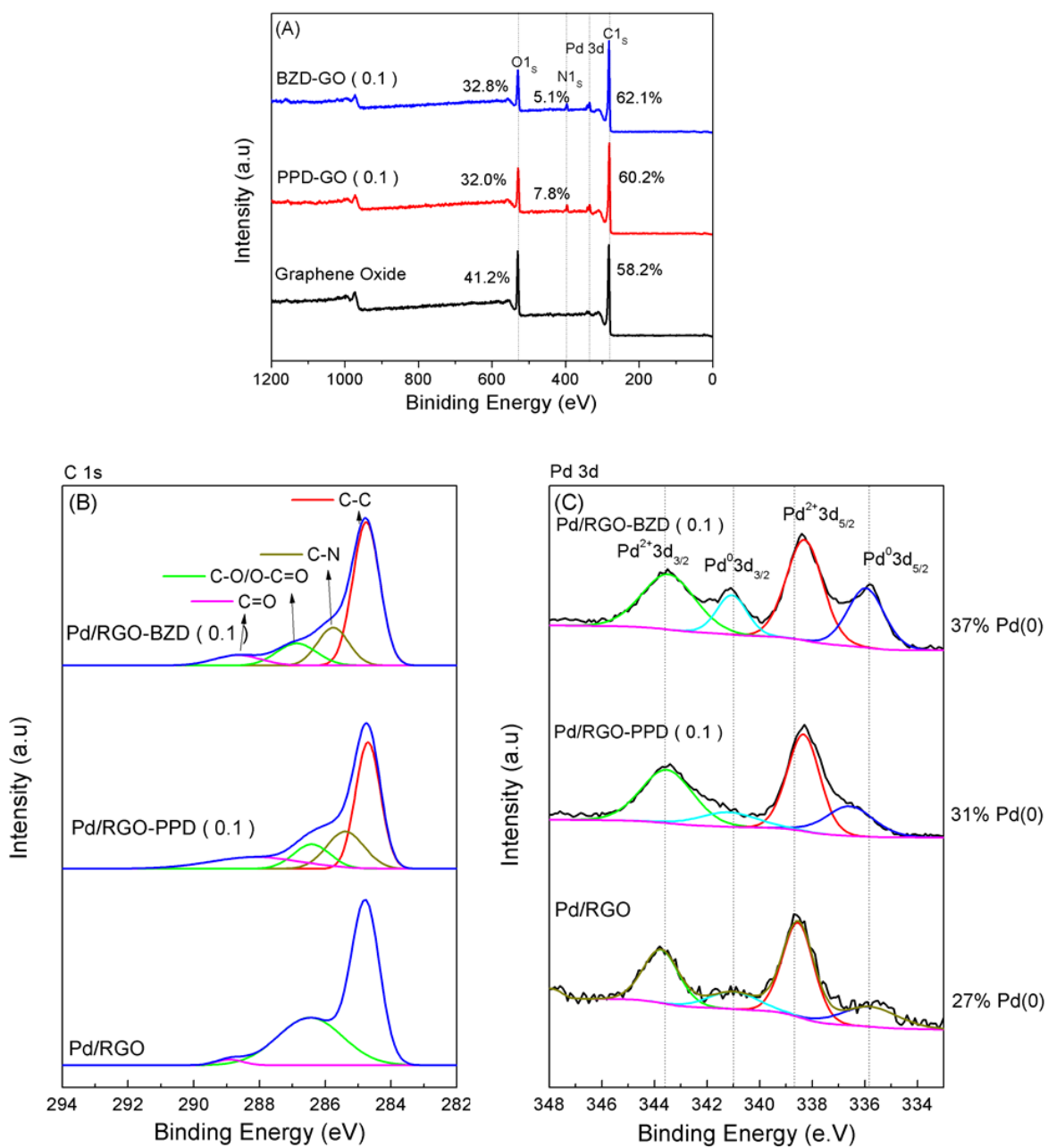


**Figure 61.** XPS Survey (A), and XPS spectra of C 1s (B), and XPS spectra of Pd 3d (C) for GO, GO-PPD (0.1), and GO-BZD (0.1).

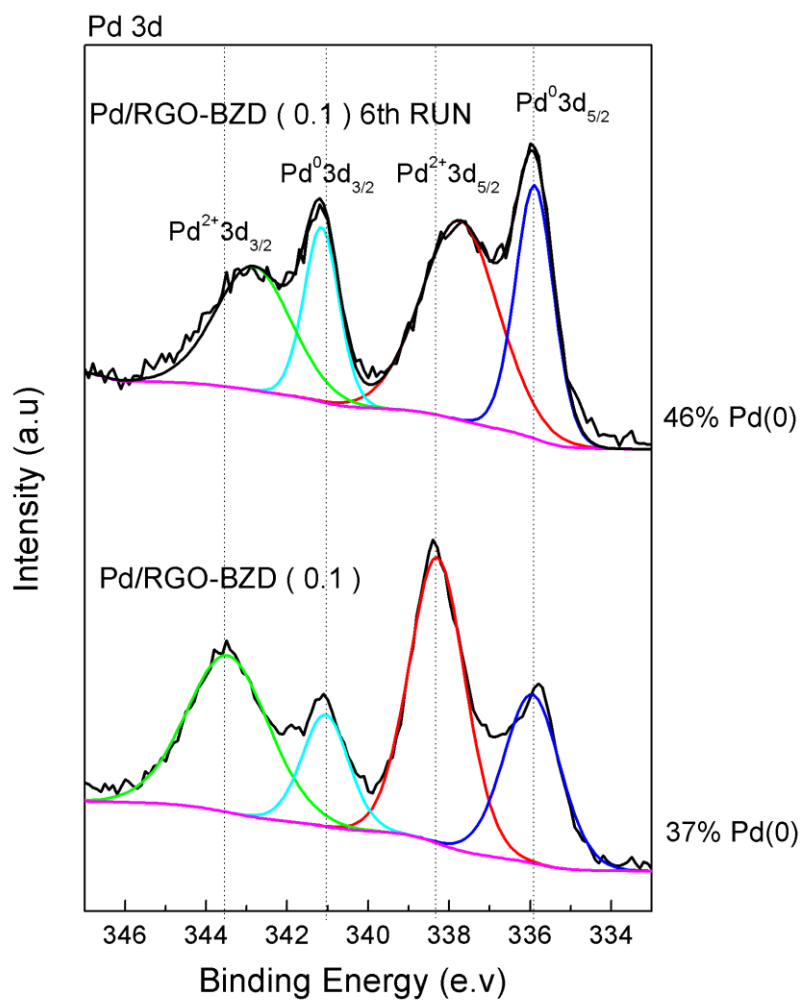


**Figure 62.** Pd 3d XPS for 3% Pd on GO-BZD before and after recycling

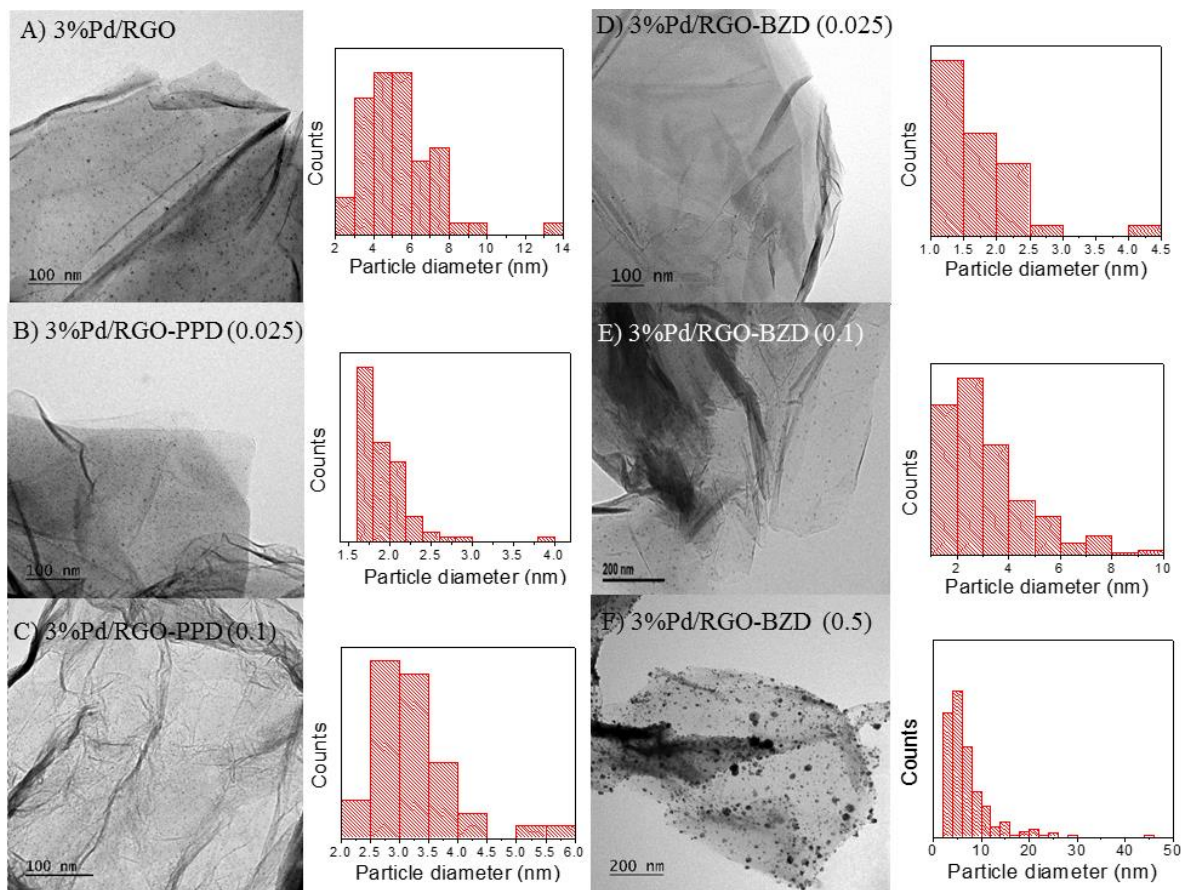


**Figure 63.** TEM images of palladium nanoparticles supported on GO, GO-PPD, and GO-BZD with varying amounts of linkers.



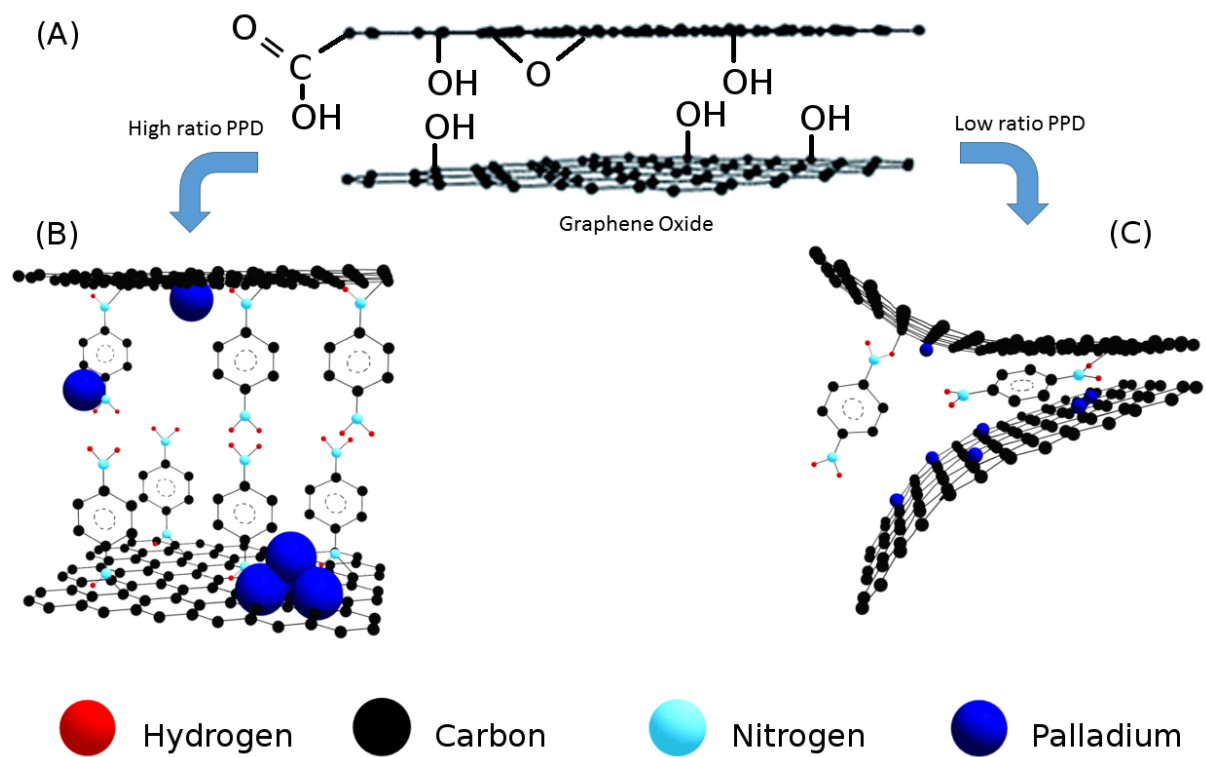


**Figure 64.** Illustration of GO (A) reduced/functionalized with a high concentration of PPD (B) and low concentration of PPD (C).

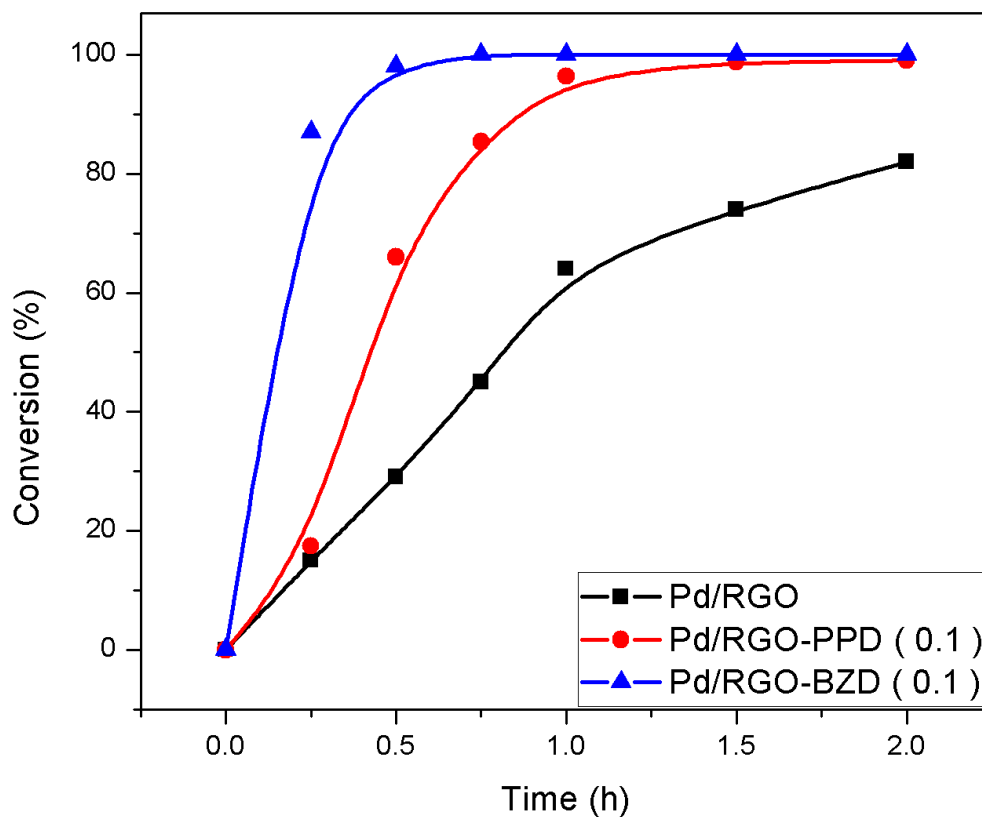


**Figure 65.** Suzuki cross coupling conversion% of 3%Pd on GO, GO-PPD ( 0.1 ), and GO-BZD ( 0.1 ). Conditions: 0.3 mol% Pd, 0.32 mmol bromobenzene, 0.38 mmol phenylboronic acid, 1 mmol  $K_2CO_3$ , and stir speed 450 rpm at r.t.

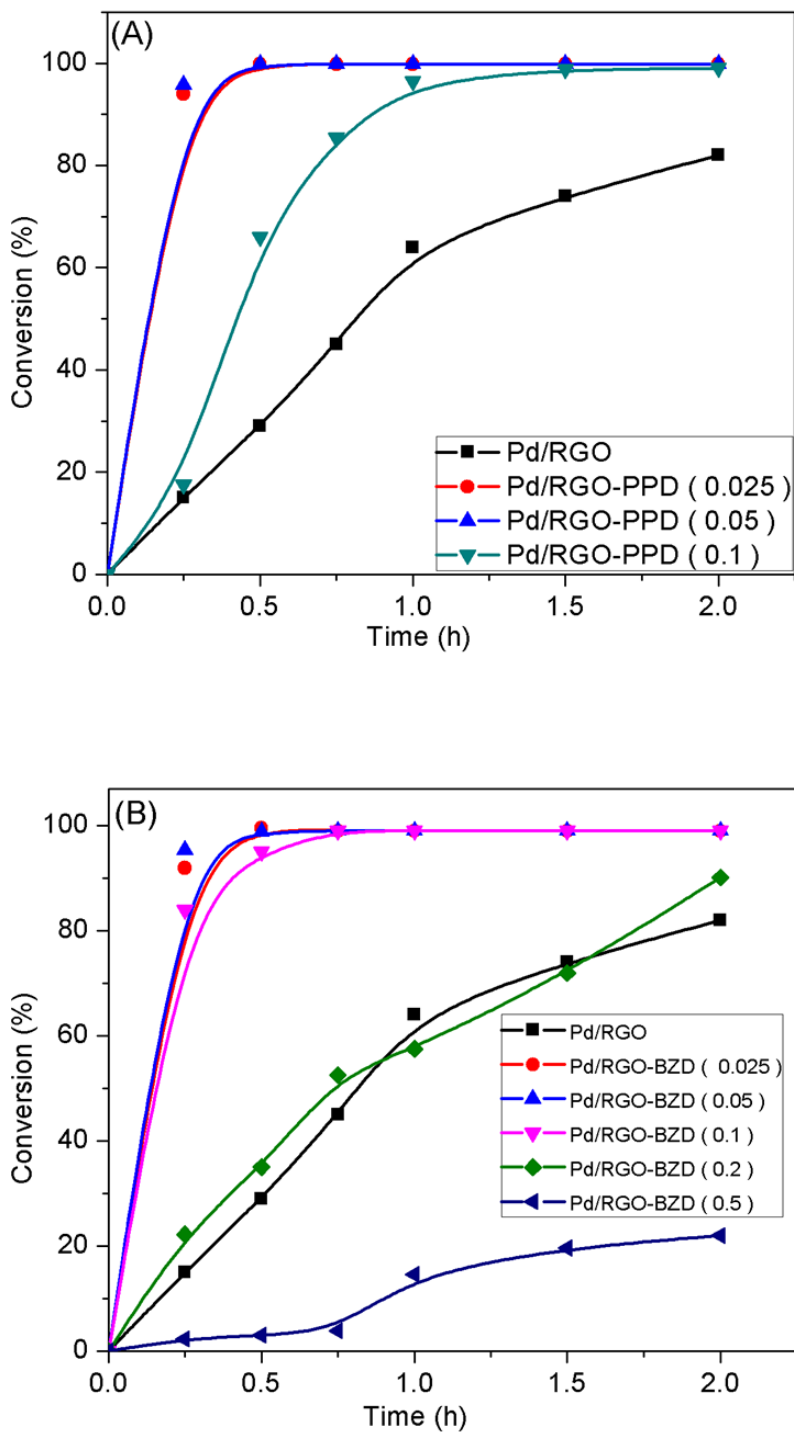


**Figure 66.** Conversion of reactants into biphenyl product for GO-BZD as a function of BZD concentration (A) and GO-PPD as a function of PPD concentration (B).

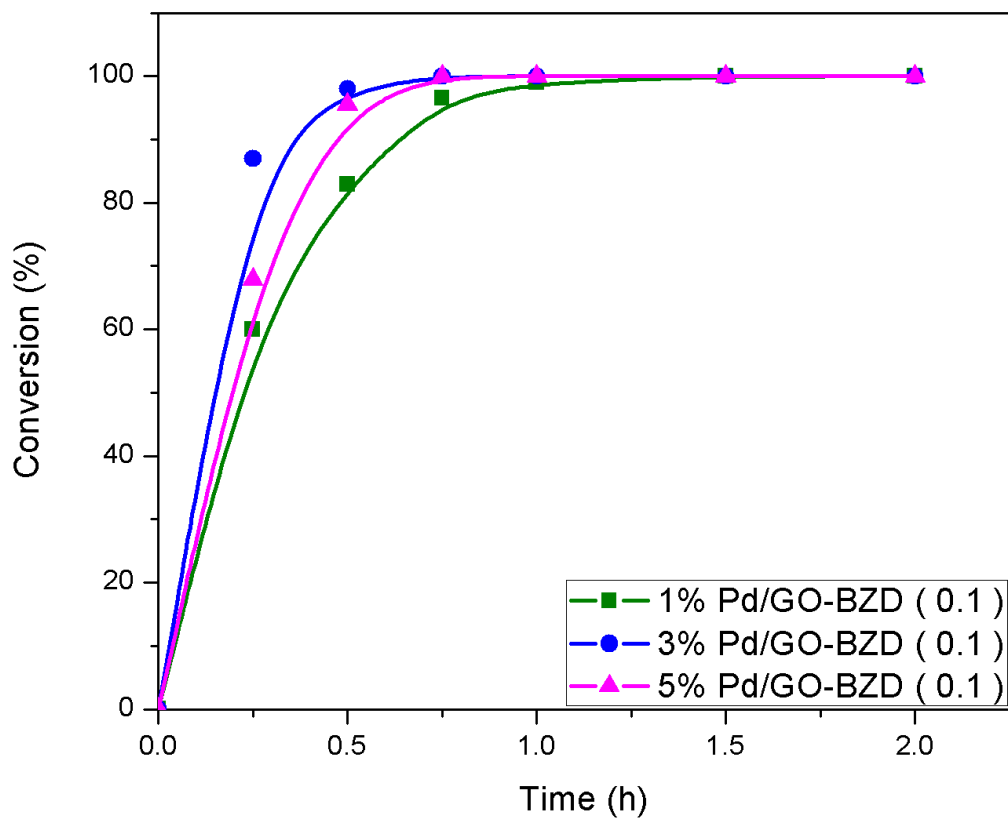


**Figure 67.** Conversion of reactants into biphenyl as a function of the effect of Pd% on GO-BZD (0.1) samples.

**Table 11.** Summary of d-spacing, Pd wt% loading, size, and TOF for GO, GO-PPD, and GO-BZD samples.

| Catalyst         | 2 $\theta$ (°) | d-Spacing (nm) | Nominal Pd loading (%) | Actual Pd loading (%) | Pd Particle Size Average (nm) | TOF h <sup>-1</sup> after 15 min |
|------------------|----------------|----------------|------------------------|-----------------------|-------------------------------|----------------------------------|
| GO               | 11.3           | 0.78           | 5                      | 3.5                   | 7.1 $\pm$ 5                   | 180                              |
| GO-PPD ( 0.025 ) | 13.1           | 0.68           | 5                      | 2.3                   | 2.9 $\pm$ 0.7                 | 1740                             |
| GO-PPD ( 0.1 )   | 7.3            | 1.21           | 5                      | 3.0                   | 2.7 $\pm$ 0.6                 | 250                              |
| GO-BZD ( 0.025 ) | 13.7           | 0.65           | 5                      | 3.3                   | 2.2 $\pm$ 1.1                 | 1230                             |
| GO-BZD ( 0.05 )  | 13.3           | 0.66           | 5                      | 3.5                   | 4.3 $\pm$ 2                   | 1160                             |
| GO-BZD ( 0.1 )   | 12.9           | 0.69           | 5                      | 3.0                   | 6.6 $\pm$ 5.6                 | 870                              |
| GO-BZD ( 0.2 )   | 11.3, 7.8      | 0.78, 1.13     | 5                      | 2.8                   | 7.5 $\pm$ 3.2                 | 340                              |
| GO-BZD ( 0.5 )   | 6.3            | 1.41           | 5                      | 2.2                   | 11.9 $\pm$ 19.9               | 45                               |

**Table 12.** Comparison of catalytic activity against other carbon-based supports by mol%, conversion%, and turnover frequency (TOF).

| Catalyst                        | Metal     | Mol% | Support (mg) | Conditions | Conversion (%) | TOF (h <sup>-1</sup> ) | Reference |
|---------------------------------|-----------|------|--------------|------------|----------------|------------------------|-----------|
| GO                              | 3.5% Pd   | 0.3  | 3.2          | r.t.       | 29 (15 min)    | 180                    | This work |
| GO-PPD (0.025)                  | 2.3% Pd   | 0.3  | 3.2          | r.t.       | 91 (15 min)    | 1740                   |           |
| GO-BZD (0.025)                  | 3.0% Pd   | 0.3  | 3.2          | r.t.       | 93 (15 min)    | 1230                   |           |
| g-C <sub>3</sub> N <sub>4</sub> | Pd/Ni     | 1.22 | 5            | r.t.       | 50 (240 min)   | 96                     | [225]     |
| g-C <sub>3</sub> N <sub>4</sub> | Pd/Ni     | 2.45 | 10           | r.t.       | 77 (240 min)   | 150                    |           |
| g-C <sub>3</sub> N <sub>4</sub> | Pd/Ni     | 3.7  | 15           | r.t.       | 89 (240 min)   | 400                    |           |
| g-C <sub>3</sub> N <sub>4</sub> | Pd/Ni     | 4.9  | 20           | r.t.       | 100 (240 min)  | 760                    |           |
| g-C <sub>3</sub> N <sub>4</sub> | Pd        | 4.9  | 20           | r.t.       | 80 (240 min)   | 76                     |           |
| g-C <sub>3</sub> N <sub>4</sub> | Ni        | 4.9  | 20           | r.t.       | 3 (240 min)    | 5                      |           |
| N-Carbon                        | 5%Pd/5%Cu | 0.24 | 4            | 30 °C      | 94 (90 min)    | 320                    | [226]     |
| Mesoporous C                    | 5% Pd     | 0.1  | -            | 40 °C      | 98 (30 min)    | 320                    | [221]     |
| GO                              | 4.1% Pd   | 0.5  | 17.5         | 40 °C      | 78 (1440 min)  | 2                      | [227]     |
| Activated C                     | 10% Pd    | 0.5  | 18.7         | 40 °C      | 87 (1440 min)  | 1                      |           |
| rGO-IL                          | -         | 0.5  | -            | 80 °C      | 95 (180 min)   | 760                    | [228]     |

**Table 13.** Recycling and ICP analysis of 3% Pd/GO-BZD ( 0.1 ). Conditions: 0.3 mol% Pd, 0.32 mmol bromobenzene, 0.38 mmol phenylboronic acid, 1 mmol K<sub>2</sub>CO<sub>3</sub>. Microwave Irradiation: 80 °C, 5 m, 3.5W.

---

| <b>Trial</b> | <b>Conversion (%)</b> | <b>Pd (%) ICP</b> |
|--------------|-----------------------|-------------------|
| <b>1</b>     | 100                   | 2.93              |
| <b>2</b>     | 99                    | 2.53              |
| <b>3</b>     | 99                    | -                 |
| <b>4</b>     | 97                    | -                 |
| <b>5</b>     | 86                    | -                 |
| <b>6</b>     | 82                    | 2.31              |

---

## Chapter 7: Results and Conclusions

A series of MOFs and carbon-based supports were synthesized and evaluated as supports for palladium nanoparticles. The MOFs studied were a cerium-trimesate polymeric crystal and a zirconium-based UiO-66-NH<sub>2</sub>. It was found that the unique properties of the Ce-MOF, {[Ce(BTC)(H<sub>2</sub>O)]DMF}<sub>n</sub>, allowed for unique interactions with gas molecules due to unsaturated cerium nodes, and the UiO-66-NH<sub>2</sub> MOF allowed for the confinement of HPW within its pores, which increased acidity of the material. GO was hybridized with the Ce-MOF support as well, and a synergistic relationship was exploited. GO was functionalized with aromatic amine spacer molecules to affect the accessibility of reactants to palladium catalytic sites.

It was found that 5% Pd/Ce-MOF was an excellent MOF with a low T<sub>100%</sub> value for the conversion of CO into CO<sub>2</sub>. This was due, in part, to the cycling between Ce<sup>3+</sup> and Ce<sup>4+</sup> oxidation states, which is allowed due to the unsaturated nature of MOF secondary-building unit metals. Cerium is one of the few lanthanide metals to have a stable Ce<sup>4+</sup> oxidation state, and the presence of f-orbitals allowed for favorable interaction with oxygen. This allowed for the Ce-MOF to adsorb oxygen and to act as an oxygen reservoir that releases oxygen at the palladium-cerium interface at higher temperatures. At lower temperatures, the Ce-MOF was shown to have a high uptake of CO<sub>2</sub> gas. This material is capable of converting CO into CO<sub>2</sub> at 373K and sequestering generated CO<sub>2</sub> gas at 273K.

The problems with Ce-MOF was the low atomic dispersion forces, low surface area measured by N<sub>2</sub> adsorption-desorption isotherms, and low dispersion in aqueous media. Liquid-solid phase reaction are predominant in heterogeneous catalysis relative to gas-solid phase reactions, so the Ce-MOF was enhanced. These problems were addressed with hybridization of Ce-MOF with GO, resulting in a MOF-PRGO composite where the composite material gains



defect sites for anchoring of palladium to increase dispersion, increased surface area, and greater dispersion in solution due to partial reduction of GO. The intercalative growth of Ce-MOF crystals between sheets of PRGO also prevented graphitic restacking of sheets, which would decrease the accessibility of palladium catalyst sites. The Ce-MOF crystals also become smaller. It was found that this hybrid material had higher palladium metal dispersion and greater acidity than its constituent components and a physical mixture of the Ce-MOF and GO resulted in inferior activity. Higher metal dispersion and greater acidity allowed for a higher conversion and selectivity of the desired products in the vanillin hydrogenation reaction.

The effect of acidity in the vanillin hydrogenation was studied by insertion of HPW into the pores of an amine-functionalized zirconium-based UiO-66-NH<sub>2</sub>. It was found that the higher acidity of the material, measured by potentiometric titration of n-butylamine, the higher the selectivity for the fully hydrogenated product. A loading of 5% HPW into the UiO-66-NH<sub>2</sub> was shown to achieve the fastest full conversion of vanillin into 2-methoxy-4-methylphenol with 0.4 wt% Pd at modest temperature and pressure. An altered mechanism was proposed: a small amount of palladium is necessary to perform the first hydrogenation step, but the presence of a strong acid in the solution allowed for the second hydrogenolysis step to convert into a more favorable hydrogenation step, allowing faster conversion of an intermediate vanillyl alcohol into the final product. This conceptualized using a bi-catalyst to reduce the amount of palladium used by substitution with HPW.

GO was functionalized with aromatic amines (PPD and BZD) and the effect of functionalization was observed for the Suzuki cross coupling reaction. It was found that a small amount of aromatic amines drastically increases the coupling of aryl halides and phenylboronic acids into biphenyl products. The material was characterized and it was seen that a small amount

of PPD or BZD decreased the palladium nanoparticle size. The tetraamine palladium salt chosen is typically employed for SEA method of palladium loading, and the partial functionalization of GO sheets with aromatic amines left sites for the strong electrostatic adsorption of palladium precursors. As the concentration of PPD or BZD increased, the amount of defect sites for nucleation of nanoparticles decreased, leading to more growth and nanoparticles became aggregated. The presence of a small amount of aromatic amine spacers helped to increase separation of layers and to help coordinate or reduce palladium into Pd(0).

The overall goal of this work was to synthesize a series of materials to act as supports for palladium nanoparticles. It was demonstrated that MOFs, GO, and composites are useful materials for dispersing palladium nanoparticles in a manner that would extend their lifetime as catalysts for a wide range of applications. Three main objectives were achieved: 1) the loading of palladium nanoparticles on MOFs, GO, and composites, 2) rational catalyst synthesis to optimize catalyst-support interaction, and 3) characterization of materials. In the four works described here, the properties of commonly used supports were enhanced through rational catalyst synthesis to improve activity of palladium nanoparticle. A Ce-MOF capable of interaction with oxygen gas was used for CO oxidation. This material was hybridized with GO to increase metal dispersion and to make the support dispersible in aqueous media. HPW was loaded into UiO-66-NH<sub>2</sub> to alter the mechanism of vanillin hydrogenation and drastically decrease palladium consumption. GO was functionalized with a small amount of aromatic amines to tune the palladium nanoparticle size.

## Appendix A

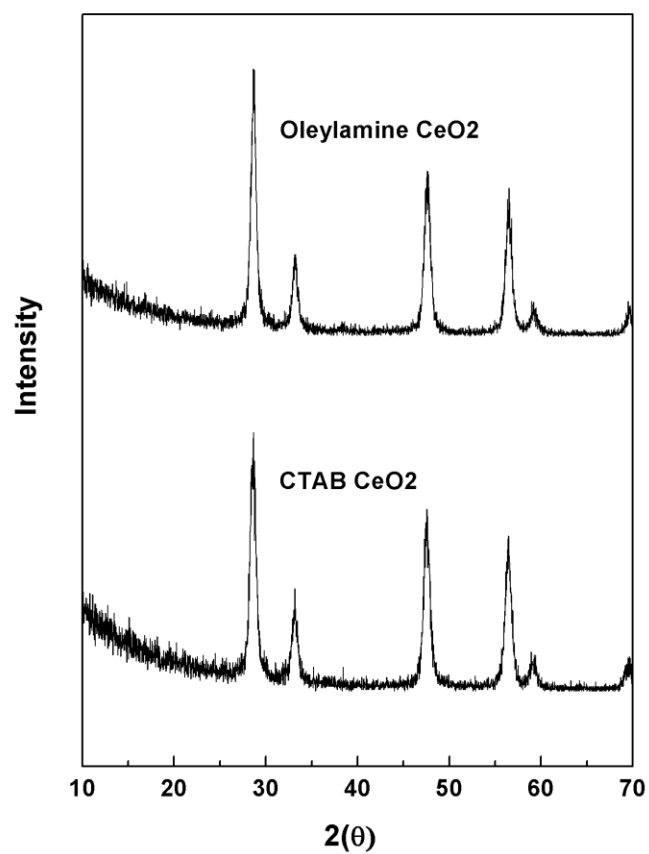


**Figure A1.** XRD diffractogram for CeO<sub>2</sub> synthesized with oleylamine and CTAB as capping agents.

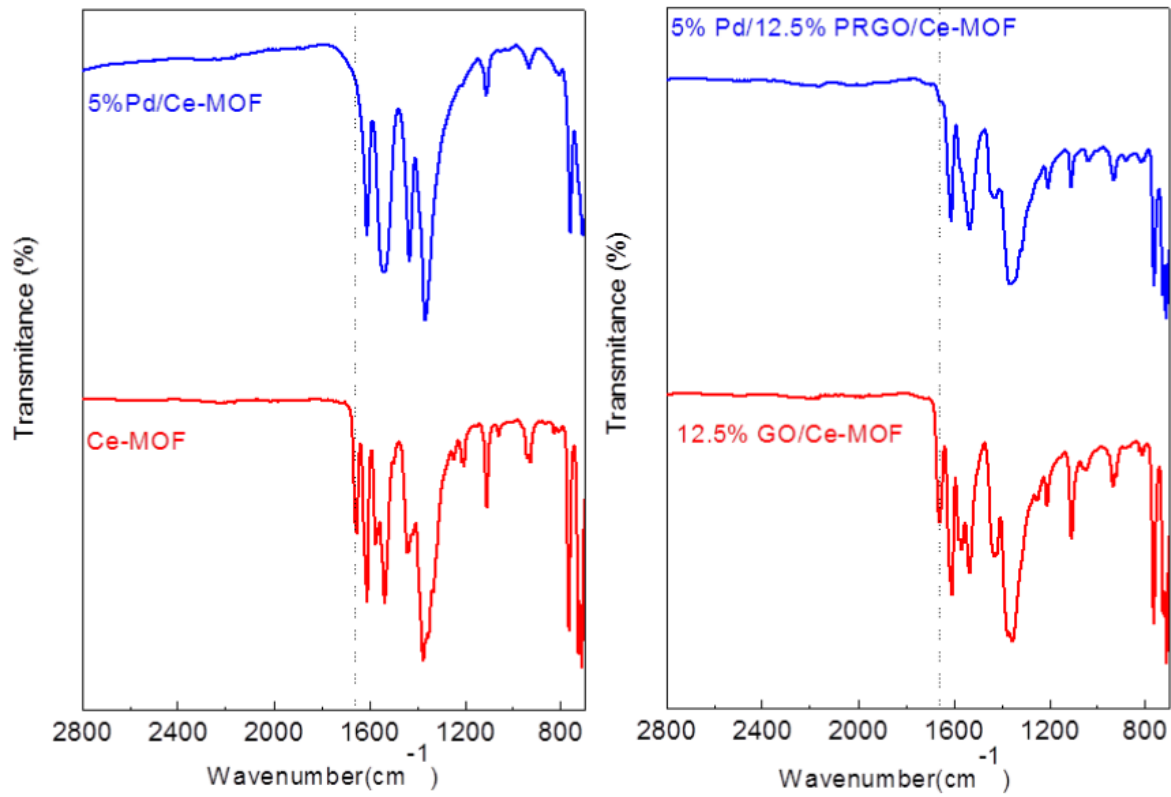


**Figure A2.** FTIR spectra of Ce-MOF and Ce-MOF-PRGO before and after 5 wt% Pd addition.

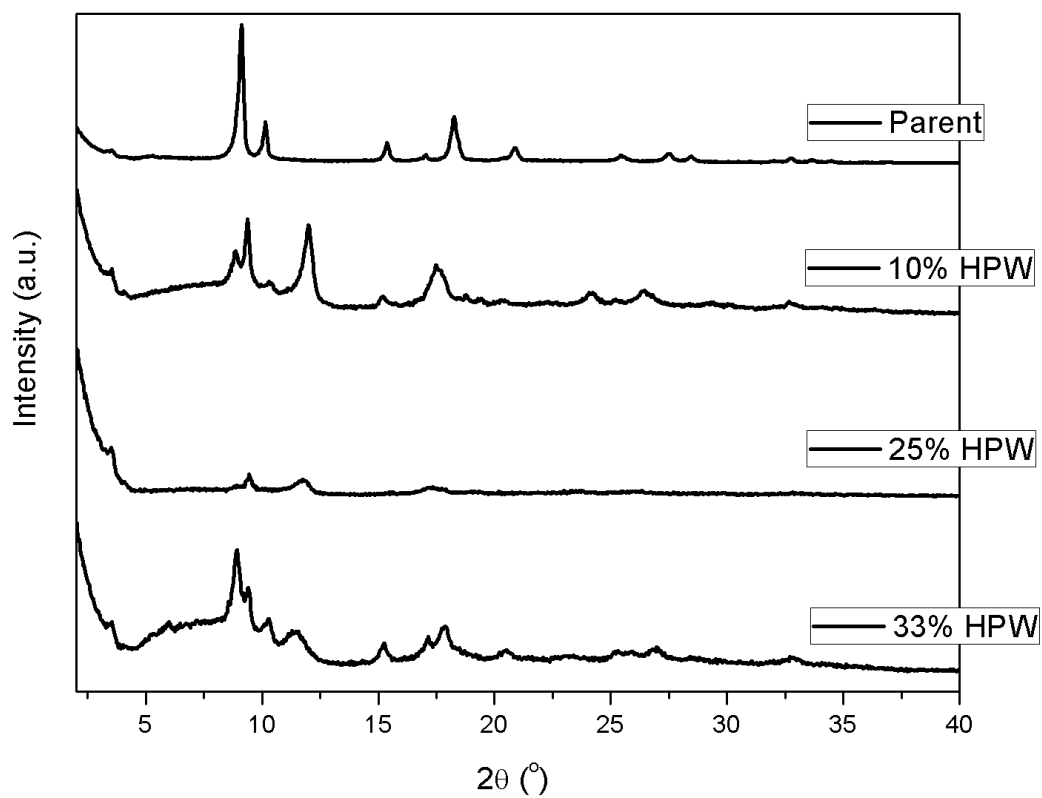


**Figure A3.** XRD spectra of MIL-53 unsuccessfully loaded with HPW.

## Vita

Andrew Lin is an American citizen born on October 28, 1990 in Columbia, SC. He earned his Chemistry B.S. from Virginia Commonwealth University in 2013. He continued to pursue higher at Virginia Commonwealth University working in the areas of nanoparticles and catalysis.

### Employment Experience

(2013-2018) **Graduate Research Student**, Richmond, VA

(2013-2018) **CHEZ 409 Teaching Assistant**, Richmond, VA

### Honors and Awards

Outstanding Physical Chemistry Graduate Student Award (2017)

### Professional Society Memberships

American Chemical Society (2017-present)

Younger Chemists Committee (2018-present)

### Publications

1. Zhang, F.; Zheng, S.; Xiao, Q.; Zhong, Y.; Zhu, W.; Lin, A.; Samy El-Shall, M., *Green Chem.* **2016**.
2. Ibrahim, A. A.; Lin, A.; Zhang, F.; Abouzeid, K. M.; El-Shall, M. S., *ChemCatChem* **2017**, *9* (469-480).
3. Lin, A.; Ibrahim, A. A.; Arab, P.; El-Kaderi, H. M.; El-Shall, M. S., *ACS Applied Materials & Interfaces* **2017**, *9* (21), 17961-17968.

## List of References

1. Brik, M. E., *Actual Chimique* **1993**, 3, 30-36.
2. Cuenya, B. R., *Thin Solid Films* **2010**, 518 (12), 3127-3150.
3. Qinghong, Z.; Kang, C.; Jincan, K.; Weiping, D.; Ye, W., *ChemSusChem* **2014**, 7 (5), 1251-1264.
4. Zheng, M.; Pang, J.; Wang, A.; Zhang, T., *Chinese J. Chem.* **2014**, 35 (5), 602-613.
5. Jin, E.; Zhang, Y.; He, L.; Harris, H. G.; Teng, B.; Fan, M., *Appl. Cat.: A Gen.* **2014**, 476, 158-174.
6. Hölderich, W. F.; Röseler, J.; Heitmann, G.; Liebens, A. T., *Catal. Today* **1997**, 37 (4), 353-366.
7. Filiciotto, L.; Balu, A. M.; Van der Waal, J. C.; Luque, R., *Catal. Today* **2018**, 302, 2-15.
8. Artz, J.; Müller, T. E.; Thenert, K.; Kleinekorte, J.; Meys, R.; Sternberg, A.; Bardow, A.; Leitner, W., *Chem. Rev.* **2018**, 118 (2), 434-504.
9. Sacchi Maria, C.; Zucchi, D.; Tritto, I.; Locatelli, P.; Dall'Occo, T., *Macromol. Rapid Comm.* **1995**, 16 (8), 581-590.
10. Muimhneachain, E. O.; McGlacken, G. P., Pd(0) nanoparticles (NPs) as catalysts in cross-coupling reactions and the homogeneous vs. heterogeneous debate. In *Organometallic Chemistry: Volume 40*, The Royal Society of Chemistry: 2016; Vol. 40, pp 33-53.
11. Yan, N.; Xiao, C.; Kou, Y., *Coordin. Chem. Rev.* **2010**, 254 (9), 1179-1218.
12. Narayanan, R.; El-Sayed, M. A., *Top. Catal.* **2008**, 47 (1), 15-21.
13. Thanh, N. T. K.; Naclean, N.; Mahiddine, S., *Chem. Rev.* **2014**, 2014 (114), 7610-7630.
14. Goesten, M. G.; Magusin, P. C. M. M.; Pidko, E. A.; Mezari, B.; Hensen, E. J. M.; Kapteijn, F.; Gascon, J., *Inorg. Chem.* **2014**, 53, 882-887.

15. Loiseau, T.; Serre, C.; Huguenard, C.; Fink, G.; Taulelle, F.; Henry, M.; Bataille, T.; Férey, G., *Chem. Eur. J.* **2004**, *10*, 1373-1382.
16. Si, X., *Dalton Trans.* **2012**, *41*, 3119-3122.
17. Zhu, M.; Srivinas, D.; Bhogeswararao.; Ratnasamay, P.; Carreon, M. A., *Cat. Comm.* **2012**, *32*, 36-40.
18. Majano, G.; Perez-Ramirez, J., *Helvetica Chimica Acta* **2012**, *95*, 2278-2286.
19. Langmi, H. W.; Ren, J.; North, B.; Mathe, M.; Bessarabov, D., *Electrochimica Acta* **2014**, *128*, 368-392.
20. Xu, Z.; L., Y.; Xu, C., *Anal. Chem.* **2015**, *87*, 3438-3444.
21. Kobayashi, H.; Mitsuka, Y.; Kitagawa, H., *Inorg. Chem.* **2016**, *55*, 7301-7310.
22. Miao, Z.; Qi, C.; Wensley, A. M.; Luan, Y., *RSC Adv.* **2016**, *6* (71), 67226-67231.
23. Piscopo, C. G.; Polyzoidis, A.; Schwarzer, M.; Loebbecke, S., *Micropor. Mesopor. Mat.* **2015**, *208*, 30-35.
24. Alexander, K.; Sebastian, E.; T., A. P.; Konrad, H.; I., V. S.; Bernhard, R., *Chem-Eur. J.* **2016**, *22* (36), 12800-12807.
25. Kandiah, M.; Usseglio, S.; Svelle, S.; Olsbye, U.; Lillerud, K. P.; Tilset, M., *J. Mat. Chem. A* **2010**, *20*, 9848-9851.
26. Randviir, E. P.; Brownson, D. A. C.; Banks, C. E., *Mater. Today* **2014**, *17* (9), 426-432.
27. Montes-Navajas, P.; Asenjo, N. G.; Santamaría, R.; Menéndez, R.; Corma, A.; García, H., *Langmuir* **2013**, *29* (44), 13443-13448.
28. Kim, J.; Park, S.-J.; Min, D.-H., *Anal. Chem.* **2017**, *89* (1), 232-248.
29. Thangavelu, K.; Palanisamy, S.; Chen, S.-M.; Velusamy, V.; Chen, T.-W.; Ramaraj, S. K., *J. Electrochem. Soc.* **2016**, *163* (14), B726-B731.



30. Xia, D.-c.; Zhou, L.; Qiao, S.; Zhang, Y.; Tang, D.; Liu, J.; Huang, H.; Liu, Y.; Kang, Z., *Materials Research Bulletin* **2016**, *74*, 441-446.
31. Liu, Z.; Feng, Y.; Wu, X.; Huang, K.; Feng, S.; Dong, X.; Yang, Y.; Zhao, B., *RSC Adv.* **2016**, *6* (101), 98708-98716.
32. Lee, D. U.; Kim, B. J.; Chen, Z., *J. Mat. Chem. A* **2013**, *1* (15), 4754-4762.
33. Alazmi, A.; Rasul, S.; Patole, S. P.; Costa, P. M. F. J., *Polyhedron* **2016**, *116*, 153-161.
34. Banhart, F.; Kotakoski, J.; Krasheninnikov, A. V., *ACS Nano* **2011**, *5* (1), 26-41.
35. Jabbari, V.; Veleta, J. M.; Zarei-Chaleshtori, M.; Gardea-Torresdey, J.; Villagrán, D., *Chem. Eng. J.* **2016**, *304*, 774-783.
36. Alam, S. N.; Sharma, N.; Kumar, L., *Graphene* **2017**, *6*, 1-18.
37. Almasi, M.; Zelenak, V.; Opanasenko, M.; Cisarova, I., *Catal.Today* **2015**, *243*, 184-194.
38. Katz, M. J.; Brown, Z. J.; Colon, Y. J.; Siu, P. W.; Scheidt, K. A.; Snurr, R. Q.; Hupp, J. T.; Farha, O. K., *Chem. Comm.* **2013**, *49* (82), 9449-9451.
39. Bromberg, L.; Su, X.; Hatton, T. A., *ACS App. Mat. & Interf.* **2013**, *5*, 5468-5477.
40. Saoud, K. M. E. Carbon Monoxide Oxidation on Nanoparticle Catalysts and Gas Phase Reactions of Small Molecules and Volatile Organics with Metal Cations. Ph.D. Thesis, Virginia Commonwealth University, 2005.
41. Kahandal, S. S.; Kale, S. R.; Disale, S. T.; Jayaram, R. V., *Catalysis Science & Technology* **2012**, *2* (7), 1493-1499.
42. El-Shall, M. S.; Abdelsayad, V.; Khder, A. S.; Hassan, H. M. A.; El-Kaderi, H. M., *J. of Mat. Chem.* **2009**, *19* (41), 7625-7631.
43. Lin, A.; Ibrahim, A. A.; Arab, P.; El-Kaderi, H. M.; El-Shall, M. S., *ACS Applied Materials & Interfaces* **2017**, *9* (21), 17961-17968.

44. O'Keefe, M.; Yaghi, O. M., *Chem. Rev.* **2012**, *112*, 675-702.
45. Furukawa, H.; Cordova, K. E.; O'Keefe, M.; Yaghi, O. M., *Science* **2013**, *341* (974-986).
46. Jiang, H. L.; Liu, B.; Akita, T.; Haruta, M.; Sakurai, H.; Xu, Q., *J. Am. Chem. Soc.* **2009**, *131*, 11302-11303.
47. Guo, Z.; Xiao, C.; Maligal-Ganesh, R. V.; Zhou, L.; Goh, T. W.; Li, X.; Tesfagaber, D.; Thiel, A.; Huang, W., *ACS Catal.* **2014**, *4*, 1340-1348.
48. Choi, K. M.; Na, K.; Somorjai, G. A.; Yaghi, O. M. C., *J. Am. Chem. Soc.* **2015**, *137*, 7810-7816.
49. Bhogeswararao, S.; Srinivas, D., *J. Cat.* **2012**, *285*, 31-40.
50. Kitagawa, S.; Kitaura, R.; Noro, S., *Angew. Chem., Int. Ed.* **2004**, *43*, 2334-2375.
51. Morozan, A.; Jaouen, F., *Energy Environ. Sci.* **2012**, *2012*, 9269-9290.
52. Li, S. L.; Xu, Q., *Energy Environ. Sci.* **2013**, *6*, 1656-1683.
53. Zou, R. Q.; Sakurai, H.; Xu, Q. P., *Angew. Chem., Int. Ed.* **2006**, *45*, 2542-2546.
54. Zou, R. Q.; Sakurai, H.; Han, S.; Zhong, R. Q.; Xu, Q., *129* **2007**, 8402-8403.
55. Ye, J. Y.; Liu, C. J., *Chem. Commun.* **2011**, (47), 2167-2169.
56. Zhao, Y.; Zhong, C.; Liu, C. J., *Catal. Commun.* **2013**, *38*, 74-76.
57. Qian, L.; Zhen, Z.; Jian, L.; Yue-Chang, W.; Gui-Yuan, J.; Ai-Jun, D., *Acta Phys.-Chim. Sin.* **2014**, *30*, 129-134.
58. Yang, Y. L.; Saoud, K. M.; Abdelsayed, V.; Glaspell, G.; Deevi, S.; El-Shall, M. S., *Catal. Commun.* **2006**, *7*, 281-284.
59. Glaspell, G.; Hassan, H. M. A.; Elzatahry, A.; Abdalsayed, V.; El-Shall, M. S., *Top. Catal.* **2008**, *47*, 22-31.

60. Glaspell, G.; Hassan, H. M. A.; Elzatahry, A.; Fuoco, L.; Radwan, N. R. E.; El-Shall, M. S., *J. Phys. Chem. B* **2006**, *110*, 21387-21393.
61. Moreno, M.; Bergamini, L.; Baronetti, G. T.; Laborde, M. A.; Mariño, F. J., *Int. J. Hydrogen Energ.* **2010**, *35* (11), 5918-5924.
62. Montini, T.; Melchionna, M.; Monai, M.; Fornasiero, P., *Chem. Rev.* **2016**, *116* (10), 5987-6041.
63. Min, P.; Zhang, S.; Xu, Y.; Li, R., *Appl. Surf. Sci.* **2018**, *448*, 435-443.
64. Holleman, A. F. W., Egon (2001), Wiberg, Nils, ed., *Inorganic Chemistry*, translated by Eagleson, Mary; Brewer, William, San Diego/Berlin: Academic Press/De Gruyter, pp. 1703–5.
65. Jhung, S. H.; Lee, J.; Yoon, J. W.; Serre, C.; Ferey, G.; Chang, J., *Adv. Mater.* **2007**, *19* (121-124).
66. Ibrahim, A. A.; Lin, A.; Zhang, F.; Abouzeid, K. M.; El-Shall, M. S., *ChemCatChem* **2017**, *9* (469-480).
67. Khan, N. A.; Haque, M. M.; Jhung, S. H., *Eur. J. Inorg. Chem.* **2010**, *31*, 4975-4981.
68. He, L.; Dumeé, L. F.; Liu, D.; Velleman, L.; She, F.; Banos, C.; Davies, J. B.; Kong, L., *RSC Adv.* **2015**, *5* (10707-10715).
69. Zhang, F.; Wang, P.; Koberstein, J.; Khalid, S.; Chan, S. W., *Surf. Sci.* **2004**, *563*, 74-82.
70. Kar, S.; Patel, C.; Santra, S., *J. Phys. Chem. C.* **2009**, *2009*, 4862-4867.
71. Saeidi, S.; Amin, N. A. S.; Rahimpour, M. R., *J. CO2 Util.* **2014**, *5*, 66-81.
72. Sutradhar, N.; Sinhamahapatra, A.; Pahari, S.; Jayachandran, M.; Subramanian, B.; Bajaj, H. C.; Panda, A. B., *J. Phys. Chem. B* **2011**, *115*, 7628-7637.
73. Adhikari, A. K.; Lin, K. S., *Chem. Eng. J.* **2016**, *284*, 1348-1360.
74. Cheon, Y. E.; Suh, M. P. E., *Angew. Chem., Int. Ed.* **2009**, *48*, 2899-2903.

75. Cao, Y.; Zhao, Y.; Lv, Z.; Song, F.; Zhong, Q., *J. Ind. Eng. Chem.* **2015**, *27*, 102-107.
76. Mishra, A. K.; Ramaprabhu, S., *Chem. Eng. J.* **2012**, *187*, 10-15.
77. Moon, S. Y.; Bae, J. S.; Jeon, E.; Park, J.-W., *Angew. Chem., Int. Ed.* **2010**, *49*, 9504-9508.
78. Kaur, P.; Hupp, J. H.; Nguyen, S. T. P., *ACS Catal.* **2011**, *1* (819-835).
79. Kim, T.; Kim, D. H.; Kim, S.; Kim, Y. D.; Bae, Y. S.; Lee, C. Y., *Polyhedron* **2015**, *90*, 18-22.
80. Zamaro, J. M.; Perez, N. C.; Miro, E. E.; Casado, C.; Seoane, B.; Tellez, C.; Coronas, J., *Chem. Eng. J.* **2012**, *195*, 180-187.
81. Rao, K. N.; Bharali, P.; Thrimurthulu, G.; Reddy, B. M., *Catal. Commun.* **2010**, *11*, 863-866.
82. Mai, H.; Zhang, D.; Shi, L.; Yan, T.; Li, H. H., *Appl. Surf. Sci.* **2011**, *257*, 7551-7559.
83. Liu, B.; Liu, J.; Li, T.; Zhao, Z.; Gong, X.-Q.; Chen, Y.; Duan, A.; Jiang, G.; Wei, Y., *J. Phys. Chem.* **2015**, *119*, 12923-12934.
84. Judkins, R. R.; Fulkerson, W.; Sanghvi, M. J., *Energy & Fuels* **1993**, *7*, 14-22.
85. Badawry, W. A., *J. of Adv. Res.* **2015**, *6*, 123-132.
86. Sharma, S.; Jain, K. K.; Sharma, A., *Mat. Sci. App.* **2015**, *6*, 1145-1155.
87. Lee, Y.; Park, C.; Balaji, N.; Lee, Y.; Dao, V. A., *Israel J. Chem.* **2015**, *10*, 1050-1063.
88. Zhao, Y.; Pan, T.; Zuo, Y.; Q., G.; Fu, Y., *Biorec. Tech.* **2013**, *147*, 37-42.
89. Adjaye, J. D.; Bakhshi, N. N., *Biomass Bioenerg.* **1995**, *8*, 131-149.
90. Carlson, T. R.; Jae, J.; Lin, Y.; Tompsett, G. A.; Huber, G. W., *J. Cat.* **2010**, *1*, 110-124.

91. McMeekin, D. P.; Sadoughi, G.; Rehman, W.; Eperon, G. E.; Michael, S.; Horanther, M. T.; Haghghirad, A.; Korte, L.; Rech, B.; Johnston, M. B.; Herz, L. M.; Snaith, H. J., *Sci.* **2016**, *351*, 151-155.
92. Li, C.; Zhao, X.; Wang, A.; Huber, G.; Zhang, T., *Chem. Rev.* **2015**, *115*, 11559-11624.
93. Zhang, J.; Wang, K.; Nolte, W.; Choi, Y. S.; Brown, R. C.; Shanks, B. H., *ACS Catal.* **2016**, *6*, 2608-2621.
94. Chan, X.; Nan, W.; Mahajan, D.; Kim, T., *Cat. Comm.* **2015**, *72*, 11-15.
95. Wang, C.; Wang, L.; Zhang, J.; Wang, H.; Lewis, J. P.; Xiao, F., *J. Am. Chem. Soc.* **2016**, *138*, 7880-7883.
96. Wang, Y.; He, W.; W.L.; Yang, J.; Xiang, X., *Chem. Asia J.* **2015**, *10*, 1561-1570.
97. Bindwal, A. B.; Vaidya, P. D., *Energy & Fuels* **2014**, *28*, 5.
98. Deng, W.; Zhang, H.; Wu, X.; Li, R.; Zhang, Q.; Wang, Y., *Green Chem.* **2015**, *17*, 5009-5018.
99. White, R. J.; Luque, R.; Budarin, V. L.; Clark, J. H.; Macquarrie, D. J., *Chem. Soc. Rev.* **2009**, *38*, 481-494.
100. Campbell, C. T.; Grant, A. W.; Starr, D. E.; Parker, S. C.; Bondzie, V. A., *Top. Catal.* **2000**, *14* (1), 43-51.
101. Santra, A. K.; Goodman, D. W., *J. Phys. Condens. Mat* **2003**, *15*, 31-62.
102. Gao, F.; Goodman, D. W., *Annu. Rev. Phys. Chem.* **2012**, *63* (1), 265-286.
103. McFarland, E. W.; Metiu, H., *Chem. Rev.* **2013**, *113* ( 6 ), 4391-4427.
104. Corma, A.; García, H.; Llabrés i Xamena, F. X., *Chem. Rev.* **2010**, *110* (8), 4606-4655.
105. Su, D. S.; Perathoner, S.; Centi, G., *Chem. Rev.* **2013**, *113* (8), 5782-5816.
106. Torres Galvis, H. M.; de Jong, K. P., *ACS Catal.* **2013**, *3* (9), 2130-2149.

107. Lu, G.; Li, S.; Guo, Z.; Farha, O. K.; Hauser, B. G.; Qi, X.; Wang, Y.; Wang, X.; Han, S.; Liu, X.; DuChene, J. S.; Zhang, H.; Zhang, Q.; Chen, X.; Ma, J.; Loo, S. C. J.; Wei, W. D.; Yang, Y.; Hupp, J. T.; Huo, F., *Nat. Chem.* **2012**, *4*, 310.
108. Pachfule, P.; Yang, X.; Zhu, Q.-L.; Tsumori, N.; Uchida, T.; Xu, Q., *J. Mat. Chem. A* **2017**, *5* (10), 4835-4841.
109. Yu, J.; Mu, C.; Yan, B.; Qin, X.; Shen, C.; Xue, H.; Pang, H., *Mater. Horiz.* **2017**, *4* (4), 557-569.
110. Zhao, M.; Deng, K.; He, L.; Liu, Y.; Li, G.; Zhao, H.; Tang, Z., *J. Am. Chem. Soc.* **2014**, *136* (5), 1738-1741.
111. Pan, X.; Bao, X., *Acc. Chem. Res.* **2011**, *44* (8), 553-562.
112. Crossley, S.; Faria, J.; Shen, M.; Resasco, D. E., *Science* **2010**, *327* (5961), 68.
113. Scheuermann, G. M.; Rumi, L.; Steurer, P.; Bannwarth, W.; Mülhaupt, R., *J. Am. Chem. Soc.* **2009**, *131* (23), 8262-8270.
114. Bagri, A.; Mattevi, C.; Acik, M.; Chabal, Y. J.; Chhowalla, M.; Shenoy, V. B., *Nat. Chem.* **2010**, *2*, 581.
115. Heterogeneous Catalysis by Metal Nanoparticles Supported On Graphene, M. S. E.-S. i. G. S. P. a. A. E. C. N. R. R., A. K. Sood), Wiley-VCH, 2013, Chap. 10, pp. 303–338. .
116. Dai, B.; Chen, K.; Wang, Y.; Kang, L.; Zhu, M., *ACS Catal.* **2015**, *5* (4), 2541-2547.
117. Moussa, S.; Abdelsayed, V.; Samy El-Shall, M., *Chem. Phys. Lett.* **2011**, *510* (4), 179-184.
118. Su, C.; Loh, K. P., *Acc. Chem. Res.* **2013**, *46* (10), 2275-2285.
119. Moussa, S.; Siamaki, A. R.; Gupton, B. F.; El-Shall, M. S., *ACS Catalysis* **2012**, *2* (1), 145-154.

120. Moussa, S.; Atkinson, G.; SamyEl-Shall, M.; Shehata, A.; AbouZeid, K. M.; Mohamed, M. B., *J. Mat. Chem.* **2011**, *21* (26), 9608-9619.
121. Moussa, S. O.; Panchakarla, L. S.; Ho, M. Q.; El-Shall, M. S., *ACS Catal.* **2014**, *4* (2), 535-545.
122. Bandosz, T. J.; Petit, C., *Adsorption* **2011**, *17* (1), 5-16.
123. Jahan, M.; Liu, Z.; Loh Kian, P., *Adv. Funct. Mater.* **2013**, *23* (43), 5363-5372.
124. Zhou, X.; Huang, W.; Shi, J.; Zhao, Z.; Xia, Q.; Li, Y.; Wang, H.; Li, Z., *J. Mat. Chem. A* **2014**, *2* (13), 4722-4730.
125. El-Shall, M. S.; Abdelsayed, V.; Khder, A. E. R. S.; Hassan, H. M.; A.; El-Kaderi, H. M.; Reich, T. E., *J. Mater. Chem.* **2009**, (19), 7625-7631.
126. Petit, C.; Bandosz Teresa, J., *Adv. Funct. Mater.* **2009**, *20* (1), 111-118.
127. Stobinski, L.; Lesiak, B.; Malolepszy, A.; Mazurkiewicz, M.; Mierzwa, B.; Zemek, J.; Jiricek, P.; Bieloshapka, I., *J. Electron Spectrosc.* **2014**, *195*, 145-154.
128. Zhang, F. J., Y.; Zhong, Y.; Zhu, W.; Ibrahim, A.A.; El-Shall M.S., *J. Mat. Chem. A* **2015**, *3*, 17008-17015.
129. Zhang, F.; Zheng, S.; Xiao, Q.; Zhong, Y.; Zhu, W.; Lin, A.; Samy El-Shall, M., *Green Chem.* **2016**.
130. Hassan, H. M. A.; Abdelsayed, V.; Khder, A. E. R. S.; AbouZeid, K. M.; Ternner, J.; El-Shall, M. S.; Al-Resayes, S. I.; El-Azhary, A. A., *J. Mat. Chem.* **2009**, *19* (23), 3832-3837.
131. Ferrari, A. C., *Solid State Comm.* **2007**, *143* (1), 47-57.
132. Cançado, L. G.; Jorio, A.; Ferreira, E. H. M.; Stavale, F.; Achete, C. A.; Capaz, R. B.; Moutinho, M. V. O.; Lombardo, A.; Kulmala, T. S.; Ferrari, A. C., *Nano Lett.* **2011**, *11* (8), 3190-3196.

133. Wang, Q.; Yang, Y.; Gao, F.; Ni, J.; Zhang, Y.; Lin, Z., *ACS Appl. Mat. Interf.* **2016**, *8* (47), 32477-32487.
134. Peng, W.; Li, H.; Liu, Y.; Song, S., *J. Molec. Liq.* **2016**, *221*, 82-87.
135. Siamaki, A. R.; Khder, A. E. R. S.; Abdelsayed, V.; El-Shall, M. S.; Gupton, B. F., *J. Cat.* **2011**, *279* (1), 1-11.
136. Elazab, H. A.; Siamaki, A. R.; Moussa, S.; Gupton, B. F.; El-Shall, M. S., *Appl. Catal. A: Gen.* **2015**, *491*, 58-69.
137. Khder, A. E. R. S.; Hassan, H. M. A.; El-Shall, M. S., *App. Cat. A: Gen.* **2014**, *487*, 110-118.
138. Cid, R.; Pecchi, G., *App. Cat.* **1985**, *14*, 15-21.
139. Aijaz, A.; Zhu, Q.-L.; Tsumori, N.; Akita, T.; Xu, Q., *Chem. Comm.* **2015**, *51* (13), 2577-2580.
140. Del Angel, G.; Coq, B.; Figueras, F., *J. Cat.* **1985**, *95* (1), 167-180.
141. Zhang, F.; Jin, Y.; Fu, Y.; Zhong, Y.; Zhu, W.; Ibrahim, A. A.; El-Shall, M. S., *J. Mat. Chem. A* **2015**, *3*, 17008-17015.
142. Zhu, Z.; Tan, H.; Wang, J.; Yu, S.; Zhou, K., *Green Chem.* **2014**, *16*, 2636-2643.
143. Xu, X.; Gong, Y.; Zhang, P.; Li, H.; Wang, Y., *J. Am. Chem. Soc.* **2012**, *134*, 16987-16990.
144. Lv, Z.; Sun, Q.; Meng, X.; Xiao, F.-S., *J. Mat. Chem. A* **2013**, *1* (30), 8630-8635.
145. Ftouni, J.; Munoz-Murillo, A.; Goryachev, A.; Hofman, J. P.; Hensen, E. J. M.; Lu, L.; Kiely, C. J.; Bruijninx, P. C. A.; Weckhuysen, B. M., *ACS Cat.* **2016**, *6*, 5462-5472.
146. Ragon, F.; Campo, B.; Yang, Q.; Martineau, C.; Wiersum, A. D.; Lago, A.; Guillerm, V.; Hemsley, C.; Eubank, J. F.; Vishnuvarthan, M.; Taulelle, F.; Horcajada, P.; Vimont, A.;



- Llewellyn, P. L.; Daturi, M.; Devautour-Vinot, S.; Maurin, G.; Serre, C.; Devic, T.; Clet, G., *J. Mat. Chem. A* **2015**, *3* (7), 3294-3309.
147. Nomiya, K.; Yagishita, K.; Nemoto, Y.; Kamataki, T., *J. Of Molec. Cat. A* **1997**, *126*, 43-51.
148. Chen, Y.; Yao, Z.; Miras, H. N.; Song, Y., *Chem. Pub. Eur.* **2015**, *21*, 10812-10820.
149. Sabyrov, K.; Jiang, J.; Yaghi, O. M.; Somorjai, G. A., *J. Am. Chem. Soc.* **2017**, *139* (36), 12382-12385.
150. Bajpe, S. R.; Kirschhock, C. E. A.; Aerts, A.; Breynaert, E.; Absillis, G.; Parac-Vogt, T. N.; Giebel, L.; Martens, J. A., *Chem. Eur. J.* **2010**, *16*, 3926-3932.
151. Cavka, J. H. J., S.; Olsbye, U.; Guillou, N.; Lamberti, C.; Bordiga, S.; and Lillerud, K.P., *JACS Comm.* **2008**, *130* (142), 13850–13851.
152. Yang, X.-L.; Qiao, L.-M.; Dai, W.-L., *Micropor. Mesopor. Mat.* **2015**, *211*, 73-81.
153. Salomon, W.; Roch-Marchal, C.; Mialane, P.; Rouschmeyer, P.; Serre, C.; Haouas, M.; Taulelle, F.; Yang, S.; Ruhlmann, L.; Dolbecq, A., *Chem. Comm.* **2015**, *51*, 2972-2975.
154. Song, Y.; Wang, X.; Qu, Y.; Huang, C.; Li, Y.; Chen, B., *Catalysts* **2012**, *106*, 170-172.
155. Zhang, F.; Zheng, S.; Xiao, Q.; Zhong, Y.; Zhu, W.; Lin, A.; El-Shall, M. S., *Green Chem.* **2016**, *18*, 2900-2908.
156. Shen, L.; Wu, W.; Liang, R.; Lin, R.; Wu, L., *Nanoscale* **2013**, *5*, 9374-9382.
157. Kumar, A.; Singh, P.; Kumar, S.; Chandra, R.; Mozumdar, S., *J. Molec. Cat. A: Chem.* **2007**, *276*, 95-101.
158. Nguyen, H. G. T.; Mao, L.; Peters, A. W.; Audu, C. O.; Brown, Z. J.; Farha, O. K.; Hupp, J. T.; Nguyen, S. T., *Cat. Sci. Tech.* **2015**, *5*, 4444-4451.
159. Liu, X.; Truitt, R. E., *J. Am. Chem. Soc.* **1997**, *119*, 9856-9860.

160. Pejov, L.; Skapin, T., *Chem. Phys. Lett.* **2004**, *400*, 453-461.
161. Kondo, J. N.; Nishitani, R.; Yoda, E.; Yokoi, T.; Tatsumi, T.; Domen, K., *Phys. Chem. Chem. Phys.* **2010**, *12*, 11576-11586.
162. Jiang, J.; Yaghi, O. M., *Chem. Rev.* **2015**, *115*, 6966-6997.
163. Kim, M. J.; Park, S. M.; Song, S.-J.; Won, J.; Lee, Y. J.; Yoon, M.; Kim, K.; Seo, G., *J. Coll. Interf. Sci.* **2011**, *361*, 612-617.
164. Ling, S.; Slater, B., *Chem. Sci.* **2016**, *7*, 4706-4712.
165. Jasuja, H.; Peterson, G. W.; Decoste, J. B.; Browe, M. A.; Walton, K. S., *Chem. Eng. Sci.* **2014**, *124*, 118-124.
166. Juan-Alcaniz, J.; Ramos-Fernandez, E. V.; Lafont, U.; Gascon, J.; Kapteijn, F., *J. of Cat.* **2010**, *269*, 229-241.
167. Nazari, M.; Rubio-Martinez, M.; Tobias, G.; Barrio Jorge, P.; Babarao, R.; Nazari, F.; Konstas, K.; Muir Benjamin, W.; Collins Stephen, F.; Hill Anita, J.; Duke Mikel, C.; Hill Matthew, R., *Advanced Functional Materials* **2016**, *26* (19), 3244-3249.
168. Wee, L. H.; Bonino, F.; Lamberti, C.; Bordiga, S.; Martens, J. A., *Green Chem.* **2014**, *16*, 1351-1357.
169. Shen, J.; Liu, G.; Huang, K.; Li, Q.; Guan, K.; Li, Y.; Jin, W., *J. of Membr. Sci.* **2016**, *513*, 155-165.
170. Bromberg, L.; Diao, Y.; Wu, H.; Speakman, S. A.; Hatton, T. A., *Chem. Mat.* **2012**, *24*, 1664-1675.
171. Ferey, G.; Mellot-Draznieks, C.; Serre, C.; Millange, F.; Dutour, J.; Surble, S.; Margiolaki, I., *Sci.* **2005**, *309*, 2040-2042.
172. Zhang, Y.; Wan, J.; Wang, Y.; Ma, Y., *RSC Adv.* **2015**, *5*, 97589-97597.

173. Sievers, C.; Noda, Y.; Qi, L.; Albuquerque, E. M.; Rioux, R. M.; Scott, S. L., *ACS Catal.* **2016**, *6* (12), 8286-8307.
174. Couck, S.; Denayer, J. F. M.; Baron, G. V.; Rémy, T.; Gascon, J.; Kapteijn, F., *J. Am. Chem. Soc.* **2009**, *131* (18), 6326-6327.
175. Yang, X.; Liang, Y.; Song, Y.; Wang, X.; Wang, Z.; Qiu, J., *RSC Adv.* **2014**, *9*, 31932-31936.
176. Jimare, M. T.; Cazana, F.; Ramirez, A.; Royo, C.; Romeo, E.; Faria, J.; Resasco, D. E.; Monzon, A., *Cat. Today* **2013**, *210*, 89-97.
177. Kusunoki, Y.; Miyazawa, T.; Kunimori, K.; Tomoshige, K., *Cat. Comm.* **2005**, *6*, 645-649.
178. Feng, J.; Xu, B., *Prog. React. Kinet. and Mech.* **2014**, *39*, 1-15.
179. Liu, H.; Jiang, T.; Han, B.; Liang, S.; Zhou, Y., *Sci.* **2009**, *326*, 1250-1252.
180. Brahmkhatri, V.; Patel, A., *Green Chem. Lett. Rev.* **2012**, *5*, 161-171.
181. Janssens, N.; Wee, L. H.; Bajpe, S.; Breynaert, E.; Kirschhock, C. E. A.; Martens, J. A., *Chem. Sci.* **2012**, *3* ( 6 ), 1847-1850.
182. Bromberg, L.; Klichko, Y.; Chang, E. P.; Speakman, S.; Straut, C. M.; Wilusz, E.; Hatton, T. A., *ACS App. Mat. and Interf.* **2012**, *4*, 4595-4602.
183. Wang, L.; Zhang, B.; Meng, X.; Su, D. S.; Xiao, F., *Chem. Sus. Chem.* **2014**, *7*, 1537-1541.
184. Yang, X.; Liang, Y.; Cheng, Y.; Song, W.; Wang, Z.; Q, J., *Cat. Comm.* **2013**, *47*, 28-31.
185. Jiang, H.; Yu, X.; Peng, X.; Zhang, H.; Nie, R.; Liu, X.; Zhou, D.; Xia, Q., *RSC Adv.* **2016**, *6*, 69045-69051.

186. Yang, Y.; Reber, A. C.; Gilliland, S. E.; Castano, C. E.; Gupton, B. F.; Khanna, S. N., *J. Cat.* **2018**, *360*, 20-26.
187. Vermisoglou, E. C.; Giannakopoulou, T.; Romanos, G.; Boukos, N.; Psycharis, V.; Lei, C.; Lekakou, C.; Petridis, D.; Trapalis, C., *Appl. Surf. Sci.* **2017**, *392*, 244-255.
188. Ma, H.; Zhang, M.; Hu, Q.; Li, W.; Jiang, Z.; Yu, Z.; Dasari, A., *ACS App. Mat. & Interf.* **2011**, *4*, 1948-1953.
189. Wang, W.; Cai, K.; Wu, X.; Shao, X.; Yang, X., *J. Alloy Compd.* **2017**, *722*, 532-543.
190. Lu, Y.; Zhang, F.; Zhang, T.; Leng, K.; Zhang, L.; Yang, X.; Ma, Y.; Huang, Y.; Zhang, M.; Chen, Y., *Carbon* **2013**, *63*, 508-516.
191. Lu, Y.; Huang, Y.; Zhang, F.; Zhang, L.; Yang, X.; Zhang, T.; Leng, K.; Zhang, M.; Chen, Y., *Chinese Science Bulletin* **2014**, *59* (16), 1809-1815.
192. Lu, X.; Li, L.; Song, B.; Moon, K.-s.; Hu, N.; Liao, G.; Shi, T.; Wong, C., *Nano Energ.* **2015**, *17*, 160-170.
193. Dakshinamoorthy, P.; Vaithilingam, S., *RSC Adv.* **2017**, *7* (56), 34922-34932.
194. Lu, X.; Li, Z.; Yin, X.; Wang, S.; Liu, Y.; Wang, Y., *Intl. J. Hydrog. Energ.* **2017**, *42* (27), 17504-17513.
195. Hung, W.; Tsou, C.; Guzman, M. D.; An, Q.; Liu, Y.; Zhang, Y.; Hu, C.; Lee, K.; Lai, J., *Chem. of Mat.* **2014**, *26*, 2983-2990.
196. Shah, R.; Kausar, A.; Muhammad, B.; Khan, M., *Composite Interf.* **2016**, *23*, 887-899.
197. Gilliland, S. E.; Tengco, J. M. M.; Yang, Y.; Regalbuto, J. R.; Castano, C. E.; Gupton, B. F., *Appl. Catal. A: Gen.* **2018**, *550*, 168-175.
198. Hao, X.; Barnes, S.; Regalbuto, J. R., *J. Cat.* **2011**, *279* (1), 48-65.

199. Elkasabi, Y.; Liu, Q.; Choi, Y. S.; Strahan, G.; Boateng, A. A.; Regalbuto, J. R., *Fuel* **2017**, *207*, 510-521.
200. Jiao, L.; Regalbuto, J. R., *J. Cat.* **2008**, *260* (2), 342-350.
201. D'Souza, L.; Regalbuto, J. R., Strong electrostatic adsorption for the preparation of Pt/Co/C and Pd/Co/C bimetallic electrocatalysts. In *Studies in Surface Science and Catalysis*, Gaigneaux, E. M.; Devillers, M.; Hermans, S.; Jacobs, P. A.; Martens, J. A.; Ruiz, P., Eds. Elsevier: 2010; Vol. 175, pp 715-718.
202. D'Souza, L.; Jiao, L.; Regalbuto, J. R.; Miller, J. T.; Kropf, A. J., *J. Cat.* **2007**, *248* (2), 165-174.
203. Zuccaro, L.; Krieg, J.; Desideri, A.; Kern, K.; Balasubramanian, K., *Sci. Rep-UK* **2015**, *5*, 11794.
204. Ai, W.; Zhou, W.; Du, Z.; Du, Y.; Zhang, H.; Jia, X.; Xi, L.; Yi, M.; Yu, T.; Huang, W., *J. Mat. Chem.* **2012**, *22*, 23439-23446.
205. Song, B.; Choi, J. I.; Zhu, Y.; Geng, Z.; Zhang, L.; Lin, Z.; Tuan, C.; Moon, K. S.; Wong, C. P., *Chem. of Mat.* **2016**, *28*, 9110-9121.
206. Cao, Y.; Choi, H. J.; Zhang, W. L.; Wang, B.; Hao, C.; Liu, J., *Compos. Sci. Technol.* **2016**, *122* (Supplement C), 36-41.
207. Li, Z.; Dai, X.; Du, K.; Ma, Y.; Liu, M.; Sun, H.; Ma, X.; Zhang, X., *J. Phys. Chem. C* **2016**, *120* (3), 1478-1487.
208. Rajagopalan, B.; Kim, B.; Hur, S. H.; Yoo, I.-K.; Chung, J. S., *J. Alloy Compd.* **2017**, *709* (J. Alloys Compd. ), 248-259.
209. Johra, F. T.; Lee, J.-W.; Jung, W.-G., *Ind. Eng. Chem. Res.* **2014**, *20* (5), 2883-2887.

210. Labulo, A. H.; Martincigh, B. S.; Omondi, B.; Nyamori, V. O., *J. Mat. Sci.* **2017**, *52* (16), 9225-9248.
211. Rasheed, T.; Rasool, N.; Noreen, M.; Gull, Y.; Zubair, M.; Ullah, A.; Rana, U. A., *J. Sulfur Chem.* **2015**, *36* (3), 240-250.
212. Molander, G. A.; Fumagalli, T., *J. Org. Chem.* **2006**, *71* (15), 5743-5747.
213. Mahanta, A.; Hussain, N.; Das Manash, R.; Thakur Ashim, J.; Bora, U., *Applied Organometallic Chemistry* **2017**, *31* (8), e3679.
214. Reizman, B. J.; Wang, Y.-M.; Buchwald, S. L.; Jensen, K. F., *React. Chem. Eng.* **2016**, *1* (6), 658-666.
215. Guoliang, L.; Bing, P.; Liyuan, C.; Lei, J., *IET Micro & Nano Letters* **2012**, *7* (9), 923-926.
216. Ohde, H.; Hunt, F.; Wai, C. M., *Chemistry of Materials* **2001**, *13* (11), 4130-4135.
217. Wang, Y.; Wu, Y.; Huang, Y.; Zhang, F.; Yang, X.; Ma, Y.; Chen, Y., *J. Phys. Chem. C* **2011**, *115* (46), 23192-23197.
218. Zhang, X.; Ciesielski, A.; Richard, F.; Chen, P.; Prasetyanto, E. A.; Cola, L. D.; Samori, P., **2016**, *Mat. Views* (12), 1044-1052.
219. Hussein, A.; Sarkar, S.; Oh, D.; Lee, K.; Kim, B., *J. Appl. Poly. Sci.* **2016**, *43821*, 1-8.
220. Seuser, G. S.; Banerjee, R.; Metavarayuth, K.; Brandt, A. J.; Maddumapatabandi, T. D.; Karakalos, S.; Lin, Y.; Regalbuto, J. R.; Chen, D. A., *Top. Catal.* **2018**, *61* (5), 379-388.
221. Liu, Y.; Bai, X.; Li, S., *Micropor. Mesopor. Mat.* **2018**, *260*, 40-44.
222. Sharma, A. K.; Gowdahalli, K.; Krzeminski, J.; Amin, S., *J. Org. Chem.* **2007**, *72* (23), 8987-8989.
223. Miao, G.; Ye, P.; Yu, L.; Baldino, C. M., *J. Org. Chem.* **2005**, *70* (6), 2332-2334.

224. Arvela, R. K.; Leadbeater, N. E., *Organic Letters* **2005**, 7 (11), 2101-2104.
225. Taheri, M.; Ghiaci, M.; Shchukarev, A., *Applied Organometallic Chemistry* **2018**, 32 (5), e4338.
226. Xia, J.; Fu, Y.; He, G.; Sun, X.; Wang, X., *Materials Chemistry and Physics* **2018**, 209, 86-94.
227. Tran, T. P. N.; Thakur, A.; Trinh, D. X.; Dao, A. T. N.; Taniike, T., *Appl. Catal. A: Gen.* **2018**, 549, 60-67.
228. Shi, X.; Cai, C., *New J. Chem.* **2018**, 42 (4), 2364-2367.